MULTI-SENSOR FUSION BASED CONTROL FOR AUTONOMOUS OPERATIONS: RENDEZVOUS AND DOCKING OF SPACECRAFT

by

JONATHAN BRYAN MCDONALD

Presented to the Faculty of the Graduate School of
The University of Texas at Arlington in Partial Fulfillment
of the Requirements
for the Degree of

MASTER OF SCIENCE IN AEROSPACE ENGINEERING

THE UNIVERSITY OF TEXAS AT ARLINGTON
December 2006

ACKNOWLEDGEMENTS

I would like to thank my advisor Dr. Subbarao. He has been a tremendous mentor, a true inspiration and an outstanding resource for me. His patience, indefatigable attitude, and demand for excellence is something I will aspire to in all my future engineering endeavors. It has truly been a pleasure to work with someone so enthusiastic about engineering and research.

I must also thank my parents, Bill and Carla, for their continuous support during my education. They have given me much freedom during this process supported me and my decisions along the way. Without their support I would not be where I am today.

Finally I would like to thank Dr. Wilson and Dr. Dogan for taking the time to serve on my committee.

November 27, 2006

ABSTRACT

MULTI-SENSOR FUSION BASED CONTROL FOR
AUTONOMOUS OPERATIONS: RENDEZVOUS
AND DOCKING OF SPACECRAFT

Publication No. _____

Jonathan Bryan McDonald, M.S.
The University of Texas at Arlington, 2006

Supervising Professor: Kamesh Subbarao

The project considers the problem of motion synchronization of free flying robotic spacecraft and serviceable floating objects in space. The synchronization maneuvers are based on sample and hold nonlinear translational and attitude control laws. GPS pseudorange signals and a vision based sensor unit are modeled to give position measurements; position and velocity estimates are extracted from the measurements based on Extended Kalman Filter models. A sensor data fusion algorithm in the form of a Federated Extended Kalman Filter is implemented that blends the estimates of the individual filters into a global estimate. Nonlinear simulations where a Pursuer spacecraft attempted to rendezvous with an uncontrolled free-floating Target spacecraft based on the estimation algorithms were performed. Effects of perturbations including non-uniform gravity and atmospheric drag were imposed to study the robustness of the algorithms.

TABLE OF CONTENTS

Appendix

LIST OF FIGURES

LIST OF TABLES

Nomenclature

x No marker indicates a true value and/or a scalar

$\mathbf{x}$ Bold indicates a vector unless specified otherwise,

all vectors are columns unless otherwise specified

$\hat{\mathbf{x}}$ Hat indicates an estimated value or unit vector (where appropriate)

$\tilde{\mathbf{x}}$ Tilde indicates measurement

$[NB]$ Rotation matrix (from B-frame to N-frame)

$I_{n\times n}$ Appropriately dimensioned identity matrix

$[I]$ 3×3 Inertia matrix

$[\mathbf{a}\times]$ Skew symmetric matrix

τ GPS clock bias

$\boldsymbol{\beta}$ Gyro bias

Superscript

${}^{B}\mathbf{x}$ Upper left indicates the reference frame the vector components are expressed in

N, O, T, P - Inertial, Orbit, Target, and Pursuer Frames respectively will be used

$\mathbf{x}^{T}$ Upper right T indicates the transpose of the vector/matrix

$\hat{\mathbf{x}}^{\mathbf{M}}$ Indicates Fused Master/Global Estimate

$\mathbf{P}^{\mathbf{M}}$ Indicates Fused Master/Global Covariance

ρ GPS pseudorange measurement

Subscript

GPS, vision Sensor description

i Variable number

s/c Stands for Spacecraft (Spacecraft and Satellite will be used interchangeably)

Master/Global Denotes the Master or Global estimate.

Master and Global will be used interchangeably

CHAPTER 1

INTRODUCTION

For the last half-century, space program engineers and scientists have continually addressed the problem of spacecraft rendezvous. One early 1960s Gemini Mission goal was 'to develop effective methods of rendezvous and docking with other orbiting vehicles, and to maneuver the docked vehicles in space.' During Gemini VIII, the first manned spacecraft successfully rendezvoused and docked on March 16, 1966 [1].

Since that time, spacecraft rendezvous and docking has served multiple purposes, including: return from the moon in the Apollo missions; repair and maintenance of the Hubble Space Telescope by astronauts; and refueling/resupply of space stations, including the International Space Station (ISS).

Nearly all past satellite servicing missions have been carried out by astronauts and in a few instances robotic manipulators have aided the mission, but it is both expensive and dangerous for astronauts to capture uncontrolled spinning satellites (even slowly spinning satellites). Thus, it is desirable to develop a free-flying robotic space vehicle capable of carrying out such satellite service missions [2].

One goal of NASA's Space Launch Initiative (SLI) program is to develop such a vehicle, a space transportation system with automated rendezvous and docking generally less expensive and more safe and reliable than today's Space Shuttle [3]. The Space Shuttle currently uses a partially manual system for rendezvous, but a fully autonomous rendezvous system could be more dependable and less dangerous [4].

Several projects dealing with autonomous rendezvous and docking of orbiting satellites have been developed over the past decade, including the Progress spacecraft, Demonstration of Autonomous Rendezvous Technology (DART), and Engineering Test Satellites VII (ETS-VII).

The Progress spacecraft, a Russian expendable unmanned freighter originally developed to supply the Russian space stations, is currently being used to help resupply the ISS. Though proximity operations[1] are monitored and can be overridden by a backup system on the ISS, each Progress' rendezvous and docking operation is capable of being totally autonomous [5]. This procedure, though impressive, is simplified because the ISS (and formally other space stations) is in a controlled orbit, can control its attitude, and manual control can be implemented by the ISS astronauts if problems arise.

While the Progress rendezvous can include ISS manual control, DART and ETS-VII Missions are characterized by two autonomous satellites attempting to rendezvous and dock. Mitsubishi Electric successfully docked two unmanned satellites (ETS-VII) for the first time in 1998 under the funding and direction of Japan's National Space Development Agency (JAXA). Their test established the feasibility of autonomous docking of satellites and provided evidential insight for overcoming various mishaps that could occur [6].

In April 2005, the DART Mission attempted to become the first American autonomous satellite rendezvous; however, approximately 11 hours into what was to be a 24-hour mission, DART detected its propellant supply was depleted and it began a series of maneuvers for departure and retirement. NASA determined most of its

[1] 'Proximity operations' are defined as the navigation and control of two or more vehicles that are operating in the vicinity of each other [4].

mission goals were not achieved [7], and autonomous satellite rendezvous continues to remain a developing technology.

As orbital activity continues to increase, it becomes more and more imperative that an autonomous space vehicle capable of capturing a tumbling object in orbit be developed, so that it might remove space debris, service a malfunctioning satellite, refuel a powerless satellite, and/or install improved technology.

The launch of just one autonomous servicing system maintained in orbit could provide tremendous savings to the satellite industry by servicing multiple malfunctioning satellites, replacing the current system of launches for every single critical malfunction. Use of such a system would also eliminate the danger astronauts face in colliding with satellites as they repair them. However, the development of such a system is very complex and even tasks such as mission phasing can vary greatly in complexity.

In a broad perspective, the satellite rendezvous mission must carry out sequential tasks corresponding to each phase of the mission. Researchers from JAXA have developed such a phased mission plan using a new system concept called Hyper-Orbital Servicing Vehicle (HOSV). This system consists of a bulky 'mother ship' (which has components similar to a conventional satellite, such as solar panels and a large communication antenna) and a deployable operation vehicle that is agile and compact [8].

The HOSV concept has the servicing/rescue vehicle docked at a mother ship (such as the International Space Station) from which it departs and returns after each mission. *Note: From this point on the rescue satellite will be known as the 'Pursuer' and the satellite to be serviced will be known as the 'Target'.* Before a mission is commenced, knowledge of the Target's orbit must be obtained; once obtained, the entire mission can be roughly divided into seven phases, generally outlined as follows:

Phase I. Departure from mother ship

Phase II. Orbit transfer to Target's orbit & long range approach

Phase III. Target identification & motion characterization

Phase IV. Proximity approach including guidance & control for docking

Phase V. Docking & capture

Phase VI. Service & maintenance

Phase VII. Pursuer return to mother ship

The first phase, Phase I, consists of the Pursuer departing from the mother ship. In Phase II (which can be optimized for fuel or time consumption) the Pursuer transfers from its docked orbit to that of the Target and approaches the Target's area until a positive identification can be made (Phase III). Phase IV begins after the Target has been positively identified and its motion has been characterized. In this phase, the Pursuer's sensors and controllers synchronize the Pursuer's motion with that of the Target until the proper docking alignment is achieved. Once accomplished, the Pursuer can capture and dock with the Target (Phase V). In Phase VI, the Pursuer services the Target and, finally, the Pursuer separates from the Target and returns to its mother ship (unless it is a recovery mission, in which case both return) in Phase VII.

The mission procedure described above is just a general overview of one potential mission, each segment having several different aspects and levels of complexity. This thesis research focuses on Phase IV, the Pursuer's proximity operations just prior to docking.

To achieve the motion synchronization aspect of Phase IV, the dynamical characteristics (translational and rotational motion) of the Target and Pursuer must be known. If the Target is in a free-floating orbit, the Pursuer does not have to account for orbital maneuvers by the Target, but the Target's rotational motion or spin must

be accounted for. All satellites have some type of rotational motion, either for stabilization or caused by gravity gradients or other natural perturbations. However, not all satellites rotate at the same rate (because of various factors — geometry, mission design, mechanical failure, disturbances, etc.), affecting the motion synchronization necessary for rendezvous and capture.

Satellite capture can be roughly categorized into four classifications based upon the attitude error and rate of the Target. The classifications and categories II, III, and IV, shown in Figure 1, are called non-cooperative target captures [8]. The

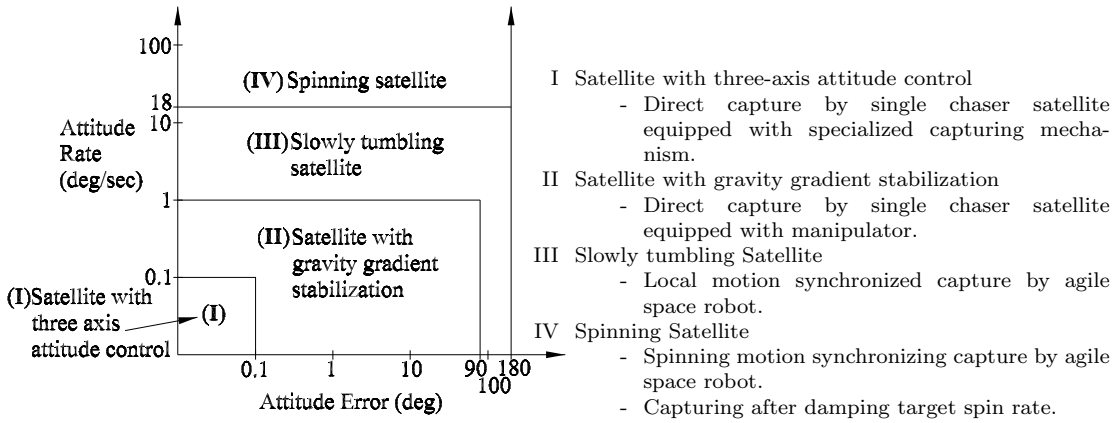

Figure 1.1 Categorization of Satellite Motion.

capture of a spinning satellite (Category IV) is relatively rare, so the remainder of this thesis will focus on estimation and control to achieve motion synchronization for docking with a slowly tumbling satellite (Category III).

Attempting to use grasping equipment without accompanying motion synchronization in a satellite capture is not practically feasible unless the Target is tumbling within the capabilities of the dynamic response of the manipulator, and failure to grasp the Target could result in detrimental collision. Successful capture, then, can

be ensured with a control system combining attitude synchronization and relative position tracking, safely maneuvering the Pursuer so that its docking component is always facing the docking component of the Target. While maintaining this attitude orientation through attitude synchronization, the relative position of the satellites gradually decreases until grasping is established. This method effectively couples the translational and rotational dynamics of the system, discussed at length in Chapter 2.

As previously stated, the dynamical characteristics (position, velocity, attitude, rotation rate, inertia, etc.) of both satellites in question must be known, and the Pursuer must have robust control laws for the relative position and orientation needed in the desired rendezvous and docking trajectory. Since dynamical values can never be known exactly, the Pursuer must employ sensors to take measurements and filters in order to estimate those dynamics based on measured data. Potential sensors for navigational use in low earth orbit (LEO) are the Global Positioning System (GPS), a vision-based navigation system, and an attitude determination system, each having unique advantages and disadvantages in terms of measurement and navigation performance. This thesis studies the fusion of multiple sensors (GPS and vision) to produce a more robust form of navigation which minimizes the impact of each sensor's particular disadvantages.

GPS navigation alone is inadequate because it is subject to outages from blockage [9, 10], atmospheric ionization during re-entry, and delta-v maneuvers, as well as multipath errors and integrity problems. As an example, when a spacecraft approaches the ISS to perform rendezvous and docking, signals from GPS satellites may be degraded as they reflect off the ISS before reaching the GPS receiver, or may be completely blocked by the ISS structure, possibly resulting in fewer measurements and a poorer estimate [10].

A form of navigation that has received much attention in recent years (particularly for satellite guidance) has been the integration of GPS and inertial navigation systems (INS)[2] [10, 11, 12]. This fused sensor system has sparked much interest as a possible navigation solution for all spacecraft flight phases: ascent, on-orbit, proximity operations, re-entry, and landing. Often GPS/INS integration is implemented through a centralized Kalman filter architecture, a form of sensor fusion described in more detail in Chapter 7. Gaylor [10] concluded that a GPS/INS sensor system is feasible for rendezvous with the ISS if an additional sensor were available to aid the INS within 10 to 20 meters of the ISS. Other multi-sensor rendezvous systems should be considered to see if a better solution can be found.

Vision-based sensor systems have also received much attention in recent years. A vision-based system such as the one developed in [13] can be very accurate for relative position determination, but is not a viable navigation option when the Target is not within proximity of the Pursuer. Sun and Crassidis [14] have shown that, for large distances, the vision-based measurements become colinear and state observability is lost.

In most missions it is likely the position, velocity, and attitude sensors of the Target are operational, thereby providing the Pursuer with the state data necessary for a rendezvous. But for instances when the Target is powerless, Lichter and Dubowsky [15] have developed an approach utilizing 3-D vision sensors that provide input to a Kalman filter during an observation phase, and the filter then extracts the full dynamic state and inertial parameters of the Target. This study assumes the Target is in a free-floating orbit and is slowly tumbling, but its communications and sensor systems are operational, enabling it to transmit its dynamical characteristics to

[2]Inertial navigation systems generally consist of a set of three mutually orthogonal accelerometers and three mutually orthogonal gyroscopes used for position and attitude determination respectively.

the Pursuer (i.e. the Pursuer has perfect knowledge of the Target's position, velocity, attitude, and angular velocity at all times).

1.1 Research Contributions

This thesis fuses GPS and vision-based sensor systems, utilizing a synchronization approach which ensures that docking components of the two vehicles are aligned for all time. High-fidelity simulations of this fusion implements the natural nonlinearity of the system as well as force disturbances due to differential gravity and drag. An extended Kalman filter is designed that estimates the position and velocity of the Pursuer utilizing GPS pseudorange measurements. As the Pursuer approaches the Target, a vision-based navigation system is initialized to also provide state estimates for use in the control algorithm. A sensor data fusion algorithm utilizes the estimates from the GPS and vision sensor to create a global/master estimate in the form of an Federated Extended Kalman Filter (FEKF).

1.2 Research Outline

This section provides an outline of the remaining chapters of this thesis:

Chapter 2: details the dynamics and control governing the spacecraft in this study.

Chapter 3: gives a general outline of how the sensor measurements were filtered to provide state estimates.

Chapter 4: briefly describes the Global Positioning System and gives the measurement and estimation model state estimation.

Chapter 5: provides an outline of the selected vision-based navigation system and gives the measurement and estimation model used for relative navigation.

Chapter 6: describes the method used to measure and filter the satellite attitude estimates.

Chapter 7: gives a brief description of different sensor fusion methods then develops algorithm for the FEKF and applies it to the GPS and vision sensors models used in this thesis.

Chapter 8: presents the results and analysis for the GPS/vision fusion simulations.

Chapter 9: summarizes the research, states conclusions, and lists possible future work that can be done.

CHAPTER 2

KINEMATICS, DYNAMICS, & CONTROL

2.1 Reference Frames

To adequately describe the motion of a body, one or more reference frames in which the motion takes place must be established. One such reference frame, a rectangular coordinate system, can be created by defining the system's origin and sense of direction. In this thesis, all such systems will have a right-handed sense in which the positive directions of each axis will form an orthogonal triplet. Three base unit vectors will be used to represent the three orthogonal axes and any other vector in the system will be described by a linear combination or those base unit vectors [16].

An inertial reference frame is one in which Newton's Laws of Motion apply. To qualify as an inertial frame, the origin of the frame must be non-rotating and non-accelerating. In practice, a truly inertial reference frame cannot be defined in the vicinity of the solar system due to the gravitational fields of the sun, planets, and other bodies orbiting the sun. However, it is possible to define reference systems that are 'inertial enough' so that the deviation of the actual motion of an object from the motion predicted by Newton's Laws is insignificant over the time span of interest [10].

The simulations described in this thesis will utilize both inertial and non-inertial reference frames. The frames used will be described in the next sections and include: Earth Centered Inertial (ECI), Hill's Relative Orbit Frame (O-frame), Target Frame (T-frame), and Pursuer Frame (P-frame). The ECI frame is inertial while the O, T, and P-frames are considered non-inertial because of satellite motion.

2.1.1 Earth Centered Inertial (ECI) Reference Frame (N-frame)

The ECI frame's origin is located at the center of mass of the Earth and its fundamental plane is the Earth's equator. The frame's X-axis points towards the Vernal Equinox, the Y-axis lays 90 degrees to the east in the equatorial plane of the equator, and the Z-axis points towards the North Pole. Since the equinox and plane of the equator move very slowly over time, the ECI frame can only be considered 'pseudo' inertial if the equator and equinox are referred to at a particular epoch [16]. The J2000 system represents the best realization of an ideal, inertial frame at the J2000 epoch. The motion of the equator and the equinox can be accounted for, so inertial frames at other times defined by the equator and equinox of date can be transformed to the J2000 ECI frame. These other inertial frames are called true-of-date because they reference the true equator and true equinox at a particular date. The ECI frame's unit vectors will be denoted by $\{\hat{n}_1, \hat{n}_2, \hat{n}_3\}$.

2.1.2 Hill's Relative Orbit Frame (O-frame)

The origin of the O-frame is located at the center of mass of the Target satellite and its orientation is given by the vector triad $\{\hat{o}_r, \hat{o}_\theta, \hat{o}_h\}$ shown in Figure 2.1. The vector $\hat{o}_r$ is in the orbit radius direction, while $\hat{o}_h$ is parallel to the orbit momentum vector in the orbit normal direction. The vector $\hat{o}_\theta$ then completes the right-handed coordinate system. Mathematically, these O-frame orientation vectors are expressed as

$$\hat{o}_r = \frac{\mathbf{R}_T}{R_T}$$
$$\hat{o}_h = \frac{\mathbf{h}_T}{h_T}$$
$$\hat{o}_\theta = \hat{o}_h \times \hat{o}_r$$

where $\mathbf{R}_T$ is the radius vector of the Target satellite from the center of the earth, $\mathbf{h}_T = \mathbf{R}_T \times \dot{\mathbf{R}}_T$ is the angular momentum vector of the Target's orbit, and R_T and h_T

are the magnitudes of the $\mathbf{R}_T$ and $\mathbf{h}_T$ vectors respectively. *Note: bold will represent a vector and the corresponding non-bold character will represent the magnitude of that vector for the remainder of the thesis.* (Note: if the inertial target orbit is circular then $\hat{o}_\theta$ is parallel to the satellite velocity vector) This rotating reference frame is sometimes also referred to as the local-vertical-local-horizontal (LVLH) frame [17].

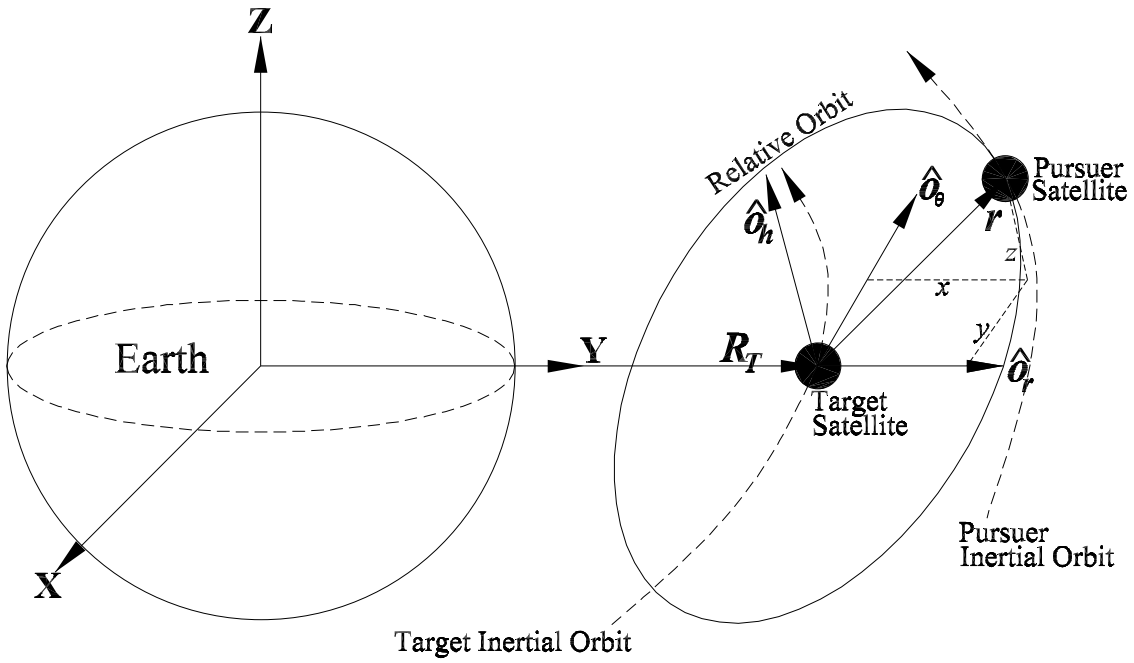

Figure 2.1 General Relative Orbit Illustration.

2.1.3 Body-Fixed Reference Frames

Two body-fixed reference frames are used in this study: the Target Reference Frame ($T-$ frame) and the Pursuer Reference Frame ($P-$ frame). The Target Frame, denoted by $\left\{\hat{t}_1, \hat{t}_2, \hat{t}_3\right\}$ is the body-fixed reference frame of the Target satellite with the origin located at the Target's center of mass. The frame's origin is coincident

with the Hill's frame origin and is fixed to the Hill's frame origin as it travels through inertial space. However, the Target Frame is able to rotate freely in inertial space and therefore does not necessarily have the same orientation as the Hill's frame.

The Pursuer Frame is the body-fixed reference frame of the Pursuer satellite with the origin located at the Pursuer's center of mass and is denoted by $\{\hat{p}_1, \hat{p}_2, \hat{p}_3\}$.

These frames provide a foundation in which the governing dynamics and kinematics can be consistently described. In the following section the kinematics and dynamics governing the rigid body spacecraft in this study are discussed.

2.2 Rigid Body Kinematics & Dynamics

Dynamics is a body's resulting motion due to applied forces and torques and can generally be divided up into translational motion (how a body moves in space) and rotational motion (how a body rotates and reacts to applied torques). In the following sections, the translational and rotational dynamics applicable to satellite motion in this study will be discussed.

2.2.1 Translational Dynamics

This section discusses the dynamics governing translational motion assumed to be acting on the rigid body satellites in this study. Since this study focuses on spacecraft, the dynamics described will focus on orbital mechanics.

The GPS constellation and the Target and Pursuer spacecraft are all assumed to follow general two-body motion. The Target and Pursuer are considered to be under the additional influence of J_2 and drag perturbations. The GPS satellites are not subject to perturbations because it is assumed that they are in controlled orbits to maintain the constellation formation. Additional acceleration to the Pursuer

spacecraft can be applied in the form of a control force. The general spacecraft translational acceleration can then be described in vector form as

$$\ddot{\mathbf{R}}_{s/c} = \mathbf{a}_{s/c} = \mathbf{a}_{2-Body} + \mathbf{a}_{J_2} + \mathbf{a}_{Drag} + \mathbf{u}_{Trans} \tag{2.1}$$

2.2.1.1 2-Body Motion

The most general orbital dynamics motion is two-body motion and can be given by

$$\mathbf{a}_{2-Body} = -\frac{\mu \mathbf{R}}{R^3} \tag{2.2}$$

This motion assumes that both bodies in question can be treated as point masses and that the mass of one body is several orders of magnitude larger than that of the other body. The term μ is known as the gravitational parameter; for 2-body motion in the vicinity of the earth, μ is given by $\mu = GM_E$ where G is the universal gravitational constant, M_E is the mass of the earth, and R is the radius vector of the satellite.

The accelerations $\mathbf{a}_{J_2}$ and $\mathbf{a}_{Drag}$ in (2.1) are due to perturbation forces caused by differential gravity and atmospheric drag.

2.2.1.2 Perturbation Effects on Translational Motion

Perturbations are deviations from a normal, idealized, or undisturbed motion. A spacecraft in orbit is likely to face several different perturbing forces such as atmospheric drag, solar-radiation pressure, magnetic field disturbances, third body effects (sun, moon, planets, etc.), and asphericity of the central body [16]. In this study, the effects of a second order oblate earth model and of atmospheric drag are considered.

Differential Gravity (J_2): As can be seen in the two-body equation, gravitational forces are based on the magnitude of separation and the masses of the bodies

in question. However, as previously stated, two-body motion assumes the bodies can be approximated as point masses. This assumption is accurate for short periods of time, but in reality the earth is not a perfect sphere, and its mass density is not evenly distributed – so the gravitational force acting upon a satellite in orbit about the earth varies depending on the satellite's orbital position. The inertial acceleration due to a second order oblate earth model is given by

$$\mathbf{a}_{J_2} = \begin{bmatrix} -\frac{3J_2\mu R_E^2 X}{2R^5}\left(1-\frac{5Z^2}{R^2}\right) \\ -\frac{3J_2\mu R_E^2 Y}{2R^5}\left(1-\frac{5Z^2}{R^2}\right) \\ -\frac{3J_2\mu R_E^2 Z}{2R^5}\left(3-\frac{5Z^2}{R^2}\right) \end{bmatrix} \tag{2.3}$$

where J_2 is a constant, R_E, it the average equatorial radius of the earth, and $\{X, Y, Z\}$ are the three components of the inertial radius vector $\mathbf{R}$.

Atmospheric Drag: Atmospheric drag is a significant force on vehicles in motion on the earth, but its effects reduce significantly as the vehicle's altitude above the surface of the earth increases. However, for satellites in low earth orbits (LEO), atmospheric drag is a significant problem and can severely shorten a satellite's orbit lifespan if orbit maintenance is not performed. In general, the acceleration on a rigid body due to atmospheric drag is given by

$$\mathbf{a}_{Drag} = -\frac{1}{2}\rho\frac{c_D A}{m}v_{rel}^2\frac{\mathbf{v}_{rel}}{\|\mathbf{v}_{rel}\|} \tag{2.4}$$

where ρ is the density of the atmosphere, c_D is the spacecraft's coefficient of drag, A is the exposed area, m is the mass of the spacecraft, and $\mathbf{v}_{rel}$ is the velocity of the spacecraft relative to the earth's rotating atmosphere given by $\mathbf{v}_{rel} = \dot{\mathbf{R}} - \boldsymbol{\omega}_E \times \mathbf{R}$

where $\boldsymbol{\omega}_E = \begin{bmatrix} 0 & 0 & \omega_E \end{bmatrix}^T$ is the angular velocity of the earth. The term $\frac{c_D A}{m}$ in (2.4) is sometimes called the 'ballistic coefficient' and is denoted by

$$B = \frac{c_D A}{m} \tag{2.5}$$

The density of the earth's upper atmosphere cannot be known exactly because of factors such as seasonal variations and solar radiation. However, many models have been developed to approximate the atmosphere's density at high altitudes. One such approximation method, known as the exponential atmosphere model, was chosen to approximate the atmospheric density in this study. In the exponential atmosphere model, the density varies exponentially according to

$$\rho = \rho_\circ \exp\left[-\frac{h_{ellp} - h_\circ}{H}\right]$$

where $\rho_\circ$ is the reference density, h_o is the reference altitude, h_{ellp} is the actual altitude above the ellipsoid, and H is the scale height. Each of these values are based upon the spacecraft's altitude and are given in appendix A.

Combining equations (2.2), (2.3), and (2.4) into (2.1) gives the uncontrolled spacecraft acceleration governing the Target and Pursuer in inertial space as

$$\begin{aligned}
\ddot{X} &= -\frac{\mu X}{R^3} - \frac{3\mu J_2 R_E^2 X}{2R^5}\left(1 - \frac{5Z^2}{R^2}\right) \\
&\quad - \frac{1}{2}\frac{\rho c_D A}{m}\left(\dot{X} + \omega_E Y\right)\sqrt{\left(\dot{X} + \omega_E Y\right)^2 + \left(\dot{Y} - \omega_E X\right)^2 + \dot{Z}^2} \\
\ddot{Y} &= -\frac{\mu Y}{R^3} - \frac{3\mu J_2 R_E^2 Y}{2R^5}\left(1 - \frac{5Z^2}{R^2}\right) \\
&\quad - \frac{1}{2}\frac{\rho c_D A}{m}\left(\dot{Y} - \omega_E X\right)\sqrt{\left(\dot{X} + \omega_E Y\right)^2 + \left(\dot{Y} - \omega_E X\right)^2 + \dot{Z}^2} \\
\ddot{Z} &= -\frac{\mu Z}{R^3} - \frac{3\mu J_2 R_E^2 Z}{2R^5}\left(3 - \frac{5Z^2}{R^2}\right) \\
&\quad - \frac{1}{2}\frac{\rho c_D A}{m}\left(\dot{Z}\right)\sqrt{\left(\dot{X} + \omega_E Y\right)^2 + \left(\dot{Y} - \omega_E X\right)^2 + \dot{Z}^2}
\end{aligned} \tag{2.6}$$

The inertial translational motion of the spacecraft has been established, but for a rendezvous engagement involving two spacecraft the motion of one spacecraft with respect to another must also be known. Therefore, the dynamics governing the relative motion between spacecraft in orbit must also be established.

2.2.1.3 Spacecraft Relative Motion Dynamics

The previous section described the motion of a single spacecraft in inertial space, but to study a rendezvous scenario, the relative motion between all spacecraft involved must be known. This section develops the relative orbit equations of motion that govern Target and Pursuer satellites in this study.

The relative orbit position vector, $\mathbf{r}$, is shown in Figure 2.1 above and can be expressed in the rotating Hill frame or O-frame components as $r = [x\ y\ z]^T$. Use of this frame is advantageous because the $\{x, y\}$ coordinates define motion in the Target's orbit plane, and the z coordinate describes out-of-plane motion.

The position vector of the Target in Hill frame components is

$$\mathbf{R}_T = R_T \hat{o}_r \tag{2.7}$$

and the position of the Pursuer can be written in vector form as

$$\mathbf{R}_P = \mathbf{R}_T + \mathbf{r} = (R_T + x)\,\hat{o}_r + y\hat{o}_\theta + z\hat{o}_h \tag{2.8}$$

Taking the derivative of equation (2.8) with respect to the inertial frame and using the transport theorem gives

$$\dot{\mathbf{R}}_P = \dot{\mathbf{R}}_T + \frac{^O d}{dt}\mathbf{r} + \boldsymbol{\omega}_{O/N} \times \mathbf{r} \tag{2.9}$$

where $\boldsymbol{\omega}_{O/N}$ is the angular velocity of the rotating Hill frame given by

$$\boldsymbol{\omega}_{O/N} = \frac{\left\| \mathbf{R}_T \times \dot{\mathbf{R}}_T \right\|}{\left\| \mathbf{R}_T \right\|^2} \hat{o}_h = \dot{\theta}\hat{o}_h \tag{2.10}$$

Differentiating equation (2.9) and using the transport theorem again gives the Pursuer's acceleration vector as

$$\ddot{\mathbf{R}}_P = \ddot{\mathbf{R}}_T + \frac{^O d^2}{dt^2}\mathbf{r} + 2\boldsymbol{\omega}_{O/N} \times \frac{^O d}{dt}\mathbf{r} + \dot{\boldsymbol{\omega}}_{O/N} \times \mathbf{r} + \boldsymbol{\omega}_{O/N} \times \left(\boldsymbol{\omega}_{O/N} \times \mathbf{r}\right) \tag{2.11}$$

where

$$\dot{\boldsymbol{\omega}}_{O/N} = \ddot{\theta}\hat{o}_h = -2\frac{\dot{R}_T}{R_T}\dot{\theta}\hat{o}_h \tag{2.12}$$

The acceleration of the Target can be found by twice differentiating (2.7) with respect to the inertial frame and is given by

$$\ddot{\mathbf{R}}_T = \left(\ddot{R}_T - R_T\dot{\theta}^2\right)\hat{o}_r = -\frac{\mu}{R_T^2}\hat{o}_r \tag{2.13}$$

Equating vector components in equation (2.13), the Target orbit radius acceleration is expressed as

$$\ddot{R}_T = R_T\dot{\theta}^2 - \frac{\mu}{R_T^2} \tag{2.14}$$

Then substituting equations (2.12) and (2.14) into (2.11), the Pursuer acceleration vector is reduced to

$$\ddot{\mathbf{R}}_P = \left(\ddot{x} - 2\dot{\theta}\left(\dot{y} - y\frac{\dot{R}_T}{R_T}\right) - x\dot{\theta}^2 - \frac{\mu}{R_T^2}\right)\hat{o}_r + \left(\ddot{y} + 2\dot{\theta}\left(\dot{x} - x\frac{\dot{R}_T}{R_T}\right) - y\dot{\theta}^2\right)\hat{o}_\theta + \ddot{z}\hat{o}_h \tag{2.15}$$

Substituting the kinematic acceleration expression from equation (2.15) into the orbit equations of motion, the Pursuer's orbital equations of motion are given by

$$\ddot{\mathbf{R}}_P = -\frac{\mu}{R_P^3}{}^{O}\begin{pmatrix} R_T + x \\ y \\ z \end{pmatrix} \tag{2.16}$$

with $R_P = \sqrt{(R_T + x)^2 + y^2 + z^2}$. Equating equations (2.15) and (2.16) yields the exact nonlinear Hills relative equations of motion.

$$\begin{aligned}
\ddot{x} &= 2\dot{\theta}\dot{y} + \ddot{\theta}y + \dot{\theta}^2 x - \frac{\mu(R_T+x)}{\left((R_T+x)^2+y^2+z^2\right)^{3/2}} + \frac{\mu}{R_T^2} \\
\ddot{y} &= -2\dot{\theta}\dot{x} - \ddot{\theta}x + \dot{\theta}^2 y - \frac{\mu y}{\left((R_T+x)^2+y^2+z^2\right)^{3/2}} \\
\ddot{z} &= -\frac{\mu z}{\left((R_T+x)^2+y^2+z^2\right)^{3/2}} \\
\ddot{R}_T &= R_T\dot{\theta}^2 - \frac{\mu}{R_T^2} \\
\ddot{\theta} &= \frac{-2\dot{R}_T\dot{\theta}}{R_T}
\end{aligned} \tag{2.17}$$

The only assumption that has been made is that no disturbances are acting on the satellites, and thus Keplerian motion assumption in the orbital equations of motion is correct. The relative equations of motion are valid for arbitrarily large relative orbits, and the Target orbit may be eccentric [17].

2.2.2 Rigid Body Kinematics

Many applications require knowledge of a rigid body's attitude, also known as orientation. The ability to determine a rigid body's orientation and control that orientation is vital to many modern operations in a variety of fields, including: a solar panel following the sun as it crosses the horizon; a surveillance satellite monitoring a specific location for an extended period of time; and a passenger airplane. In the case of spacecraft rendezvous, the attitude of all spacecraft in question must be known accurately in order for a rendezvous to occur. Onboard computers must know the orientation before firing thrusters to decrease the relative separation of the spacecraft. The attitude must also be known for the spacecraft to align their respective docking ports for rendezvous and possibly for communications.

Numerous forms of attitude representation have been developed, each with advantages and disadvantages. Euler angles are a simple minimal and intuitive means of attitude determination but prone to singularities in the attitude kinematics. In fact, all minimal parameter attitude sets have singularities. One parameter set, based on Euler's Principal Rotation Theorem[1], is known at Euler Parameters or quaternions and eliminates singularities, but they are an over parameterized set and therefore require an additional constraint. Another attitude representation based on Euler's Theorem is known as Modified Rodrigues Parameters (MRP) [17]. MRPs were selected for use in this study and are are described below.

2.2.2.1 Modified Rodrigues Parameters

The Modified Rodrigues Parameters (MRPs) are an efficient and robust form of attitude parameters based on Euler's Principal Rotation Theorem. The MRP vector can be expressed in terms of the principal rotation elements as $\boldsymbol{\sigma} = \hat{\mathbf{e}} \tan\left(\frac{\phi}{4}\right)$ where $\hat{\mathbf{e}}$ is the vector about which the rotation takes place and ϕ is the angle of rotation. MRPs are a minimal parameter representation and, as with all minimal parameter representations, have a singularity. However, MRPs are more robust than other minimal parameter forms because they are accurate and effective for small and large angles of rotation and only encounter singularities when $\phi = \pm 360^\circ$ (or one full rotation). One effective method to avoid this singularity is to break up the rotation into smaller successive rotations.

[1] **Theorem 2.2.1 (Euler's Principal Rotation Theorem)** *A rigid body or coordinate reference frame can be brought from an arbitrary initial orientation to an arbitrary final orientation by a single rigid rotation through a principal angle ϕ about the principal axis $\hat{\mathbf{e}}$; the principal axis is a judicious axis fixed in both the initial and final orientation [17].*

The MRP representation can provide a transformation from the inertial frame, N, to a general body frame, B, through a direction cosine matrix or rotation matrix given by the relation

$$[BN] = [I_{3\times3}] + \frac{8\left[\boldsymbol{\sigma}\times\right]^2 - 4\left(1-\sigma^2\right)\left[\boldsymbol{\sigma}\times\right]}{\left(1+\sigma^2\right)^2} \tag{2.18}$$

where $[BN]$ is the rotation matrix from the body frame to the inertial frame, $I_{3\times3}$ is a 3×3 identity matrix and $[\boldsymbol{\sigma}\times]$ is a cross product matrix that follows the form $\mathbf{a} \times \mathbf{b} = [\mathbf{a}\times]\,\mathbf{b}$, with

$$[\mathbf{a}\times] = \begin{bmatrix} 0 & -a_3 & a_2 \\ a_3 & 0 & -a_1 \\ -a_2 & a_1 & 0 \end{bmatrix}$$

The kinematic differential equation of the MRPs in vector form is given by

$$\dot{\boldsymbol{\sigma}} = \frac{1}{4}\left[\left(1-\sigma^2\right)[I_{3\times3}] + 2\left[\boldsymbol{\sigma}\times\right] + 2\boldsymbol{\sigma}\boldsymbol{\sigma}^T\right]\boldsymbol{\omega} = \frac{1}{4}\left[B\left(\boldsymbol{\sigma}\right)\right]\boldsymbol{\omega} \tag{2.19}$$

and gives the time rate of change of the MRP [17].

2.2.3 Rotational Dynamics

The previous section discussed how the satellite's orientation can be described mathematically in multiple reference frames and how that orientation can change over time with respect to an inertial frame. However, to give a complete description of a rigid body's rotational motion, its rotational dynamics must be discussed. The attitude kinematics described above do not give a complete picture of the rotational motion governing the rigid bodies in this study because they do not account for the

rigid body's inertia or applied torques (controlled and uncontrolled). The following section describes the rotational dynamics used.

The torque applied to a rigid body equals the inertial rate of change of the angular momentum

$$\mathbf{T} = \frac{^N d}{dt}\mathbf{h} \tag{2.20}$$

where $\mathbf{T}$ is the applied torque and $\mathbf{h}$ is the angular momentum of the rigid body. The angular momentum of a rigid body is given by the expression

$$\mathbf{h} = [I]\,\boldsymbol{\omega}_{B/N} \tag{2.21}$$

where $[I]$ is the rigid body's moment of inertia matrix and $\boldsymbol{\omega}_{B/N}$ is the rigid body's rotation rate with respect to the inertial frame. This form for the angular momentum is convenient because the inertia matrix is constant in body frame components (because of rigid-body assumption). However, a relationship must be found to relate the inertial derivative of the angular momentum to the body frame components. The time derivative of a vector with respect to the inertial frame is related to the time derivative with respect to the body frame by

$$\frac{^N d}{dt}\mathbf{r} = \frac{^B d}{dt}\mathbf{r} + \boldsymbol{\omega}_{B/N} \times \mathbf{r} \tag{2.22}$$

This relationship is sometimes referred to as the transport theorem. Applying the transport theorem to (2.20) the torque then becomes

$$\mathbf{T} = \frac{^B d}{dt}\,[I]\,\boldsymbol{\omega}_{B/N} + \boldsymbol{\omega}_{B/N} \times [I]\,\boldsymbol{\omega}_{B/N} \tag{2.23}$$

Remembering that in the body frame the inertia is constant (2.23) can be reduced to

$$\mathbf{T} = [I]\,\dot{\boldsymbol{\omega}}_{B/N} + \boldsymbol{\omega}_{B/N} \times [I]\,\boldsymbol{\omega}_{B/N} \tag{2.24}$$

which is known as Euler's equation [18].

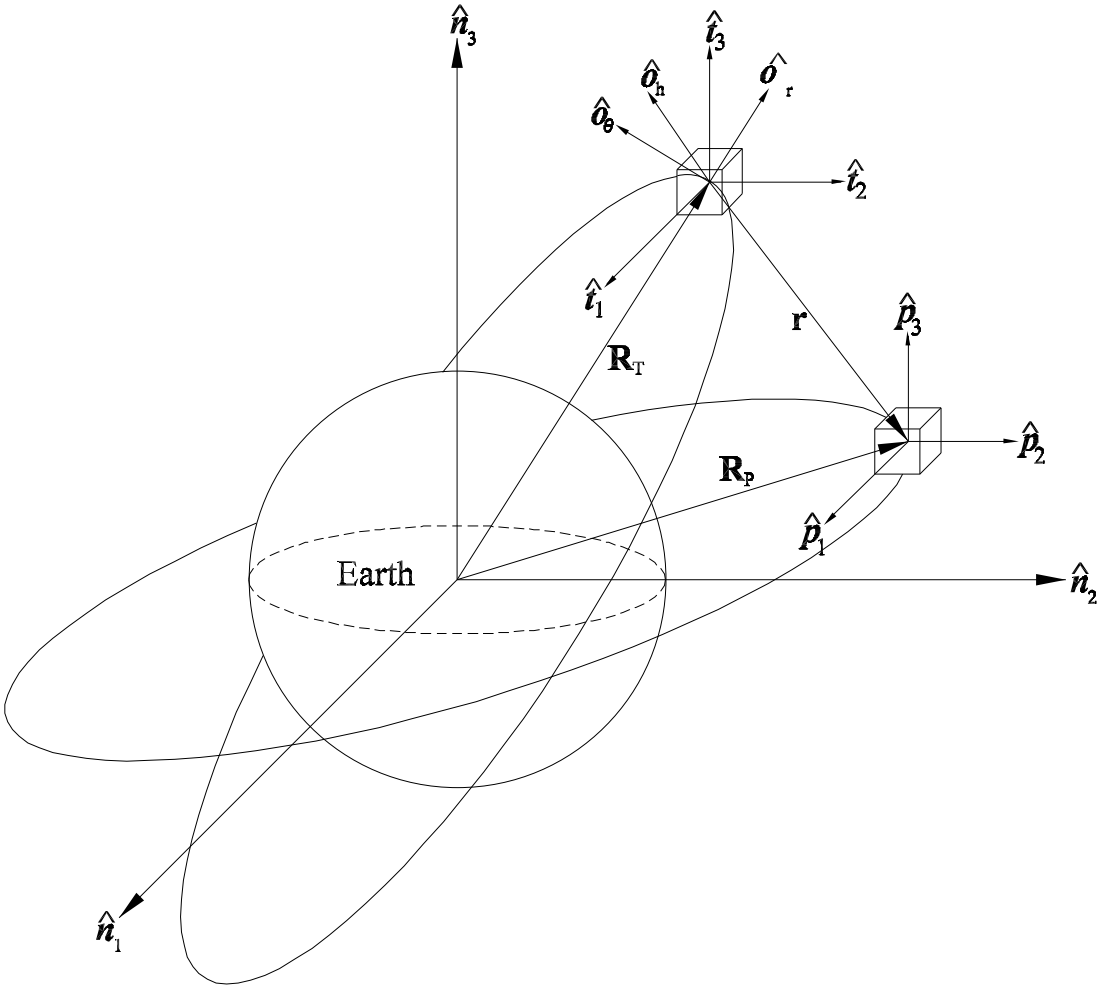

Figure 2.2 General Rendezvous Mission Orbit Setup.

The previous sections described the uncontrolled kinematics and dynamics of the spacecraft being studied but did not cover the stability or controllability of the dynamics. For two spacecraft to engage in a rendezvous, the dynamics of at least one of the vehicles must be controlled.

2.3 Control

As stated previously, it is assumed that the Target is in an uncontrolled orbit and is arbitrarily tumbling such that it cannot modify its orbit or control its attitude. The Pursuer spacecraft is controllable and able to modify its orbit and attitude through the use of translational and rotational control forces denoted by $\mathbf{u_{Trans}}$ and $\mathbf{u_{Rot}}$. These control forces are assumed to be arbitrary, such that no distinction is made whether the control force is provided by thrusters, momentum wheels, solar sails, etc.

The main focus of this study is estimation and sensor fusion; therefore, Proportional-Derivative (PD) controllers have been chosen because they are simple and robust. A PD controller follows the form

$$\mathbf{u} = -k_P\mathbf{e} - k_D\dot{\mathbf{e}} \tag{2.25}$$

where $\mathbf{u}$ is the control, k_P is the proportional gain, k_D is the derivative gain, and $\mathbf{e}$ and $\dot{\mathbf{e}}$ are the error vectors given by

$$\mathbf{e} = \mathbf{r} - \mathbf{r}_{des} \tag{2.26a}$$

$$\dot{\mathbf{e}} = \dot{\mathbf{r}} - \dot{\mathbf{r}}_{des} \tag{2.26b}$$

where $\mathbf{r}$, $\dot{\mathbf{r}}$ is the actual vector and its time derivative and $\mathbf{r_{des}}$, $\dot{\mathbf{r}}_{\mathbf{des}}$ is the desired vector and its time derivative. Proportional gain primarily influences the rise time and overshoot of the controlled response, while the derivative gain will alter response's settling time and overshoot.

Now that the control type has been established the components that will form the translational and rotational controllers can be given.

Translational Controller: Translational control allows the Pursuer to alter its orbit so that it can position itself in the proper relative location (i.e. along the radius vector of the Target's docking port). Following the form given in (2.25) the translational control can be computed by

$$\mathbf{u}_{Trans} = -k_{P_{Trans}} (\mathbf{r} - \mathbf{r}_{des}) - k_{D_{Trans}} (\dot{\mathbf{r}} - \dot{\mathbf{r}}_{des}) \tag{2.27}$$

where $\mathbf{u}_{Trans}$ is the translational control, $k_{P_{Trans}}$ and $k_{D_{Trans}}$ are the gains, $\mathbf{r}$ is the separation between the satellites shown in 2.2 and $\mathbf{r}_{des}$ is the desired position for the Pursuer to reach relative to the Target.

Attitude Controller: Attitude control allows the Pursuer to alter its orientation such that its docking port faces the Target's docking (i.e. the respective docking ports are aligned). The PD form for the attitude controller is given by

$$\mathbf{u}_{Rot} = -k_{P_{Rot}} (\boldsymbol{\sigma} - \boldsymbol{\sigma}_{des}) - k_{D_{Rot}} (\dot{\boldsymbol{\sigma}} - \dot{\boldsymbol{\sigma}}_{des}) \tag{2.28}$$

where $\boldsymbol{\sigma}$ is the MRP orientation of the Pursuer, $\dot{\boldsymbol{\sigma}}$ is given in (2.19), and $\boldsymbol{\sigma}_{des}$ and $\dot{\boldsymbol{\sigma}}_{des}$ are the desired MRP orientation and its time derivative. The desired effects of the two controllers is shown in Figure 2.3.

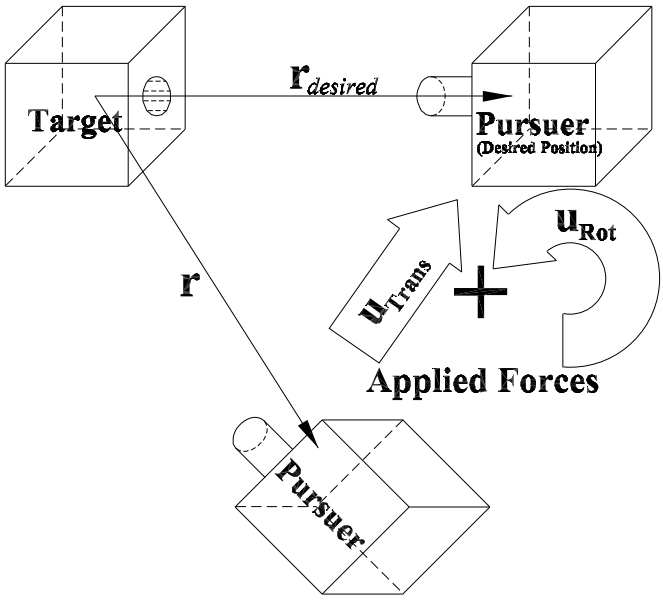

Figure 2.3 Desired Control Effect.

Combining the translational control with the dynamics given in (2.29) gives the equations that govern the translational acceleration of the Pursuer in inertial space

$$
\begin{aligned}
\ddot{X} &= -\frac{\mu X}{R^3} - \frac{3\mu J_2 R_E^2 X}{2R^5}\left(1 - \frac{5Z^2}{R^2}\right) \\
&\quad - \frac{1}{2}\frac{\rho c_D A}{m}\left(\dot{X} + \omega_E Y\right)\sqrt{\left(\dot{X} + \omega_E Y\right)^2 + \left(\dot{Y} - \omega_E X\right)^2 + \dot{Z}^2} + {}^N u_{Trans1} \\
\ddot{Y} &= -\frac{\mu Y}{R^3} - \frac{3\mu J_2 R_E^2 Y}{2R^5}\left(1 - \frac{5Z^2}{R^2}\right) \\
&\quad - \frac{1}{2}\frac{\rho c_D A}{m}\left(\dot{Y} - \omega_E X\right)\sqrt{\left(\dot{X} + \omega_E Y\right)^2 + \left(\dot{Y} - \omega_E X\right)^2 + \dot{Z}^2} + {}^N u_{Trans2} \\
\ddot{Z} &= -\frac{\mu Z}{R^3} - \frac{3\mu J_2 R_E^2 Z}{2R^5}\left(3 - \frac{5Z^2}{R^2}\right) \\
&\quad - \frac{1}{2}\frac{\rho c_D A}{m}\left(\dot{Z}\right)\sqrt{\left(\dot{X} + \omega_E Y\right)^2 + \left(\dot{Y} - \omega_E X\right)^2 + \dot{Z}^2} + {}^N u_{Trans3}
\end{aligned}
\tag{2.29}
$$

Control can also be applied to the relative dynamics given in (2.17) by rotating the inertial translational control into the O-frame such that ${}^{O}\mathbf{u}_{Trans} = [ON]\,{}^{N}\mathbf{u}_{Trans}$ yielding

$$\begin{aligned}
\ddot{x} &= 2\dot{\theta}\dot{y} + \ddot{\theta}y + \dot{\theta}^2 x - \frac{\mu(R_T+x)}{\left((R_T+x)^2+y^2+z^2\right)^{3/2}} + \frac{\mu}{R_T^2} + {}^{O}u_{Trans1} \\
\ddot{y} &= -2\dot{\theta}\dot{x} - \ddot{\theta}x + \dot{\theta}^2 y - \frac{\mu y}{\left((R_T+x)^2+y^2+z^2\right)^{3/2}} + {}^{O}u_{Trans2} \\
\ddot{z} &= -\frac{\mu z}{\left((R_T+x)^2+y^2+z^2\right)^{3/2}} + {}^{O}u_{Trans3} \\
\ddot{R}_T &= R_T\dot{\theta}^2 - \frac{\mu}{R_T^2} \\
\ddot{\theta} &= \frac{-2\dot{R}_T\dot{\theta}}{R_T}
\end{aligned} \tag{2.30}$$

The Pursuer's controlled rotational motion can be found by combining the rotational control in (2.28) with (2.24)

$$\dot{\boldsymbol{\omega}}_{B/N} = -[I]^{-1}\left(\boldsymbol{\omega}_{B/N} \times [I]\,\boldsymbol{\omega}_{B/N}\right) + [I]^{-1}\,\mathbf{u}_{Rot} \tag{2.31}$$

This chapter has given the equations governing the six degree-of-freedom motion of the Target and Pursuer satellites, however, to gain knowledge of the system's motion (i.e. position, velocity, attitude, etc.) the system's parameters must be identified.

The only way to identify a parameter, such as relative position, is to take measurements which, in turn, requires some type of sensor. Since all real-world sensor measurements are inherently noisy to some degree, the quantities measured are altered from the true values by an unknown amount of error. If numerous measurements are taken, an estimation process (or filtering) can be applied to filter out some of the measurement noise and provide estimates of the true values.

In this study, filtering algorithms were utilized to provide position, velocity, and attitude estimates based on measurements from a GPS sensor, a vision based sensor,

and an attitude sensor. The calculated estimates were used in the translational and attitude controllers to initiate and complete the rendezvous engagement scenario. The following chapters will provide a brief description of each of the sensors used and give the mathematical models used to simulate sensor measurements and provide estimates based on those measurements.

CHAPTER 3

ESTIMATION OF DYNAMICAL SYSTEMS

In this study the controllers described previously are dependent on estimated parameters provided by filters. To understand how the filters estimated the state parameters requires a discussion on filtering/estimation. This chapter will define filtering at it applies to this thesis and provide a brief description of various estimation techniques. Then the Extended Kalman Filter, the filter of choice for this thesis, will be discussed, including how it is mathematically modeled and why it was chosen.

3.1 Introduction to Estimation

In general filtering is determining the current state using current (and past) observations. In the estimation of any variable or parameter there are three quantities of interest: the true value, the measured value, and the estimated value. In practice the true value (or 'truth') is rarely known and is the value sought of the quantity being approximated by the estimator. The measured value denotes the quantity which is determined from a sensor (whether by direct or indirect means). Measurements are never perfect, since they will always contain errors (i.e. electronic noise, computational error, unknown bias, etc.) and are usually modeled using a function of the true values plus some error. The measured values of the truth, x, are typically denoted by $\tilde{x}$ [19].

Estimated values of x are determined from the estimation process itself, and are found using a combination of static/dynamic modeling and measurements and are denoted by $\hat{x}$. Other quantities used commonly in estimation are the measurement

error (measurement value minus true value), and the residual error (measurement value minus estimated value). Thus, for a measurable quantity x, the following two equations hold [19]:

$$\begin{array}{ccccc} \text{measured value} & = & \text{true value} & + & \text{measurement error} \\ \tilde{x} & = & x & + & \upsilon \end{array}$$

and

$$\begin{array}{ccccc} \text{measured value} & = & \text{estimated value} & + & \text{residual error} \\ \tilde{x} & = & \hat{x} & + & e \end{array}$$

Similar to the true value, the actual measurement error (υ) is never known in practice. However, the errors in the mechanism that physically generate this error are usually approximated by some known process (often by a zero-mean Gaussian noise process with known variance).

Two of the most common forms of estimation are Least Squares and the Kalman Filter, both of which have a variety of forms and are applicable to different situations. Some of the variations of Least squares include: batch, sequential, weighted, nonlinear, and maximum-likelihood; however, all forms of Least squares 'minimize the sum of the squares of the residuals'. The residuals will be the difference in the actual observations and those obtained using the state vector solution [16]. For a more detailed discussion on Least Squares and its variants see [19].

Rudolf E. Kalman's contribution combined statistical mathematics with linear system theory to produce a recursive algorithm for computing 'maximum-likelyhood' estimates of a system state. The principle of maximum-likelihood seeks to find an estimate of the state that maximizes the probability of having obtained the given observational data set. Simply speaking, the Kalman filter is a technique for computing

the best estimate of the state of a time-varying process (i.e. a dynamical system). It uses a predictor-corrector technique ideally suited for computer applications, given imperfect observations and uncertain dynamics. It differs from the Least-Squares technique in two ways. First, it continuously updates the epoch time, thus estimating the state at each successive observation time. Of course this assumes we have data available over a period of time. Second, it carries all the information concerning the past measurements in its current state and covariance estimates and therefore doesn't need to reprocess all of the past measurement information at each step [16].

The Kalman filter works well for linear systems, but all real-world systems are inherently nonlinear so the Kalman filter's effectiveness is reduced. However, the Extended Kalman Filter (EKF) attempts to filter nonlinear systems by linearizing the system dynamics through a first-order Taylor series expansion. This method is generally effective (assuming frequent updates) and is widely used in practice.

The Kalman filter and Extended Kalman filter have advantages and disadvantages when compared to least squares and sequential least squares. Some of the advantages are [16]:

- It's not limited by the accuracy of the force models in the fit span, but it is still constrained during subsequent propagation.
- It's a very fast, recursive process that is ideally suited for real-time control of a system because it doesn't require iteration (Viking Lander, Apollo Lunar Landers, Missiles).
- It may require less memory storage and processor time, but that depends on the computer software. Because the filter uses more frequent updates, we can use less accurate propagation models in some situations.
- It allows solving for measurement biases simultaneously in the state space, which accommodates the true time-varying bias (if the bias is observable enough).

- It is more adept at modeling time-varying coefficients such as of drag and solar-radiation pressure (assuming the quantities are observable enough).

3.2 Continuous-Discrete Extended Kalman Filter

Even with the EKF there are several possible variations applicable for estimation: the continuous-EKF (dynamics and measurements are considered continuous), continuous-discrete EKF (continuous dynamics, discrete updates), discrete-discrete (dynamics updated at discrete time intervals and measurements are taken at discrete time intervals). Continuous-discrete EKF models were applied to each sensor used in this thesis (GPS, vision, attitude) to calculate state and parameter estimates of the Pursuer satellite. Because the system dynamics are treated as continuous rather than discrete they must be numerically integrated.

A general Continuous-Discrete EKF consists of five components: the model, initialization, calculation of the gain, update the estimated state vector and covariance, and propagating the estimated state and covariance.

Continuous-Discrete EKF Model: The model consists of the true system dynamics and the measurement model. The system's true dynamics can be generalized as

$$\dot{\mathbf{x}}(t) = \mathbf{f}(\mathbf{x}(t), \mathbf{u}(t), t) + G(t)\mathbf{w}(t), \ \mathbf{w}(t) \sim N(\mathbf{0}, Q(t)) \tag{3.1}$$

where $\mathbf{f}(\mathbf{x}(t), \mathbf{u}(t), t)$ is the noiseless dynamics and $\mathbf{w}(t)$ is the process noise with zero mean and standard deviation $Q(t)$ (i.e. $E\left\{\mathbf{w}_k \mathbf{w}_j^T\right\} = \begin{cases} 0 & k \neq j \\ Q_k & k = j \end{cases}$). Process noise, $\mathbf{w}$, is a mathematical model of the errors in the system dynamics and quantifies the ability to accurately model the actual dynamics before and after a given epoch

[16]. It should be noted that in general the process noise is very hard to model and the filter's performance could degrade or even diverge if enough process noise is present.

The measurement model for any sensor at some iteration k can be generalized as

$$\tilde{\mathbf{y}}_k = \mathbf{h}\left(\mathbf{x}_k\right) + \mathbf{v}_k,\ \mathbf{v}_k \sim N\left(\mathbf{0}, R_k\right) \tag{3.2}$$

where $\tilde{\mathbf{y}}_k$ is the k^{th} measurement, $\mathbf{h}\left(\mathbf{x}_k\right)$ is the measurement model at the k^{th} iteration, and $\mathbf{v}_k$ is the measurement noise which is assumed to be zero mean and have a standard deviation of R_k (i.e. $E\left\{\mathbf{v}_k \mathbf{v}_j^T\right\} = \begin{cases} 0 & k \neq j \\ R_k & k = j \end{cases}$). It must also be stated that $\mathbf{w}_k$ and $\mathbf{v}_k$ are assumed to be uncorrelated so that $E\left\{\mathbf{v}_k \mathbf{w}_k^T\right\} = 0$ for all k.

Continuous-Discrete EKF Initialization: One of the drawback to all forms of Kalman filtering is the initial estimated state and covariance must be initialized by some other means than the filter. If the initial state of the system is not well known then a poor initial estimate could result and lead to filter instability or divergence. The same issue could arise if the initial covariance is too small and the initial errors lie outside the radius of convergence. The estimated state and covariance are generally initialized as

$$\begin{aligned} \hat{\mathbf{x}}\left(t_0\right) &= \hat{\mathbf{x}}_0 \\ P_0 &= E\left\{\tilde{\mathbf{x}}\left(t_0\right) \tilde{\mathbf{x}}^T\left(t_0\right)\right\} \end{aligned} \tag{3.3}$$

Continuous-Discrete EKF Gain: The Kalman gain is the primary parameter governing the measurement update process and can be computed as

$$K_k = P_k^- H_k^T\left(\hat{\mathbf{x}}_k^-\right)\left[H_k\left(\hat{\mathbf{x}}_k^-\right) P_k^- H_k^T\left(\hat{\mathbf{x}}_k^-\right) + R_k\right]^{-1} \tag{3.4}$$

where K_k is the gain, P_k^- is the pre-update covariance at the k^{th} iteration, R_k is the measurement noise matrix, and $H_k\left(\hat{\mathbf{x}}_k^-\right)$ is the observation or basis function matrix.

The observation matrix is a function of the pre-updated state estimate $\hat{\mathbf{x}}_k^-$ and is given by

$$H_k\left(\hat{\mathbf{x}}_k^-\right) \equiv \left.\frac{\partial \mathbf{h}}{\partial \mathbf{x}}\right|_{\hat{\mathbf{x}}_k^-} \tag{3.5}$$

Continuous-Discrete EKF Update: After the gain has been calculated the estimated state vector and its corresponding covariance at the k^{th} iteration can be updated by

$$\hat{\mathbf{x}}_k^+ = \hat{\mathbf{x}}_k^- + K_k\left[\tilde{\mathbf{y}}_k - \mathbf{h}\left(\hat{\mathbf{x}}_k^-\right)\right] \tag{3.6a}$$

$$P_k^+ = \left[I - K_k H_k\left(\hat{\mathbf{x}}_k^-\right)\right] P_k^- \tag{3.6b}$$

$\hat{\mathbf{x}}_k^+$ is the updated state vector, $\hat{\mathbf{x}}_k^-$ is the estimated state vector before the update, I is an identity matrix of proper dimensions and the quantity $\left[\tilde{\mathbf{y}}_k - \mathbf{h}\left(\hat{\mathbf{x}}_k^-\right)\right]$ is known as the residual error. The covariance matrix contains the estimates for the closeness of the fit with the chosen dynamics. The diagonal terms are the variances of the estimated state parameters and the square roots of the diagonal terms are the corresponding standard deviations. The off-diagonal elements are called the covariance terms and represent the degree of correlation among the elements, with zero being no correlation. Positive signs indicate a direct correlation, while negative signs imply an inverse relationship. It is desired that all off-diagonal terms are zero or nearly zero [16]. The state propagation and discrete update method of the continuous-discrete EKF is visualized in Figure 3.1

Continuous-Discrete EKF Propagation: Once the state and covariance have been updated they can be propagated forward in time to the next iteration step. As stated before the filter of choice for this study is a Continuous-Discrete EKF so the state and covariance must be numerically integrated. The propagation model for

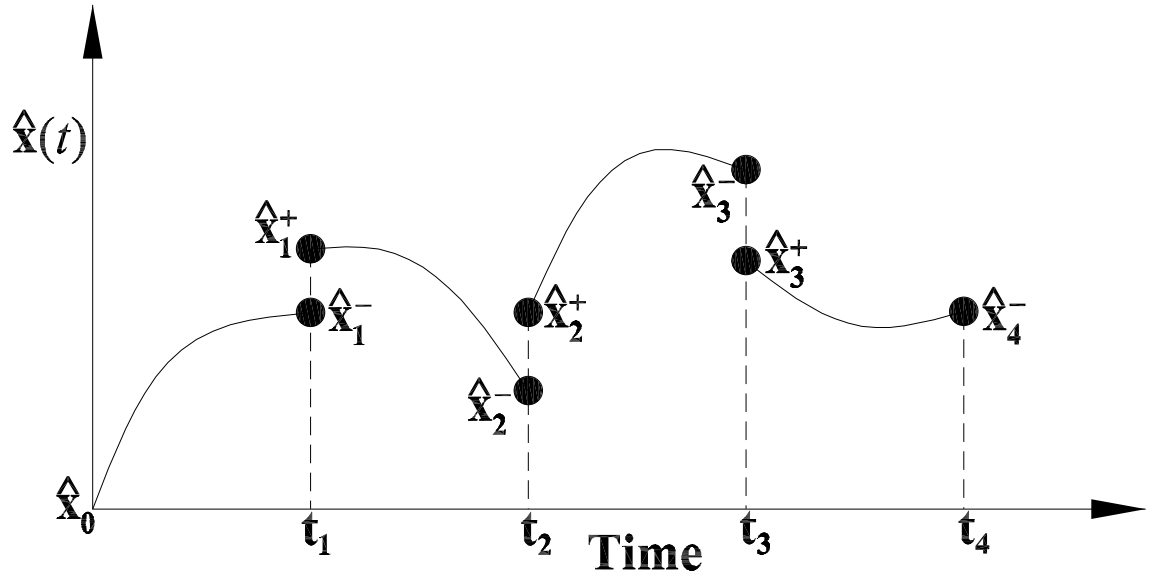

Figure 3.1 Mechanism for the Continuous-Discrete Kalman Filter.

the estimated state is the same as the truth model except there is no process noise and estimated parameters are used rather than true parameters.

$$\dot{\hat{\mathbf{x}}}(t) = \mathbf{f}(\hat{\mathbf{x}}(t), \mathbf{u}(t), t) \tag{3.7}$$

The covariance is propagated by integrating

$$\dot{P}(t) = F(\hat{\mathbf{x}}(t), t) P(t) + P(t) F^T(\hat{\mathbf{x}}(t), t) P(t) + G(t) Q(t) G^T(t) \tag{3.8}$$

where F is the partial of the estimated state dynamics with respect to the state and is given by

$$F(\hat{\mathbf{x}}(t), t) \equiv \left.\frac{\partial \mathbf{f}}{\partial \mathbf{x}}\right|_{\hat{\mathbf{x}}^-(t)} \tag{3.9}$$

The EKF process is recursive, therefore at the end of the propagation phase the process will start over with a new measurement at the $k+1$ iteration and then follow

with a new calculated gain, update the state and covariance again, and propagate the state and covariance forward again. The primary difference between the first loop through the EKF and subsequent iterations is the state and covariance initialization will have already taken place in the prior iteration. The continuous-discrete EKF model is summarized in Table 3.1

Table 3.1 Continuous-Discrete Extended Kalman Filter

Model	$\dot{\mathbf{x}}(t) = \mathbf{f}(\mathbf{x}(t), \mathbf{u}(t), t) + G(t)\mathbf{w}(t), \quad \mathbf{w}(t) \sim N(\mathbf{0}, Q(t))$ $\tilde{\mathbf{y}}_k = \mathbf{h}(\mathbf{x}_k) + \mathbf{v}_k, \quad \mathbf{v}_k \sim N(\mathbf{0}, R_k)$
Initialize	$\hat{\mathbf{x}}(t_0) = \hat{\mathbf{x}}_0$ $P_0 = E\left\{\tilde{\mathbf{x}}(t_0)\tilde{\mathbf{x}}^T(t_0)\right\}$
Gain	$K_k = P_k^- H_k^T\left(\hat{\mathbf{x}}_k^-\right)\left[H_k\left(\hat{\mathbf{x}}_k^-\right)P_k^- H_k^T\left(\hat{\mathbf{x}}_k^-\right) + R_k\right]^{-1}$ $H_k\left(\hat{\mathbf{x}}_k^-\right) \equiv \frac{\partial \mathbf{h}}{\partial \mathbf{x}}\Big\vert_{\hat{\mathbf{x}}_k^-}$
Update	$\hat{\mathbf{x}}_k^+ = \hat{\mathbf{x}}_k^- + K_k\left[\tilde{\mathbf{y}}_k - \mathbf{h}\left(\hat{\mathbf{x}}_k^-\right)\right]$ $P_k^+ = \left[I - K_k H_k\left(\hat{\mathbf{x}}_k^-\right)\right]P_k^-$
Propagation	$\dot{\hat{\mathbf{x}}}(t) = \mathbf{f}(\hat{\mathbf{x}}(t), \mathbf{u}(t), t)$ $\dot{P}(t) = F(\hat{\mathbf{x}}(t), t)P(t) + P(t)F^T(\hat{\mathbf{x}}(t), t) + G(t)Q(t)G^T(t)$ $F(\hat{\mathbf{x}}(t), t) \equiv \frac{\partial \mathbf{f}}{\partial \mathbf{x}}\Big\vert_{\hat{\mathbf{x}}^-(t)}$

The next three chapters will discuss the sensors utilized for the rendezvous simulation in this study: GPS, vision, attitude. Each chapter will give a brief description of a sensor system and give the model to how measurements were simulated and how the EKF was implemented for that sensor system.

CHAPTER 4

GPS NAVIGATION

The Global Positioning System (GPS) was originally developed for the U.S. military to enable determination of position and time for military troops and guided missiles. Over time, however, the GPS has spread into civilian applications and become a basis for position and time measurements in the scientific community and in a multi-billion dollar commercial industry.

Interest in the application of the GPS to spacecraft navigation and attitude determination has grown significantly in recent years [19]; this chapter briefly describes the Global Positioning System, some of the advantages and disadvantages of GPS navigation, the assumptions made for simulation purposes, and the mathematical models used to simulate the GPS constellation and generate simulated GPS measurements.

4.1 GPS Constellation

Positions and velocities of GPS satellites are required for simulation of GPS pseudorange measurements. This section presents a description of the GPS constellation model used in this thesis and the equations needed to determine the positions and velocities of the satellites within the constellation.

The Global Positioning System has three segments: the space segment, the control segment, and the user segment. In the space segment, a varying number[1] of satellites spread equally over six orbital planes are orbiting the earth in nearly

[1]The exact number of satellites operating at any one particular time varies depending on the number of satellite outages and operational spares in orbit [20].

circular 12-hour orbits at 55° inclinations. The control segment consists of centers that collect ground station tracking data, calculate satellite ephemerides and clock corrections using a Kalman filter, and then upload the data to the satellites. The user segment consists of GPS receivers and the user community. The GPS receivers convert the satellites' signals into position, velocity, and time estimates for navigating, positioning, distributing time, or geodesy [16].

The GPS constellation of this study was constructed from NORAD Two-Line Element Sets (TLE) given on the CelesTrak website [21]. TLE contain orbital data for a satellite, embedded in a set of two lines that include the satellite's inclination, right ascension of the ascending node, eccentricity, argument of perigee, mean anomaly, and mean motion at a given epoch. From this data, a satellite's position and velocity at the given epoch time can be extracted. The epoch time for each TLE is not necessarily the same, however – so each satellite's orbital position must be propagated to a common specific time, or the constellation formation will not be maintained. TLE data was taken for 29 operational GPS satellites on April 19, 2005 and all of the satellites' orbits were propagated forward to midnight Coordinated Universal Time (UTC) on April 20, 2005.

4.2 GPS Signals

Each satellite within the GPS constellation transmits navigation signals on two L-band frequencies, called L_1 (1575.42 MHz) and L_2 (1227.60 MHz), upon which two pseudorandom noise PRN-codes (the C/A-Code and the P-Code) are superimposed. Each GPS satellite's PRC is unique, guaranteeing the receiver will not confuse multiple incoming signals. Serving as the basis for civilian use is the Coarse Acquisition (C/A) code which is the modulated PRC at the L_1 carrier, repeating 1023 bits and modulating at a 1MHz rate. Another PRC, the Precise (P) code, which repeats on a

seven-day cycle and modulates both the L_1 and L_2 carriers 10MHz rate, is intended for military use and can be encrypted. Position determination is made possible by comparing how late in time the GPS's PRC appears to the receiver's code. Multiplying the travel time by the speed of light, one obtains the distance to the GPS satellite. This requires very accurate timing in the receiver, which is provided by using a fourth GPS satellite to correct a 'clock bias' in the internal clock receiver [19].

4.3 GPS Error Sources

Many error sources affect GPS accuracy using PRC. GPS signals may slow down as they pass through charged particles in the ionosphere or through water vapor in the troposphere. Solar flares may cause GPS receivers to fail. Signals may bounce off local obstructions before arriving at the receiver (known as multipath errors), or may be completely blocked by obstructions (blockage). Ephemeris (or known satellite position errors) can contribute to location inaccuracy as well. In another potential error source, Geometric Dilution of Precision (GDOP), GPS sightlines to the receiver can be near colinear and result in degraded accuracy [19].

Because the GPS system is very complex, several assumptions were made to simplify the GPS navigation model, including:

- GPS receivers are all-in-view, meaning all GPS satellites within line of sight[2] are tracked and used for measurement.

[2]Assume you know two arbitrary vectors ($\mathbf{a}$ and $\mathbf{b}$). Using the dot product, the cosine of the angle between the two vectors is: $\cos(\theta) = \frac{\mathbf{a}\cdot\mathbf{b}}{|\mathbf{a}||\mathbf{b}|}$ If you now fix the maximum perpendicular distance between the central point and the line-of-sight vector to 1 Earth Radius, you can determine two half angles θ_1 and θ_2. These angles are given by $\cos(\theta_1) = \frac{1}{|\mathbf{a}|}$ and $\cos(\theta_2) = \frac{1}{|\mathbf{b}|}$ No quadrant check is required because all the angles are less than 180°. If the sum of $\theta_1 + \theta_2 \leq \theta$, there is no line-of-sight. For more information see [16].

- GPS receivers are able to instantly acquire and lock on to new GPS satellites as they become visible, but receivers will also immediately lose the signal from a GPS satellite when it passes out of line-of-sight.
- The line-of-sight model used assumes a spherical Earth.
- Errors due to multipath and blockage were ignored.
- Errors from receiver noise and atmospheric effects were all grouped into the measurement noise.

4.4 GPS Navigation Measurement Equations

A minimum of four GPS satellites are required so that, in addition to the three-dimensional position of the user, the time of the solution can be determined and used to correct the user's clock. The GPS pseudorange measurements are assumed to be modeled as

$$\tilde{\rho}_i = \sqrt{(e_{1i} - X)^2 + (e_{2i} - Y)^2 + (e_{3i} - Z)^2} + \tau + v_i \quad i = 1, 2, ..., n \tag{4.1}$$

$\tilde{\rho}_i$ is the measured pseudorange from the i^{th} GPS satellite, $\{e_{1i}, e_{2i}, e_{3i}\}$ are the ECI coordinates of the i^{th} GPS satellite, $\{X, Y, Z\}$ are the inertial coordinates of the satellite being measured, τ is the clock bias[3] assumed to be the same for all GPS satellites, v_i is the measurement noise which is assumed to be a zero-mean Gaussian noise process with variance σ^2 and σ is assumed to be the same for all GPS satellites and n is the number of observable GPS satellites. It was assumed that the GPS clock

[3]Biases are a constant offset from the 'true' value, wheras noise is a statistical indication (actually a standard deviation) of the random variation about the measured mean. In other words, noise is scattering about the observed mean value. Drift represents a slow and unpredictable variation over time of the observed mean value over an interval of time. The nice feature of biases is that, if we known them, we can simply subtract them from each observation [16].

bias could be modeled as a random walk process such that the truth model is given by

$$\dot{\tau}\left(t\right) = w_{\tau}\left(t\right)$$

where $w_{\tau}\left(t\right)$ is assumed to be a zero-mean Gaussian noise process with known variance Q_{bias}

The estimated pseudorange is obtained similarly to the measured pseudorange by

$$\hat{\rho}_i = \sqrt{\left(e_{1i} - \hat{X}\right)^2 + \left(e_{2i} - \hat{Y}\right)^2 + \left(e_{3i} - \hat{Z}\right)^2} + \hat{\tau} \quad i = 1, 2, ..., n \tag{4.2}$$

where $\hat{\rho}_i$ is the estimated pseudorange, $\left\{\hat{X}, \hat{Y}, \hat{Z}\right\}$ are the estimated ECI coordinates of the satellite being measured, and $\hat{\tau}$ is the estimated clock bias. In terms of the general EKF discussed in Chapter 3, $\tilde{\rho}_i$ in (4.1) is the measured value $\tilde{\mathbf{y}}_k$ in (3.2) and $\hat{\rho}_i$ in (4.2) is $\mathbf{h}\left(\hat{\mathbf{x}}_k^-\right)$ in (3.6a).

4.5 State Estimation from GPS Pseudorange Measurements

An extended Kalman filter (EKF) was implemented to estimate the joint state vector involving the states and the parameters, $\mathbf{x}_{GPS}$. The joint state vector estimated by GPS measurements included the inertial position and velocity of the Pursuer, GPS clock bias, τ, the J_2 coefficient, and the Pursuer's ballistic coefficient, B with $B = \frac{c_D A}{m}$.

$$\mathbf{x}_{GPS} = \begin{bmatrix} X_P & X_P & Z_P & \dot{X}_P & \dot{Y}_P & \dot{Z}_P & \tau & J_2 & B \end{bmatrix}^T$$

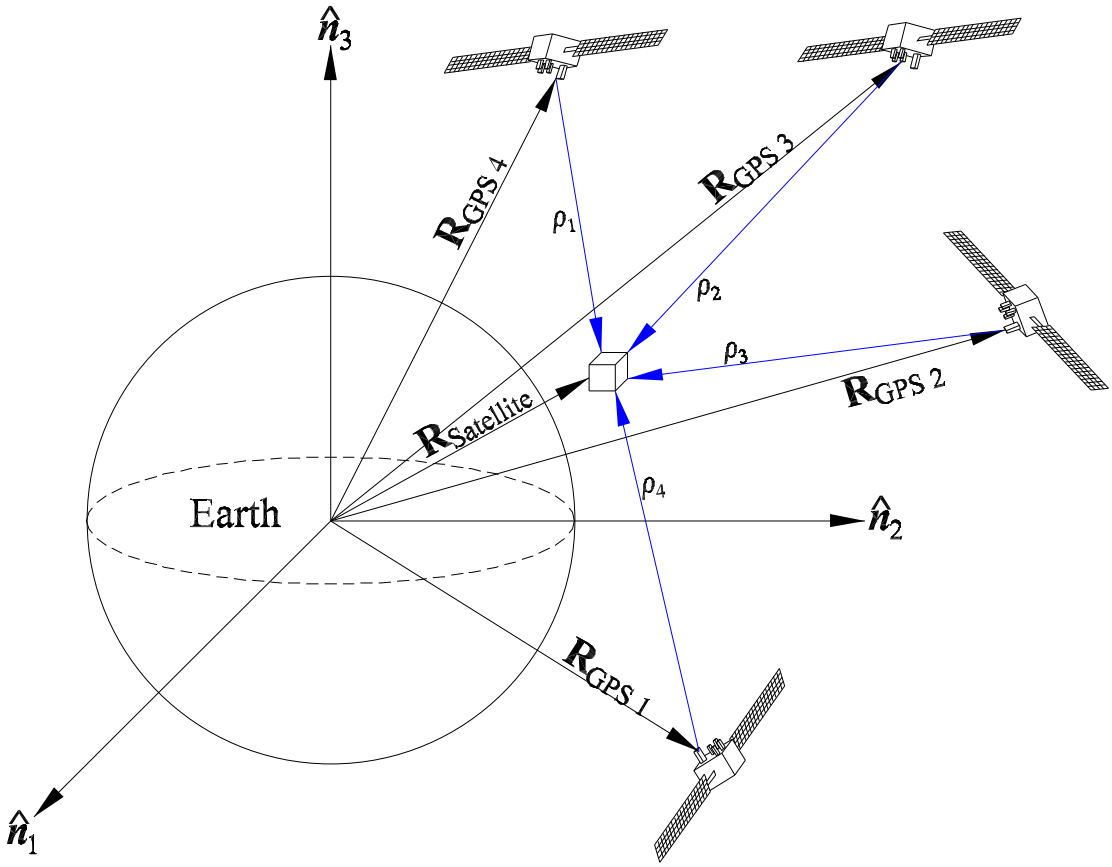

Figure 4.1 General setup for GPS pseudorange measurements.

For GPS pseudorange measurements the observation matrix used to calculate the Kalman gain and covariance update in (3.4) and (3.6b) is given by

$$H_k\left(\hat{\mathbf{x}}_k^-\right) = \left.\frac{\partial \hat{\rho}}{\partial \mathbf{x}_{GPS}}\right|_{\hat{\mathbf{x}}(t)} = \begin{bmatrix} \frac{\partial \hat{\rho}_1}{\partial \hat{x}} & \frac{\partial \hat{\rho}_1}{\partial \hat{y}} & \frac{\partial \hat{\rho}_1}{\partial \hat{z}} & 0 & 0 & 0 & 1 & 0 & 0 \\ \frac{\partial \hat{\rho}_2}{\partial \hat{x}} & \frac{\partial \hat{\rho}_2}{\partial \hat{y}} & \frac{\partial \hat{\rho}_2}{\partial \hat{z}} & 0 & 0 & 0 & 1 & 0 & 0 \\ \vdots & \vdots & \vdots & \vdots & \vdots & \vdots & \vdots & \vdots & \vdots \\ \frac{\partial \hat{\rho}_n}{\partial \hat{x}} & \frac{\partial \hat{\rho}_n}{\partial \hat{y}} & \frac{\partial \hat{\rho}_n}{\partial \hat{z}} & 0 & 0 & 0 & 1 & 0 & 0 \end{bmatrix} \tag{4.3}$$

where the partials of the pseudorange estimates that form the first three columns of H_k are

$$\frac{\partial \hat{\rho}_i}{\partial \hat{X}} = -\frac{\left(e_{1i}-\hat{X}\right)}{\sqrt{\left(e_{1i}-\hat{X}\right)^2+\left(e_{2i}-\hat{Y}\right)^2+\left(e_{3i}-\hat{Z}\right)^2}}$$
$$\frac{\partial \hat{\rho}_i}{\partial \hat{Y}} = -\frac{\left(e_{2i}-\hat{Y}\right)}{\sqrt{\left(e_{1i}-\hat{X}\right)^2+\left(e_{2i}-\hat{Y}\right)^2+\left(e_{3i}-\hat{Z}\right)^2}}$$
$$\frac{\partial \hat{\rho}_i}{\partial \hat{Z}} = -\frac{\left(e_{3i}-\hat{Z}\right)}{\sqrt{\left(e_{1i}-\hat{X}\right)^2+\left(e_{2i}-\hat{Y}\right)^2+\left(e_{3i}-\hat{Z}\right)^2}}$$

After the gain, K_k, has been calculated, the updated state estimate, $\hat{\mathbf{x}}_k^+$, and updated covariance, P_k^+, can be calculated at discrete instants by (3.6). Once $F_{GPS} = \frac{\partial \dot{\hat{\mathbf{x}}}_{GPS}}{\partial \hat{\mathbf{x}}_{GPS}}$ (given in appendix B) has been calculated, the state and covariance are propagated between discrete measurement instants by numerically integrating the equations of motion given in (2.29) and (3.8). The matrices associated with process noise and needed for the covariance propagation are given by

$$G_{GPS} = \begin{bmatrix} \mathbf{0}_{3\times 3} & \mathbf{0}_{3\times 1} \\ I_{3\times 3} & \mathbf{0}_{3\times 1} \\ \mathbf{0}_{3\times 3} & \begin{bmatrix} 1 & 0 & 0 \end{bmatrix}^T \end{bmatrix}$$
$$Q_{GPS} = diag\left(\alpha_i\right) I_{4\times 4}$$

where α_i are appropriate positive tuning parameters.

This chapter has described the GPS sensor system and developed the measurement and estimation models used for simulation purposes in this thesis. The next chapter will give a similar discussion for the vision based navigation system.

CHAPTER 5

VISION-BASED NAVIGATION

5.1 Vision-Based Navigation System Setup

Vision-based navigation is a relatively new potential form of relative navigation and attitude determination. In general the system consists of a camera sensor and light beacons. An illustration of the vision-based sensor setup is provided in Fig. 5.1. The camera sensor and light beacons are both stationary and at known locations with respect to the P-frame and T-frame respectively. The camera sensor 'sees' the beacons from the light landing on the image plane and can measure the relative distance between the two bodies from the location of the landing on the image plane (x_i, z_i).

A few advantages of this type of navigation system is that it can be used at any location (i.e. between cars on a road, two planes refueling in midair, two spacecraft in orbit about Mars, etc.) and it can provide very accurate (within a few cm) relative position, velocity, and attitude estimates. However, this system has range problems due to the beacons reaching collinearity as the relative separation grows [14].

The vision-based navigation system utilized for the autonomous rendezvous and docking of the Pursuer and Target system is similar to the model found in [13]. In that paper, measurements from the vision-based system were used to estimate relative position as well as attitude using a Gaussian Least Squares Differential Correction algorithm (GLSDC). In this study the vision sensor setup and measurement model provided estimates of the relative position and relative velocity through the use of an Extended Kalman Filter algorithm.

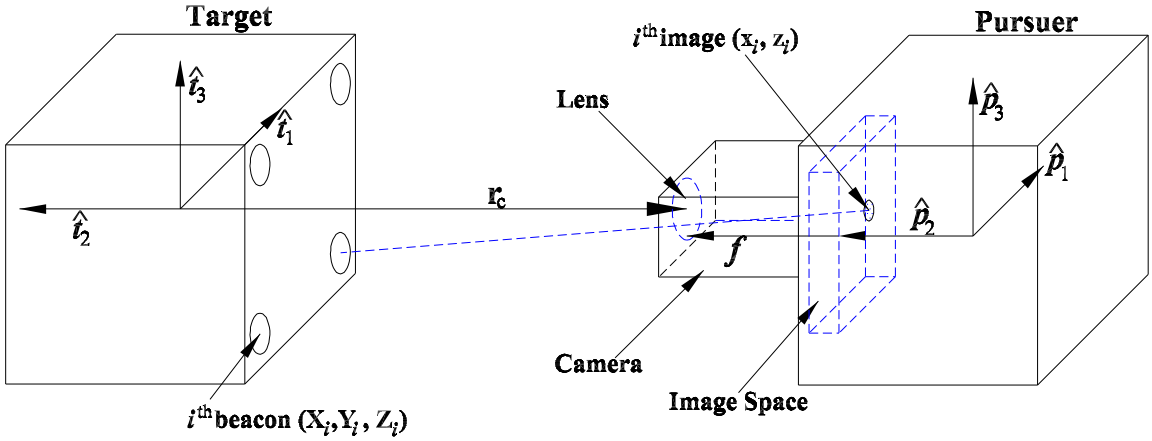

Figure 5.1 Vision-Based Navigation Setup.

5.2 Vision Based Navigation Measurement Model

In this study it was assumed that vision sensor was initially turned off (due to range limitations) and the initial estimates for the vision sensor's EKF process were provided by the GPS estimation process.

Active beacons are assumed to be mounted on the Target with the number of beacons being n (four beacons are shown in Figure 5.1 because four beacons were used in the simulations) and the position of each beacon is known in T-frame components. *Note: Four beacons is also the minimum number that can achieve a unique solution for attitude and position determination.* The position of the i^{th} beacon is given by the object space (T-frame) coordinates $\{X_i, Y_i, Z_i\}$.

The electro-optical sensor is a camera mounted on the Pursuer with a focal length f. The body fixed frame attached to the Pursuer (P-frame) is defined such that the image plane of the camera coincides with the $(\hat{p}_1, \hat{p}_3)$ plane and the vector to the center of the lens is known and given by $\mathbf{f} = f\hat{p}_2$. The vector $\mathbf{r_c}$ is the radius vector from the T-frame to the center of the camera lens and is generalized in the T-frame as $\mathbf{r}_c = X_c\hat{t}_1 + Y_c\hat{t}_2 + Z_c\hat{t}_3$. The centroid of the incident light from the i^{th}

beacon is located on the image plane at coordinates (x_i, z_i). The ideal (i.e. noiseless) transformation projection from the object space to the centroid of the coordinates in the image space is given by the collinearity equations

$$\begin{aligned} x_i &= -f\frac{C_{11}(X_i-X_c)+C_{12}(Y_i-Y_c)+C_{13}(Z_i-Z_c)}{C_{21}(X_i-X_c)+C_{22}(Y_i-Y_c)+C_{23}(Z_i-Z_c)} \\ z_i &= -f\frac{C_{31}(X_i-X_c)+C_{32}(Y_i-Y_c)+C_{33}(Z_i-Z_c)}{C_{21}(X_i-X_c)+C_{22}(Y_i-Y_c)+C_{23}(Z_i-Z_c)} \end{aligned} \qquad i = 1, 2, ..., n \tag{5.1}$$

where C_{xx} are terms in the direction cosine matrix from the object frame to the sensor frame ($C = [PT]$), and $\{X_c, Y_c, Z_c\}$ are the components of the camera lens' position which is known in the P-frame.

Equation (5.1) can be expressed in unit vector form $\mathbf{h}_i = C\mathbf{r}_i$ where the sensor frame unit vectors are

$$\mathbf{h}_i = \frac{1}{\sqrt{f^2 + x_i^2 + z_i^2}} \begin{bmatrix} f \\ x_i \\ z_i \end{bmatrix} \tag{5.2}$$

and the object frame unit vectors are

$$\mathbf{r}_i = \frac{1}{d_i} \begin{bmatrix} X_i - X_c \\ Y_i - Y_c \\ Z_i - Z_c \end{bmatrix} \tag{5.3}$$

where $d_i = \sqrt{(X_i - X_c) + (Y_i - Y_c) + (Z_i - Z_c)}$. It is important to point out that the unit vector $\mathbf{r_i}$ is not the same as the relative position vector between the Target and the Pursuer.

It is likely that the focal length, f, in (5.2) is a known and constant value and does not need to be measured. Therefore, to save computing power a small

refinement of the above equations is provided. Equation (5.2) can be expressed in a more convenient form by

$$\mathbf{h}_i = D\mathbf{r}_i \tag{5.4}$$

where

$$D = \begin{bmatrix} C_{11} & C_{12} & C_{13} \\ C_{31} & C_{32} & C_{33} \end{bmatrix}$$

To construct the full set of measurements from n beacons at each instant, k, the measurement vector from each beacon can be stacked in a column vector $\mathbf{b}_k = \left[\mathbf{h}_1^T, \mathbf{h}_2^T, \ldots, \mathbf{h}_n^T\right]^T$. The measurement is modeled by

$$\tilde{\mathbf{b}}_k = \mathbf{b}_k + \mathbf{v}_k \tag{5.5}$$

where $\mathbf{v}_i$ is a zero-mean Gaussian noise with covariance R.

5.3 State Estimation from Vision Based Navigation Measurements

To yield estimates of the relative position and velocity between the Target and Pursuer an Extended Kalman Filter is implemented. The estimated state vector for this system contained the relative position and velocity in O-frame components

$$\hat{\mathbf{x}}_{vision} = \begin{bmatrix} {}^{O}x & {}^{O}y & {}^{O}z & {}^{O}\dot{x} & {}^{O}\dot{y} & {}^{O}\dot{z} \end{bmatrix}^T$$

The vision's system dynamics, $\dot{\mathbf{x}}$, is the relative motion between the satellites given in equation (2.30).

The gain for the vision sensor's EKF is computed by equation (3.4) where the observability matrix is given by

$$H_k = \begin{bmatrix} H_1^T & H_2^T & \cdots & H_n^T \end{bmatrix}^T \tag{5.6}$$

and the individual elements of H_k are given by

$$H_i = \frac{\partial \mathbf{h}_i}{\partial \mathbf{x}_{vision}} = \begin{bmatrix} -D\frac{I_{3\times3} - \mathbf{r}_i\mathbf{r}_i^T}{d_i} & \mathbf{0}_{2\times3} \end{bmatrix}$$

The state and covariance are then updated for the vision EKF by using equation (3.6) and the resulting updates are propagated to the next iteration through equations (2.30) and (3.8). The matrices dealing with process noise and needed for the covariance propagation, G and Q are given below and $F_{vision} = \frac{\partial \dot{\hat{\mathbf{x}}}_{vision}}{\partial \hat{\mathbf{x}}_{vision}}$ is given in appendix B.

$$G_{vision} = \begin{bmatrix} \mathbf{0}_{3\times3} & \mathbf{0}_{3\times3} \\ \mathbf{0}_{3\times3} & I_{3\times3} \end{bmatrix}$$

$$Q_{vision} = \alpha \left[I_{6\times6} \right]$$

where α is an appropriate tuning parameter.

This and the previous chapter have established sensor systems and models to provide position and velocity determination but no sensor model has been established for attitude determination, an integral part of the control algorithm to engage in the rendezvous. The next chapter will describe the attitude estimation system used in this study.

CHAPTER 6

ATTITUDE ESTIMATION

Applying attitude estimation in this study was more for completeness of the simulation than the focus of the study. The focus of this thesis is to study sensor fusion covered in the next chapter.

Many sensors have been developed to allow satellites to determine their attitude while in orbit such as: star cameras, sun sensors, magnetometers, GPS, and rate-integrating gyros; gyros are also frequently used to estimate a vehicle's rotational velocity.

To control a rigid-body's attitude using the PD controller described in Chapter 2 the attitude and its rate of change must be known. This in turn requires that the rotational velocity of the body be known (for calculation of the attitude rate of change). Rather than create two separate models, one for attitude estimation one for rotational velocity estimation, a hybrid model was created to estimate the satellite's attitude and the gyro bias.

6.1 Attitude & Gyro Measurement Models

Attitude measurements were assumed to be measured directly such as

$$\tilde{\boldsymbol{\sigma}}_P = \boldsymbol{\sigma}_P + \mathbf{v} \tag{6.1}$$

where $\tilde{\boldsymbol{\sigma}}_P$ is the measured attitude (in MRP form), $\boldsymbol{\sigma}_P$ is the Pursuer's true attitude, and $\mathbf{v}$ is a zero-mean Gaussian white noise process with known covariance R.

Gyro measurements for the Pursuer were assumed to be measured in the form

$$\tilde{\boldsymbol{\omega}}_{P/N} = \boldsymbol{\omega}_{P/N} + \boldsymbol{\beta} + \boldsymbol{\eta}_v \tag{6.2a}$$

$$\dot{\boldsymbol{\beta}} = \boldsymbol{\eta}_u \tag{6.2b}$$

where $\tilde{\boldsymbol{\omega}}_{P/N}$ is the measured rotational velocity of the P-frame with respect to the inertial frame, $\boldsymbol{\omega}_{P/N}$ is the true rotational velocity, $\boldsymbol{\beta}$ is the gyro bias vector, and $\boldsymbol{\eta}_v$ is the gyro measurement noise which is assumed to be a zero-mean Gaussian white noise process. The gyro bias vector is modeled as a random walk process where $\boldsymbol{\eta}_u$ is a zero-mean Gaussian white-noise process. The covariances of $\boldsymbol{\eta}_v$ and $\boldsymbol{\eta}_u$ are given by $\sigma_v I^2_{3\times 3}$ and $\sigma_u I^2_{3\times 3}$ respectively [22].

The estimated angular velocity is given by

$$\hat{\boldsymbol{\omega}} = \tilde{\boldsymbol{\omega}} - \hat{\boldsymbol{\beta}} \tag{6.3}$$

where $\hat{\boldsymbol{\omega}}$ is the estimated angular velocity, $\tilde{\boldsymbol{\omega}}$ is the measured angular velocity, and $\hat{\boldsymbol{\beta}}$ is the estimated gyro bias which is given by [22]

$$\dot{\hat{\boldsymbol{\beta}}} = \mathbf{0} \tag{6.4}$$

6.2 State Estimation from Attitude and Angular Velocity Measurements

The attitude estimation state contained the Pursuer's MRP attitude terms and the gyro bias.

$$\hat{\mathbf{x}}_{MRP} = \begin{bmatrix} \sigma_1 & \sigma_2 & \sigma_3 & \beta_1 & \beta_2 & \beta_3 \end{bmatrix}^T$$

Measurements for the EKF were computed by

$$\tilde{\mathbf{y}}_{MRP} = H_k\left(\hat{\mathbf{x}}_k^-\right)\mathbf{x}_{MRP} + \mathbf{v} \tag{6.5}$$

where the observation matrix $H_k\left(\hat{\mathbf{x}}_k^-\right)$ is

$$H_k\left(\hat{\mathbf{x}}_k^-\right) = \frac{\partial \boldsymbol{\sigma}_{MRP}}{\partial \hat{\mathbf{x}}_{MRP}} = \begin{bmatrix} I_{3\times3} & \mathbf{0}_{3\times3} \end{bmatrix}$$

The estimated state was computed by

$$\hat{\mathbf{y}}_{MRP} = H_k\left(\hat{\mathbf{x}}_k^-\right)\hat{\mathbf{x}}_{MRP} \tag{6.6}$$

The EKF gains, state, and covariance updates are then computed by the continuous-discrete equations (3.4) and (3.6).

The matrices needed to propagate the covariance are given by [22]

$$\begin{aligned} F &= \begin{bmatrix} \frac{\partial \mathbf{f}}{\partial \boldsymbol{\sigma}} & \frac{\partial \mathbf{f}}{\partial \boldsymbol{\beta}} \\ \mathbf{0}_{3\times3} & \mathbf{0}_{3\times3} \end{bmatrix} \\ G &\equiv \begin{bmatrix} \hat{G}_{11} & \mathbf{0}_{3\times3} \\ \mathbf{0}_{3\times3} & I_{3\times3} \end{bmatrix} \\ Q &= \begin{bmatrix} \sigma_u I_{3\times3} & \mathbf{0}_{3\times3} \\ \mathbf{0}_{3\times3} & \sigma_u^2 I_{3\times3} \end{bmatrix} \end{aligned} \tag{6.7}$$

where [22]

$$\mathbf{f} = \tfrac{1}{2}\left\{\tfrac{1}{2}\left(1-\boldsymbol{\sigma}^T\boldsymbol{\sigma}\right)I_{3\times 3} + [\boldsymbol{\sigma}\times] + \boldsymbol{\sigma}\boldsymbol{\sigma}^T\right\}(\tilde{\boldsymbol{\omega}} - \boldsymbol{\beta})$$

$$\tfrac{\partial \mathbf{f}}{\partial \boldsymbol{\sigma}}\Big|_{\mathbf{x}=\hat{\mathbf{x}}} = \tfrac{1}{2}\left\{\hat{\boldsymbol{\sigma}}\hat{\boldsymbol{\omega}}^T - \hat{\boldsymbol{\omega}}\hat{\boldsymbol{\sigma}}^T - [\hat{\boldsymbol{\omega}}\times] + \left(\hat{\boldsymbol{\omega}}^T\hat{\boldsymbol{\sigma}}\right)I_{3\times 3}\right\}$$

$$\tfrac{\partial \mathbf{f}}{\partial \boldsymbol{\beta}}\Big|_{\mathbf{x}=\hat{\mathbf{x}}} = -\tfrac{1}{2}\left\{\tfrac{1}{2}\left(1-\hat{\boldsymbol{\sigma}}^T\hat{\boldsymbol{\sigma}}\right)I_{3\times 3} + [\hat{\boldsymbol{\sigma}}\times] + \hat{\boldsymbol{\sigma}}\hat{\boldsymbol{\sigma}}^T\right\} \equiv \hat{G}_{11}$$

CHAPTER 7

MULTI-SENSOR FUSION

The previous chapters have described individual sensor systems that are used for navigation and control in this thesis. Both the GPS and vision sensor systems have advantages and disadvantages for navigation, specifically rendezvous, however, it is possible to use multiple sensors in conjunction to improve estimation performance and in turn improve the control performance. Use of multiple sensors in conjunction to create a single global or master estimate of the desired state parameters is known as sensor fusion and is the main focus of this thesis.

Sensor fusion is generally achieved through two means: a centralized filter or a decentralized filter. The following chapter will describe the difference between these two filter types, develop the algorithm for the decentralized filter, and apply that filter to the GPS and vision sensors previously developed to create a global state estimate in the form of a Federated Extended Kalman Filter.

7.1 Centralized Kalman Filter Architecture

A general centralized Kalman filter architecture is depicted in Figure 7.1. In this setup, a series of independent local sensors provide uncorrelated measurements $(\mathbf{Y}_1, \ldots, \mathbf{Y}_N)$ on some larger global system. The measurements from these sensors can be fed to a conventional Kalman filter to obtain an optimal estimate of the global state called a *global* or *centralized Kalman filter*. Although this global filter can provide an optimal linear minimum-variance (LMV) solution to the estimation problem, the large number of states in the global system often requires processing

data rates that cannot be maintained in practical real-time applications. For this reason, and because smaller parallel structures can often provide improved failure detection and correction, improved redundancy management, and lower costs for system integration, there has been considerable recent interest in decentralized (or distributed) Kalman filter architectures [23].

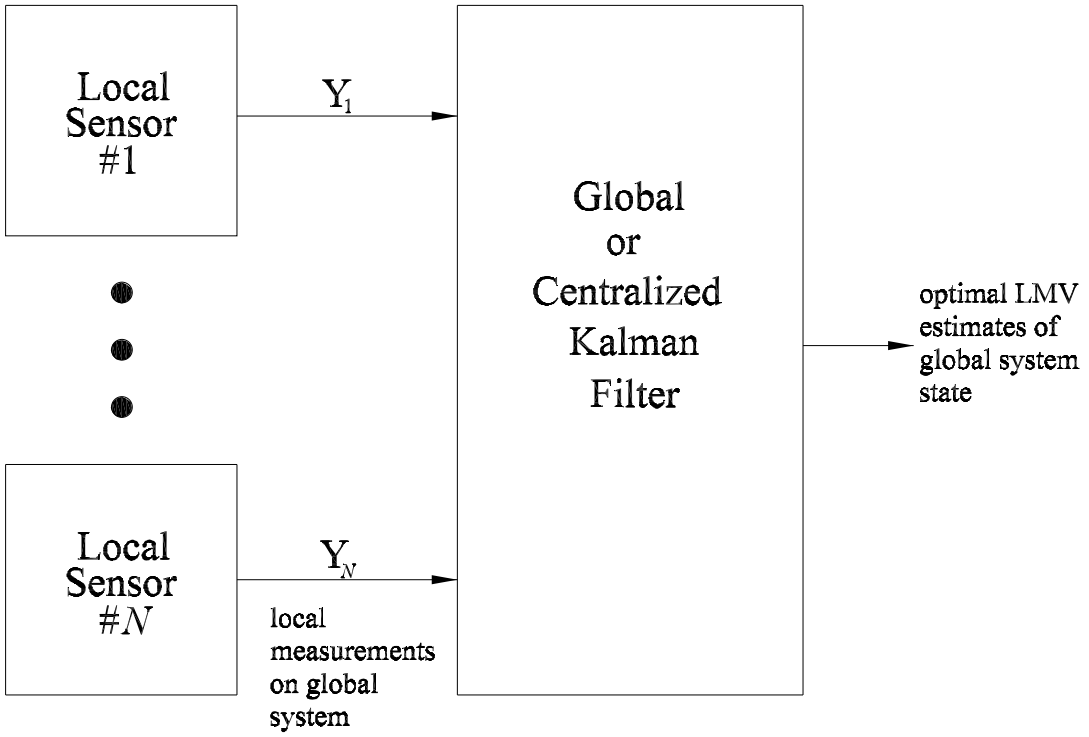

Figure 7.1 Centralized Kalman Filter Architecture.

7.2 Decentralized Kalman Filter Architecture

The basic goal of decentralized Kalman filtering methods has been the determination of efficient parallel processing structures that, like the centralized Kalman filter, provide in some sense optimal estimates of the global system's states. A de-

centralized Kalman filter architecture generally seeks to replace the architecture in Figure 7.1 with one depicted in Figure 7.2. In this architecture each local sensor has a local processor to provide optimal estimates for some subset of the global system state vector. The individual estimates are then passed to the global fusion processor to create an optimal estimate of the global system. If a local system model has the same states as the global system, it is said to have *full-order*. If its states are a smaller subset of the global system states, it is said to have *reduced-order* [23].

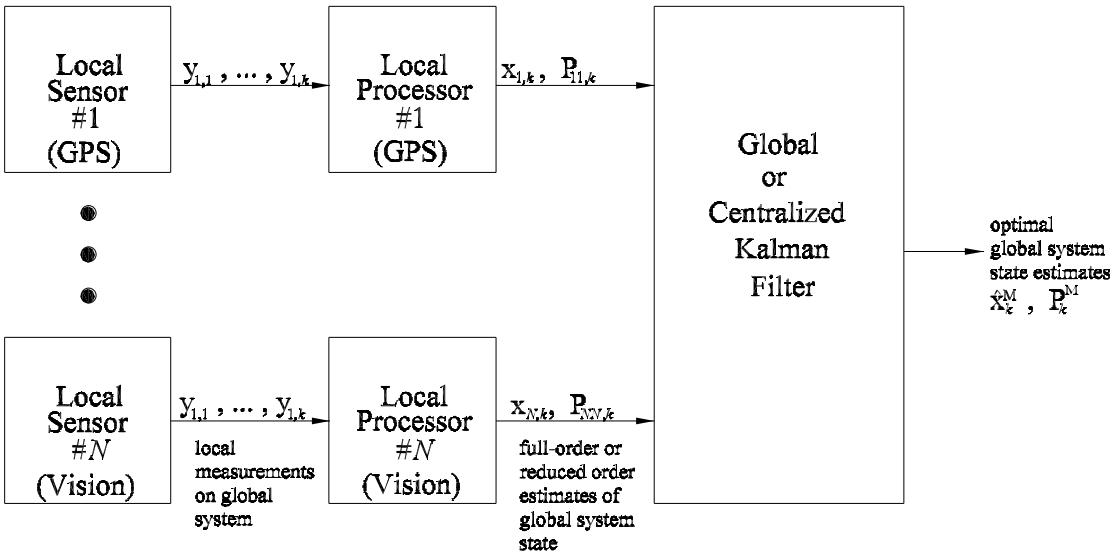

Figure 7.2 Decentralized Kalman Filter Architecture.

The application of decentralized Kalman filtering methods to integrated navigation systems has been well studied and is summarized in Ref [24]. Carlson applied an optimal global fusion procedure, developed in Ref [25] to a decentralized Kalman filter architecture proposed by Kerr in Ref [26] for integrated navigation systems. Although the Federated Kalman Filter (FKF) developed by Carlson is conservatively suboptimal, it forms the basis for the nonlinear state and measurement models used

in this study. Since the state and measurement models dealt with in this study are nonlinear the FKF will be referred to as the Federated Extended Kalman Filter (FEKF).

7.3 The Federated Extended Kalman Filter

The output of the decentralized Kalman filter discussed in the previous section, and illustrated in Figure 7.2, contains different state estimates and error covariance matrices for states that are common to the local systems. That is, in the output of the decentralized Kalman filter, each local filter contributes to its own estimate (and the corresponding error covariance matrix) for the common system states. The federated Kalman filter architecture includes a second stage of processing that provides a means to optimally integrate this common information. This optimal fusion algorithm is described in the following paragraphs.

If it is assumed that all of the local systems contain common state variables the global system state can be expressed as a stack of N common state vectors $\mathbf{x}_{c,k}$ and the master filter global state estimate can be represented as [23]

$$\hat{\mathbf{x}}_k^{\mathbf{M}} = \begin{bmatrix} \hat{\mathbf{x}}_{c,k}^{\mathbf{M}} \\ \vdots \\ \hat{\mathbf{x}}_{c,k}^{\mathbf{M}} \end{bmatrix} \tag{7.1}$$

and the performance index can be expressed as [23]

$$J = \sum_{i=1}^{N} \left(\hat{\mathbf{x}}_{i,k} - \hat{\mathbf{x}}_{c,k}^{\mathbf{M}}\right)^T \mathbf{P}_{ii,k}^{-1} \left(\hat{\mathbf{x}}_{i,k} - \hat{\mathbf{x}}_{c,k}^{\mathbf{M}}\right) \tag{7.2}$$

The performance index achieves its minimum value at the point where its partial derivative with respect to $\hat{\mathbf{x}}_{c,k}^{\mathbf{M}}$ is zero. Then taking the partial of (7.2) with respect

to $\hat{\mathbf{x}}_{c,k}^{\mathbf{M}}$, setting the resultant to zero, and solving for $\hat{\mathbf{x}}_{c,k}^{\mathbf{M}}$ yields the optimal integrated state. The partial derivative of J with respect to $\hat{\mathbf{x}}_{c,k}^{\mathbf{M}}$ can be expressed as [23]

$$2\sum_{i=1}^{N}\mathbf{P}_{ii,k}^{-1}\left(\hat{\mathbf{x}}_{i,k}-\hat{\mathbf{x}}_{c,k}^{\mathbf{M}}\right) \tag{7.3}$$

Setting (7.3) equal to zero and solving for $\hat{\mathbf{x}}_{c,k}^{\mathbf{M}}$ yields the optimal global state estimate

$$\hat{\mathbf{x}}_{c,k}^{\mathbf{M}}=\left(\mathbf{P}_{11,k}^{-1}+\ldots+\mathbf{P}_{NN,k}^{-1}\right)^{-1}\left(\mathbf{P}_{11,k}^{-1}\hat{\mathbf{x}}_{1,k}+\ldots+\mathbf{P}_{NN,k}^{-1}\hat{\mathbf{x}}_{N,k}\right) \tag{7.4}$$

The error covariance matrix for the estimate $\hat{\mathbf{x}}_{c,k}^{\mathbf{M}}$, denoted $\mathbf{P}_{c,k}^{\mathbf{M}}$, can be determined by noting that

$$\begin{aligned}\mathbf{x}_{c,k}-\hat{\mathbf{x}}_{c,k}^{\mathbf{M}}&=\left(\mathbf{P}_{11,k}^{-1}+\ldots+\mathbf{P}_{NN,k}^{-1}\right)^{-1}\left[\mathbf{P}_{11,k}^{-1}\left(\mathbf{x}_{c,k}-\hat{\mathbf{x}}_{1,k}\right)+\ldots+\mathbf{P}_{NN,k}^{-1}\left(\mathbf{x}_{c,k}-\hat{\mathbf{x}}_{N,k}\right)\right]\\&=\left(\mathbf{P}_{11,k}^{-1}+\ldots+\mathbf{P}_{NN,k}^{-1}\right)^{-1}\begin{bmatrix}\mathbf{P}_{11,k}^{-1} & \ldots & \mathbf{P}_{NN,k}^{-1}\end{bmatrix}\left(\mathbf{x}_{k}-\hat{\mathbf{x}}_{k}\right)\end{aligned}$$

So that the associated covariance for the global state estimate, denoted as $\mathbf{P}_{c,k}^{\mathbf{M}}$, can be calculated by

$$\begin{aligned}\mathbf{P}_{c,k}^{\mathbf{M}}&\triangleq E\left\{\left(\mathbf{x}_{c,k}-\hat{\mathbf{x}}_{c,k}^{\mathbf{M}}\right)\left(\mathbf{x}_{c,k}-\hat{\mathbf{x}}_{c,k}^{\mathbf{M}}\right)^{T}\right\}\\&=\left(\mathbf{P}_{11,k}^{-1}+\ldots+\mathbf{P}_{NN,k}^{-1}\right)^{-1}\begin{bmatrix}\mathbf{P}_{11,k}^{-1} & \ldots & \mathbf{P}_{NN,k}^{-1}\end{bmatrix}\mathbf{P}_{k}\\&\qquad\begin{bmatrix}\mathbf{P}_{11,k}^{-1} & \ldots & \mathbf{P}_{NN,k}^{-1}\end{bmatrix}^{T}\left(\mathbf{P}_{11,k}^{-1}+\ldots+\mathbf{P}_{NN,k}^{-1}\right)^{-1}\\&=\left(\mathbf{P}_{11,k}^{-1}+\ldots+\mathbf{P}_{NN,k}^{-1}\right)^{-1}\end{aligned} \tag{7.5}$$

The final form of equations (7.4) and (7.5) can be simplified to [23]

$$\hat{\mathbf{x}}_{c,k}^{\mathbf{M}}=\mathbf{P}_{c,k}^{\mathbf{M}}\left(\mathbf{P}_{11,k}^{-1}\hat{\mathbf{x}}_{1,k}+\ldots+\mathbf{P}_{NN,k}^{-1}\hat{\mathbf{x}}_{N,k}\right) \tag{7.6a}$$

$$\mathbf{P}_{c,k}^{\mathbf{M}} = \left(\mathbf{P}_{11,k}^{-1} + \ldots + \mathbf{P}_{NN,k}^{-1}\right)^{-1} \tag{7.6b}$$

and provide the simplest form for a global fusion of the local estimates that is in essence an optimal weighted least squares estimate with the specific weight as chosen in (7.6b).

7.4 Implementing Sensor Fusion Through the Federated Extended Kalman Filter

The GPS and vision-based navigation sensors were chosen as the local sensor components in the FEKF described above and the global estimated state vector, $\hat{\mathbf{x}}_{c,k}^{\mathbf{M}}$, was chosen to be the inertial position and velocity of the Pursuer satellite

$$\hat{\mathbf{x}}_k^{\mathbf{M}} = \begin{bmatrix} {}^{N}\mathbf{R}_P \\ {}^{N}\dot{\mathbf{R}}_P \end{bmatrix} = \begin{bmatrix} {}^{N}X & {}^{N}Y & {}^{N}Z & {}^{N}\dot{X} & {}^{N}\dot{Y} & {}^{N}\dot{Z} \end{bmatrix}^T$$

GPS position and velocity measurements are in inertial frame components but the vision-based navigation sensor measures the relative separation and velocity between the Target and Pursuer. To utilize the FEKF as described above, the estimated state and covariance from the vision sensor must be transformed into inertial components.

The vision-based navigation state estimate can be represented as

$${}^{O}\hat{\mathbf{x}}_{vision} = \begin{bmatrix} {}^{O}\mathbf{r}^T & {}^{O}\dot{\mathbf{r}}^T \end{bmatrix}^T$$

where ${}^{O}\mathbf{r}$ is the relative separation and ${}^{O}\dot{\mathbf{r}}$ is the relative velocity in Hills frame components. ${}^{O}\hat{\mathbf{x}}_{vision}$ can be rotated into the inertial frame and in turn be used

in the global estimate through the use of the transport theorem which yields the following transformation

$$ {}^{N}\hat{\mathbf{x}}_{vision} = \begin{bmatrix} {}^{N}\mathbf{r} \\ {}^{N}\dot{\mathbf{r}} \end{bmatrix} = \begin{bmatrix} {}^{N}\mathbf{R}_T + [NO]\,{}^{O}\mathbf{r} \\ {}^{N}\dot{\mathbf{R}}_T + [NO]\,{}^{O}\dot{\mathbf{r}} + {}^{O}\boldsymbol{\omega}_{O/N} \times {}^{O}\mathbf{r} \end{bmatrix} \tag{7.7} $$

where ${}^{N}\mathbf{R}_T$ and ${}^{N}\dot{\mathbf{R}}_T$ are the Target's inertial position and velocity, $\boldsymbol{\omega}_{O/N}$ is the rotation rate of the O-frame with respect to the inertial frame, and $[NO]$ is the rotation matrix from the O-frame to the N-frame.

To transform the covariance terms of the vision sensor's estimates into the inertial frame a similar procedure is performed. The general covariance used in the local vision sensor system can be expressed as

$$ {}^{O}\mathbf{P}_{vision} = \begin{bmatrix} {}^{O}\mathbf{P}_{11} & {}^{O}\mathbf{P}_{12} \\ {}^{O}\mathbf{P}_{21} & {}^{O}\mathbf{P}_{22} \end{bmatrix} \tag{7.8} $$

where ${}^{O}\mathbf{P}_{11}, {}^{O}\mathbf{P}_{12}, {}^{O}\mathbf{P}_{21}, {}^{O}\mathbf{P}_{22}$ constitute the four quadrants of ${}^{O}\mathbf{P}_{vision}$ and are each 3×3 in size. The transformed covariance to be used in the global estimate can be represented by

$$ {}^{N}\mathbf{P}_{vision} = \begin{bmatrix} {}^{N}\mathbf{P}_{11} & {}^{N}\mathbf{P}_{12} \\ {}^{N}\mathbf{P}_{21} & {}^{N}\mathbf{P}_{22} \end{bmatrix} \tag{7.9} $$

where the terms ${}^{N}\mathbf{P_{11}}, {}^{\mathbf{N}}\mathbf{P_{12}}, {}^{\mathbf{N}}\mathbf{P_{21}}$ and ${}^{N}\mathbf{P_{22}}$ are derived in Appendix C. The derivations yield

$$ {}^{N}\mathbf{P}_{11} = [NO]\,{}^{O}\mathbf{P}_{11}\,[ON] \tag{7.10a} $$

$$ {}^{N}\mathbf{P}_{12} = [NO]\left({}^{O}\mathbf{P}_{12} - {}^{O}\mathbf{P}_{11}\left[{}^{O}\boldsymbol{\omega}_{O/N}\times\right]\right)[ON] \tag{7.10b} $$

$$ {}^{N}\mathbf{P}_{21} = [NO]\left({}^{O}\mathbf{P}_{21} + \left[{}^{O}\boldsymbol{\omega}_{O/N}\times\right]{}^{O}\mathbf{P}_{11}\right)[ON] \tag{7.10c} $$

$$
\begin{aligned}
{}^{N}\mathbf{P}_{22} = [NO]\left({}^{O}\mathbf{P}_{22} - {}^{O}\mathbf{P}_{21}\left[{}^{O}\boldsymbol{\omega}_{O/N}\times\right] + \left[{}^{O}\boldsymbol{\omega}_{O/N}\times\right]{}^{O}\mathbf{P}_{12} + \right. \\
\left.\left[{}^{O}\boldsymbol{\omega}_{O/N}\times\right]{}^{O}\mathbf{P}_{11}\left[{}^{O}\boldsymbol{\omega}_{O/N}\times\right]\right)[ON]
\end{aligned}
\tag{7.10d}
$$

Once the vision sensor's transformed state vector, ${}^{N}\hat{\mathbf{x}}_{vision}$, and covariance, ${}^{N}\mathbf{P}_{vision}$, have been formed they can be implemented in (7.6) with the GPS sensor's state vector and covariance. The final form of the sensor fusion equations used in this thesis at the k^{th} iteration are

$$
\hat{\mathbf{x}}_k^{\mathbf{M}} = \mathbf{P}_k^{\mathbf{M}}\left(\mathbf{P}_{GPS,k}^{-1}\hat{\mathbf{x}}_{GPS,k} + {}^{N}\mathbf{P}_{vision,k}^{-1}{}^{N}\hat{\mathbf{x}}_{vision,k}\right) \tag{7.11a}
$$

$$
\mathbf{P}_k^{\mathbf{M}} = \left(\mathbf{P}_{GPS,k}^{-1} + {}^{N}\mathbf{P}_{vision,k}^{-1}\right)^{-1} \tag{7.11b}
$$

7.5 Resetting the Local Estimates & Error Covariances

In the federated Kalman filter algorithm, the master filter computes an optimal weighted least-squares estimate of the global system state and its error covariance according to the methods described in the preceding sections. Then, as illustrated in Figure 7.3, this information can be fed back to the local filters to reset the local estimates and local error covariances. The local state estimates and local error covariances are reset with values that have the effect of resetting the global estimate and the global error covariance computed in the first stage of processing, $\hat{\mathbf{x}}_k$ and $\mathbf{P}_k$, to the corresponding values computed by the master fusion filter.

Each local processor can be reset by the global filter. Since the GPS state and covariance are in the same reference frame as the global state and covariance the GPS state vector reset can be implemented directly by

$$
\begin{aligned}
\hat{\mathbf{x}}_{GPS,k+1}^{-} &= \hat{\mathbf{x}}_k^{\mathbf{M}} \\
\mathbf{P}_{GPS,k+1}^{-} &= \mathbf{P}_k^{\mathbf{M}}
\end{aligned}
\tag{7.12}
$$

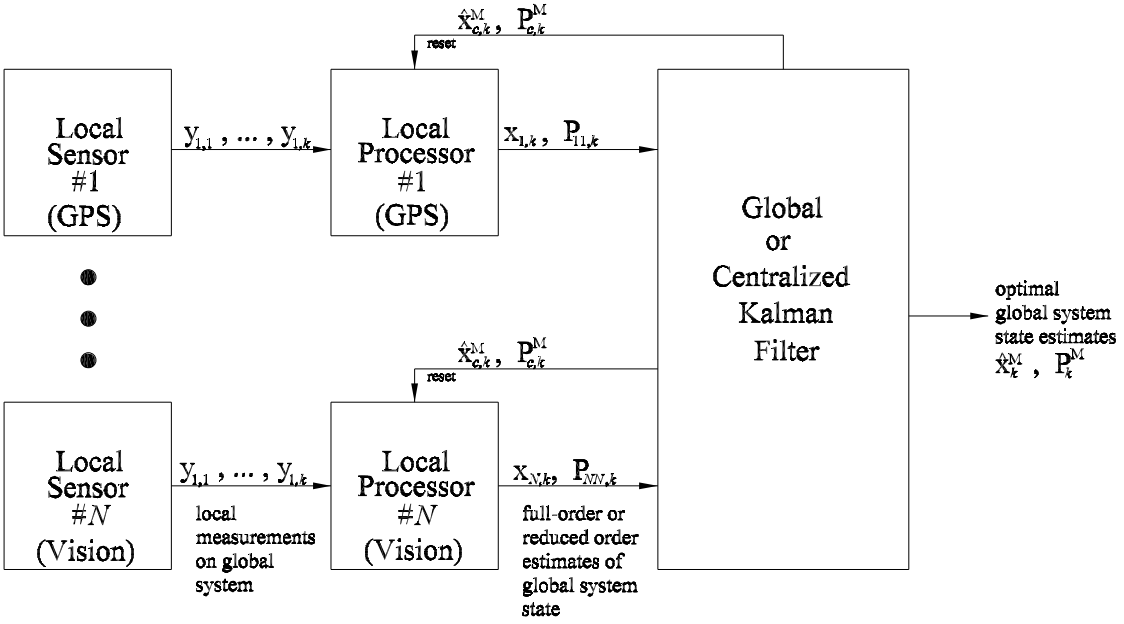

Figure 7.3 Decentralized Kalman Filter Architecture with feedback.

However, to reset the vision state vector the global state must be transformed from inertial components to orbit frame components. The transformation can be given by

$$ {}^{O}\hat{\mathbf{x}}_{vision} = \begin{bmatrix} {}^{O}\hat{\mathbf{r}} \\ {}^{O}\dot{\hat{\mathbf{r}}} \end{bmatrix} = \begin{bmatrix} [ON]\left({}^{N}\hat{\mathbf{R}}_P - {}^{N}\mathbf{R}_T\right) \\ [ON]\left({}^{N}\dot{\hat{\mathbf{R}}}_P - {}^{N}\dot{\mathbf{R}}_T\right) - \boldsymbol{\omega}_{O/N} \times \left({}^{N}\hat{\mathbf{R}}_P - {}^{N}\mathbf{R}_T\right) \end{bmatrix} \tag{7.13} $$

A transformation similar to (7.10) is performed to make $\mathbf{P^M}$ available for resetting the vision's local estimator. The final result is

$$ {}^{O}\mathbf{P}_{vision} = \begin{bmatrix} \mathbf{P}_{reset11} & \mathbf{P}_{reset12} \\ \mathbf{P}_{reset21} & \mathbf{P}_{reset2} \end{bmatrix} \tag{7.14} $$

where

$$
\begin{aligned}
\mathbf{P}_{reset11} &= [ON]\,\mathbf{P}_{11}^{\mathbf{M}}\,[NO] \\
\mathbf{P}_{reset12} &= [ON]\,\mathbf{P}_{12}^{\mathbf{M}}\,[NO] + [ON]\,\mathbf{P}_{11}^{\mathbf{M}}\,[NO]\left[{}^{O}\boldsymbol{\omega}_{O/N}\right] \\
\mathbf{P}_{reset21} &= [ON]\left[\mathbf{P}_{12}^{\mathbf{M}}\right]^{T}[NO] - \left[{}^{O}\boldsymbol{\omega}_{O/N}\times\right][ON]\left[\mathbf{P}_{11}^{\mathbf{M}}\right]^{T}[NO] \\
\mathbf{P}_{reset22} &= [ON]\left(\mathbf{P}_{22}^{\mathbf{M}} + \mathbf{P}_{21}^{\mathbf{M}}\left[{}^{N}\boldsymbol{\omega}_{O/N}\times\right] - \left[{}^{N}\boldsymbol{\omega}_{O/N}\times\right]\mathbf{P}_{12}^{\mathbf{M}}\right. \\
&\qquad \left. - \left[{}^{N}\boldsymbol{\omega}_{O/N}\times\right]\mathbf{P}_{11}^{\mathbf{M}}\left[{}^{N}\boldsymbol{\omega}_{O/N}\times\right]\right)[NO]
\end{aligned}
$$

The preceding chapters have given the governing system dynamics and developed the estimation models used for the simulations in this thesis. The next chapter will outline the simulations performed, give the parameters used for those simulations and discuss the results.

CHAPTER 8

SIMULATIONS & RESULTS

8.1 Simulation Descriptions

The results of the GPS/vision fusion based estimate simulations are discussed in this chapter. For this study two simulations employing sensor fusion were carried out: the first keeps local estimators independent of the Master filter and the second implements reinitialization of each sensor's common local state vector and covariance by the Master filter after each update. The simulations were carried out using MATLAB.

For a more accurate determination of the effects of state and covariance reinitialization the simulation parameters for both simulations were the same. The initial conditions for the simulations are shown in Table 8.1, the sensor parameters are listed in 8.2, and the control law parameters are given in 8.3.

The rendezvous scenario was simulated for an arbitrary time of 100 seconds to show that the specified control laws and estimation algorithms worked as desired. GPS pseudorange, vision-based, and attitude measurements were all taken at a rate of $25Hz$. The local state estimates (GPS, vision, attitude) and the Master state estimate were also updated at a rate of $25Hz$. Control inputs were updated at a rate of $5Hz$, held constant between updates, and saturation limits were imposed to limit the amount of translational and attitude control available (for a more realistic simulation).

Initially only the GPS and attitude sensors are actively providing measurements. Because the vision sensor is not initially active, Master filter estimates are

based only on GPS data until the vision sensor is turned on. When the Master state estimate relative separation magnitude is less than $100m$ the vision sensor is switched on and sensor fusion in the form of the FEKF is implemented (i.e. the Master estimate now depends on GPS and vision measurements).

Translational controller calculations are based on the Master state estimate and rotational control calculations are based on the attitude sensor's estimate. It should be noted that the translational controller was highly damped to avoid problems with the vision sensor activation as the Pursuer crossed the vision sensor activation distance.

Once the Pursuer is estimated to be less than $100m$ from the Target the GPS standard deviation and covariance were artificially increased to roughly simulate the effects of signal blockage and multipath errors. The standard deviation is linearly increased by $1m$ for every meter of separation under $100m$ (i.e. the standard deviation increase is $0m$ at a separation of $100m$ and is 100 at a separation of $0m$.

The Pursuer began the simulations trailing the Target by $200m$ in the $\hat{o}_\theta$ direction with no relative velocity and an arbitrary orientation. The Target is in a free-floating orbit and aligned with and rotating at the same rate as the O-frame. The desired relative separation vector for the Pursuer to reach was $5m$ along the $-\hat{t}_2$ axis.

Docking ports for the Target and Pursuer were assumed to be along the $-\hat{t}_2$ and $\hat{p}_2$ axes respectively and the desired Pursuer orientation was to align its docking port with the Target's docking port. Both satellites were assumed to be cubes with side length $2m$ and evenly distributed mass. Four light beacons for the vision-based sensor were located at the Target's four corners on the $\left(\hat{t}_1, \hat{t}_3\right)$ plane and facing the $-\hat{t}_2$ direction.

Table 8.1 Satellite Initial Conditions for Both Simulations

Description	**Value**
Target Initial Orbital Elements: ${}^{N}\mathbf{R}_{T_0}$	$a = 6737km$ $e = 5.1181 \times 10^{-4}$ $i = 51.66°$ $\Omega = 209.05°$ $\omega = 282.18°$ $\nu = 281.81°$
Pursuer Initial Position: $\mathbf{R}_{P_0}$	$\mathbf{R}_{T_0} - [200m]\,\hat{o}_\theta$
Target & Pursuer Coefficient of Drag	$c_D = 2.2$
Target & Pursuer Exposed Area	$A = 24m^2$
Target & Pursuer Mass	$mass = 500kg$
Target & Pursuer Principal Moment of Inertia	$[I] = \begin{bmatrix} 333.33 & 0 & 0 \\ 0 & 333.33 & 0 \\ 0 & 0 & 333.33 \end{bmatrix} kgm^2$
Target Initial Attitude (Aligned with the O-frame)	$\boldsymbol{\sigma}_{T_0} = \begin{bmatrix} -.241084 \\ -.010657 \\ .222592 \end{bmatrix}$
Pursuer Initial Attitude	$\boldsymbol{\sigma}_{P_0} = -\boldsymbol{\sigma}_{T_0}$
Target Initial Angular Velocity	$\boldsymbol{\omega}_{T_0/N} = \boldsymbol{\omega}_{O/N} = \left[\frac{\mathbf{R}_{T_0} \times \dot{\mathbf{R}}_{T_0}}{R_{T_0}^2}\right] \frac{rad}{s}$
Pursuer Initial Angular Velocity	$\boldsymbol{\omega}_{P_0/N} = 2\boldsymbol{\omega}_{T_0} \frac{rad}{s}$

8.2 Simulation Results: No Local Reinitialization by the Master Estimate

This simulation carried out the above described rendezvous engagement scenario without reinitialization by the Master estimator (i.e. the GPS and vision estimators

Table 8.2 Sensor Estimation, & Control Parameters for Both Simulations

Description	**Value**
GPS Standard Deviation	$\sigma_{GPS} = 10m$
GPS Clock Bias	$\tau = 50km$
GPS G Matrix	$G_{GPS} = \begin{bmatrix} 0_{3\times3} & 0_{3\times1} \\ I_{3\times3} & 0_{3\times1} \\ 0_{3\times3} & \begin{bmatrix} 1 & 0 & 0 \end{bmatrix}^T \end{bmatrix}$
GPS Q Matrix	$Q_{GPS} = \begin{bmatrix} 10^{-5} \times I_{3\times3} & 0_{3\times1} \\ 0_{1\times3} & .2 \end{bmatrix}$
Beacon Positions (T-frame)	$\begin{bmatrix} X_1 & Y_1 & Z_1 \\ X_2 & Y_2 & Z_2 \\ X_3 & Y_3 & Z_3 \\ X_4 & Y_4 & Z_4 \end{bmatrix} = \begin{bmatrix} -1 & 1 & 1 \\ -1 & 1 & -1 \\ 1 & 1 & -1 \\ 1 & 1 & 1 \end{bmatrix} m$
Camera Position (P-frame)	$\begin{bmatrix} X_c & Y_c & Z_c \end{bmatrix}^T = \begin{bmatrix} 0 & 1 & 0 \end{bmatrix}^T m$
Vision Standard Deviation	$\sigma_{vision} = 5cm$
Vision G Matrix	$G_{vision} = \begin{bmatrix} 0_{3\times3} & 0_{3\times3} \\ 0_{3\times3} & I_{3\times3} \end{bmatrix}$
Vision Q Matrix	$Q_{vision} = 10^{-5} I_{6\times6}$
Attitude Standard Deviation	$\sigma_{MRP} = 1 \times 10^{-4} cm$

remained local as depicted in Figure 7.2). The resulting plots from this simulation are given below.

Figure 8.1 shows the relative separation between the Target and Pursuer in the O-frame. It is seen that Pursuer follows the desired trajectory fairly well and the estimated position is generally no more than a few meters from the true position

Table 8.3 Control Law Parameters for Both Simulations

Description	**Value**
Translational Gains	$k_{P_{Trans}} = I_{3\times3}$ $k_{D_{Trans}} = 8I_{3\times3}$
Rotational Gains	$k_{P_{Rot}} = 300I_{3\times3}$ $k_{D_{Rot}} = 400I_{3\times3}$
Translational Saturation (each axis)	$u_{Trans_{max}} = \pm 1 \frac{m}{s^2}$
Torque Saturation (each axis)	$u_{Rot_{max}} = \pm 10 Nm$
Desired Separation Vector	$\mathbf{r}_{Des} = \begin{bmatrix} 0\hat{t}_1 & -5\hat{t}_2 & 0\hat{t}_3 \end{bmatrix}^T m$
Desired Orientation	$\boldsymbol{\sigma}_{Des} = \boldsymbol{\sigma}_T$

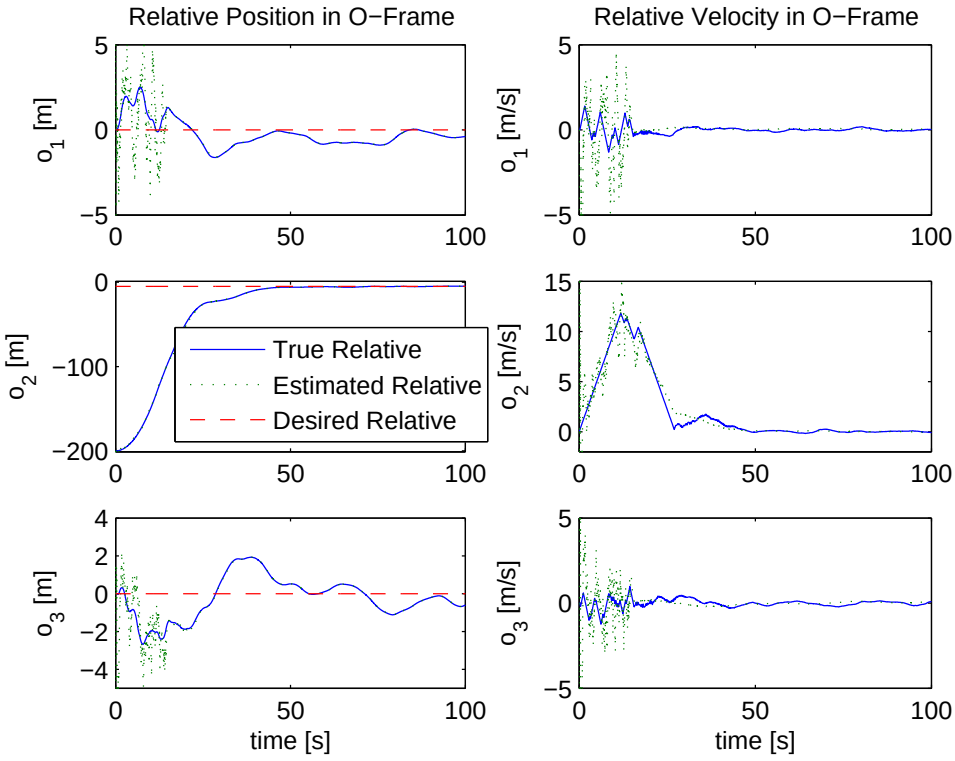

Figure 8.1 Relative Position and Velocity for Simulation 1.

indicating that the control and estimation algorithms work as intended. The true trajectory does not follow the desired trajectory perfectly because of multiple factors: the control is held constant between updates, the control calculations are based on estimated data which is errant in nature, and the selected control was not optimized.

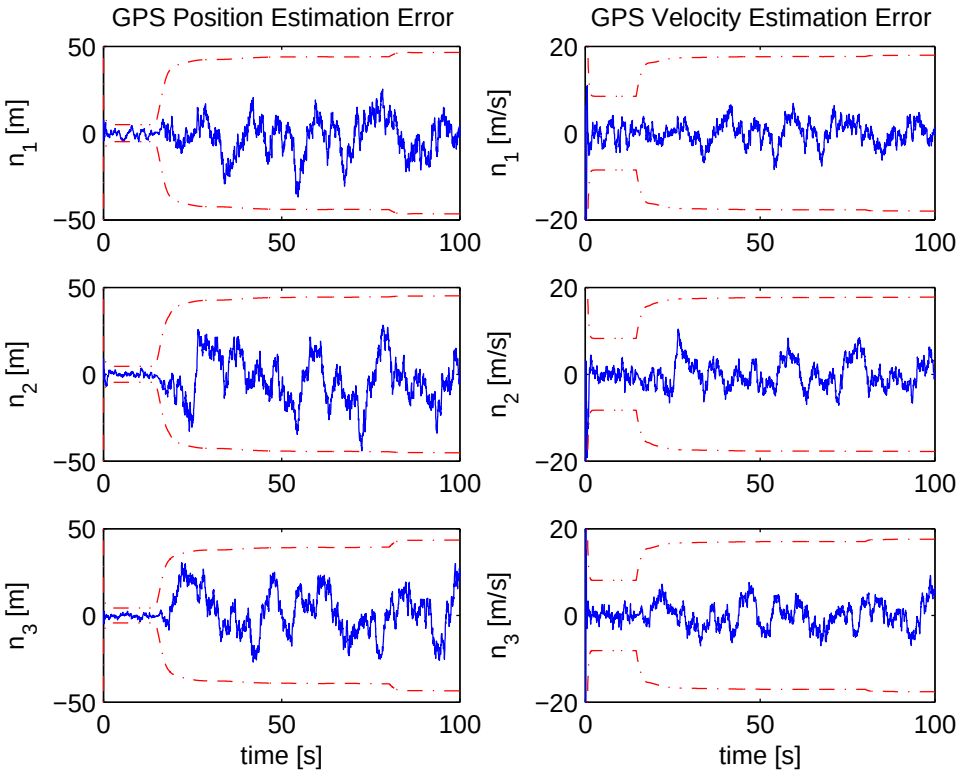

Figure 8.2 GPS Position and Velocity Estimation Error for Simulation 1.

The position and velocity estimation errors of the GPS sensor system are shown in Figure 8.2. It can be seen that the GPS system works well and generally has errors under $5m$ along each inertial axis when the satellite's separation magnitude is large enough to ignore blockage and multipath errors. However, as the relative separation decreases the GPS estimation errors increase substantially and are probably large enough to disallow a safe rendezvous engagement when GPS navigation alone is used.

The dashed lines indicate the 3σ[1] bounds of the GPS estimates and the GPS estimates lie within the bounds in this case indicating confidence in the estimation algorithm.

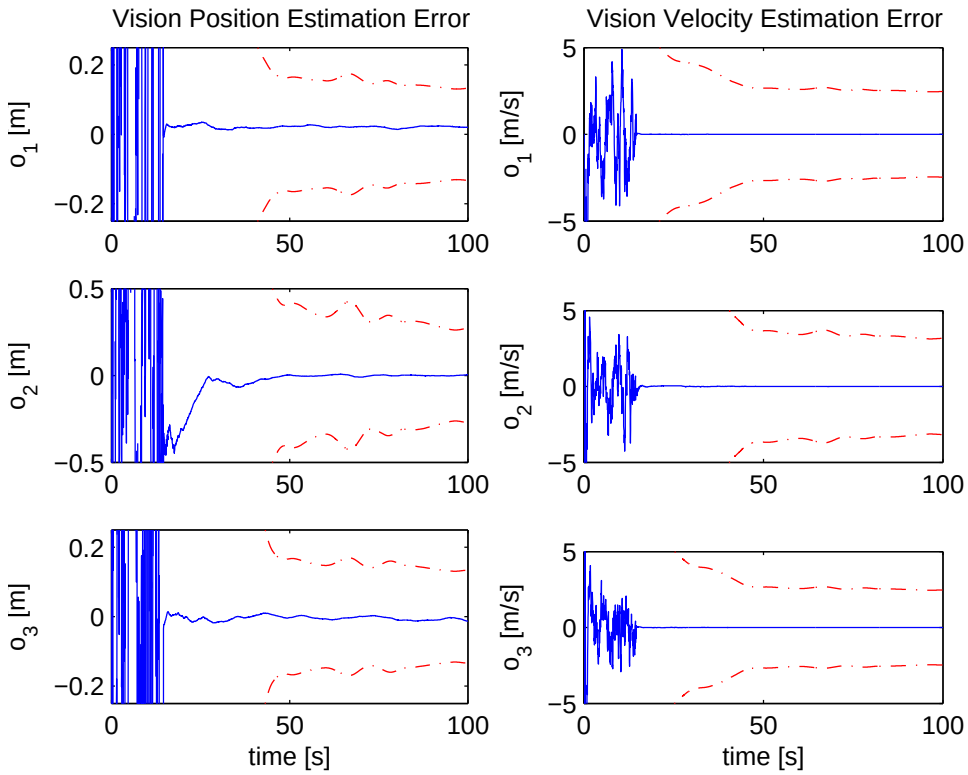

Figure 8.3 Vision Position and Velocity Estimation Error for Simulation 1.

Position and velocity estimation errors from the vision-based sensor system are shown in Figure 8.3. Approximately the first 20 seconds of the vision-based estimates is GPS data fed to the vision sensor primarily for plotting purposes. Once the Pursuer comes within $100m$ of the Target the vision sensor is switched on and it can be seen that the position and velocity estimation errors are very small, generally on the order of millimeters with slightly more error in the velocity estimate than the position estimate. The low estimation error indicates that the vision navigation

[1]If Data is from a normal distribution then 1 standard deviation (1σ) covers 68% of the population, 2σ covers 95%, and 3σ 99.7% of the population.

system may be a viable option to assist proximity navigation when GPS signals may be too erroneous for valid navigation.

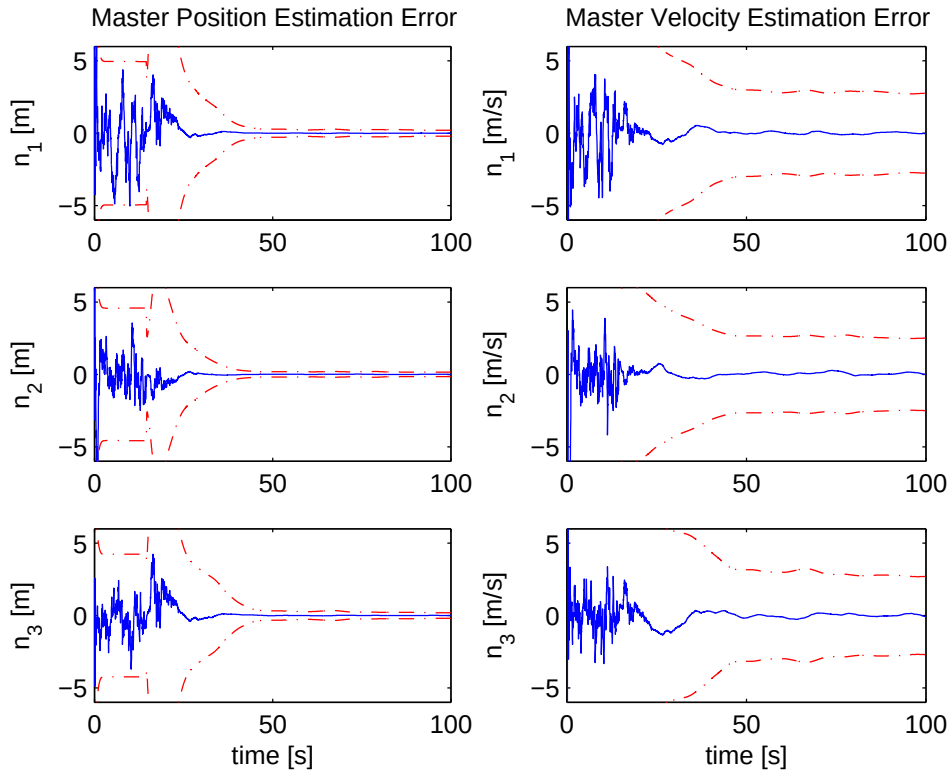

Figure 8.4 Master Filter Position and Velocity Estimation Error for Simulation 1.

Figure 8.4 shows the position and velocity estimation error calculated by the fused state estimates. The initial errors are all due to GPS because the vision sensor had yet to be switched on. The transition to sensor fusion is clearly seen by the jump in estimation error and 3σ bounds at about 20 seconds. This occurs because the vision estimates had not converged while the GPS estimates had converged by that point. The optimal weighting performed by the fusion algorithm is easily seen as well. From Figures 8.2 and 8.3 it is seen that the vision estimation has a better performance than the GPS sensor (less estimation error and smaller corresponding

covariance). The vision's smaller covariance weights the vision estimates more than the corresponding GPS in the fusion algorithm. As a result the Master estimate performs similarly to the vision sensor system once the vision system has settled.

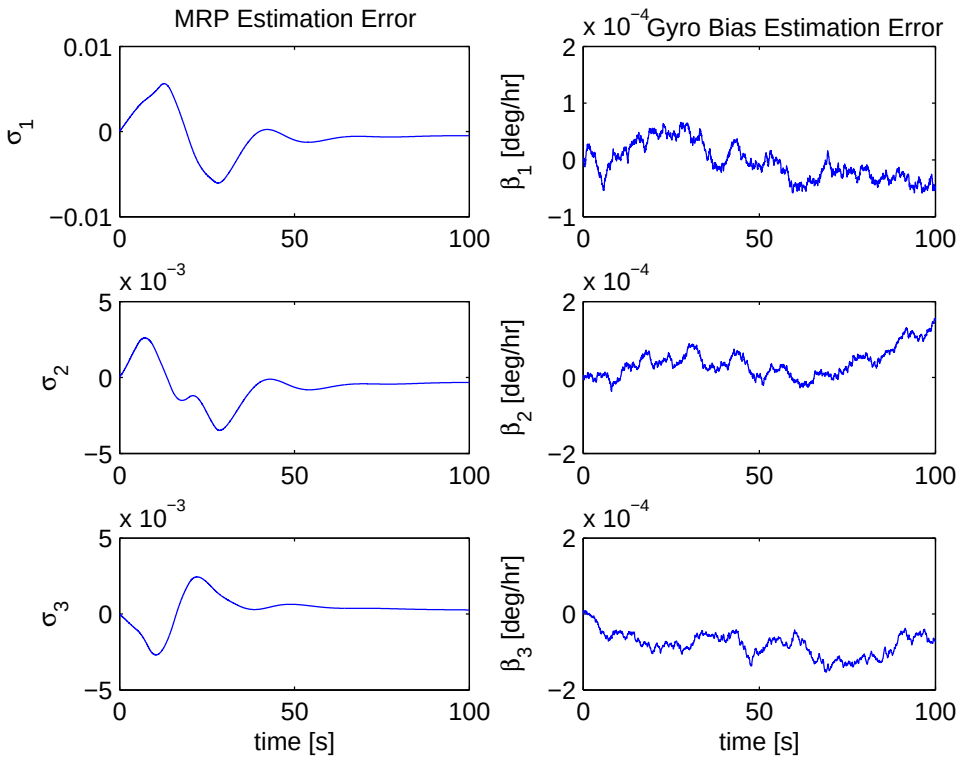

Figure 8.5 Attitude Estimation Error and Gyro Bias Estimation Error for Simulation 1.

The attitude and gyro bias estimator performed adequately with errors generally less than 1×10^{-3} for the MRP once the filter had converged giving desired attitude estimation results.

The right side plots of Figure 8.6 show the desired orientation for the Pursuer to reach and its true and estimated orientation during the simulation. The convergence of the true and desired orientations indicates that the rotational control laws are effective in achieving synchronization. The left hand side of the figure shows the

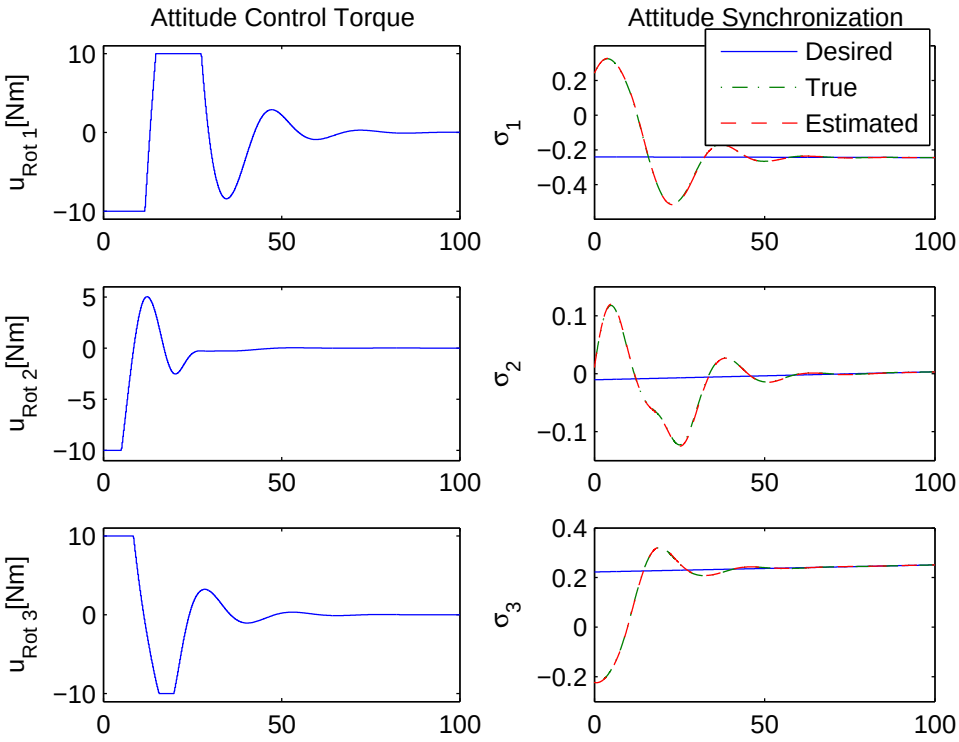

Figure 8.6 Attitude Synchronization and Control Torque Input for Simulation 1.

corresponding control torques applied to the Pursuer to reach the desired attitude. Torque saturation limits were imposed during roughly the first third of the simulation as indicated by the constant magnitude sections, especially along the $\hat{n}_1$ and $\hat{n}_3$ axes. As the estimated attitude approaches the desired attitude the control torque used decreases to near zero, however, the necessary torque never be completely zero due to the constant rotation of the Target and subsequent constant necessary motion synchronization.

The translational control accelerations used by the Pursuer to reach the desired position vector $\mathbf{r}_{des}$ are shown in Figure 8.7. The constant areas are where the control saturations were imposed. The necessary control was calculated in the O-frame and

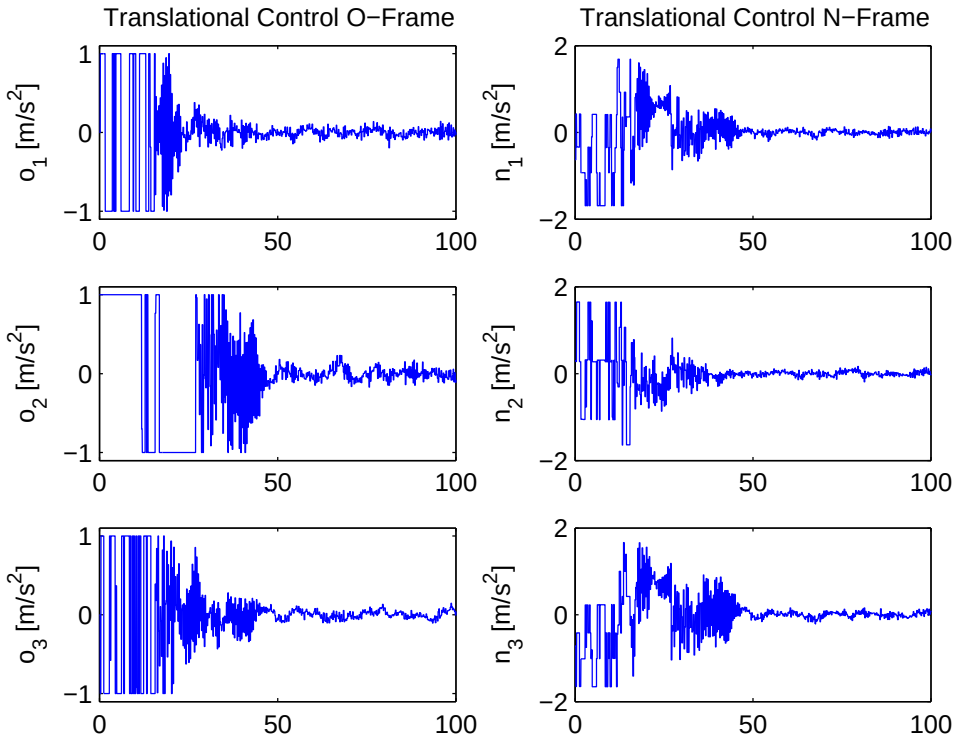

Figure 8.7 Translational Control Acceleration in the Inertial and Orbit Frames for Simulation 1.

then rotated into the inertial frame so that it could be applied to the inertial equations of motion.

It appears the GPS sensor system did a good job of estimating the clock bias, J_2, and ballistic coefficient terms because the estimation errors were very small in Figure 8.8. Note that it was assumed that these parameters were observable enough to be estimated by the GPS estimator. A full observability analysis was not performed to determine 'how observable' these parameters are.

8.3 Simulation Results: Local Reinitialization by the Master Estimate

When the local estimators are reinitialized by the Master estimate the resulting estimates improve and lead to a better performance by the translational controller

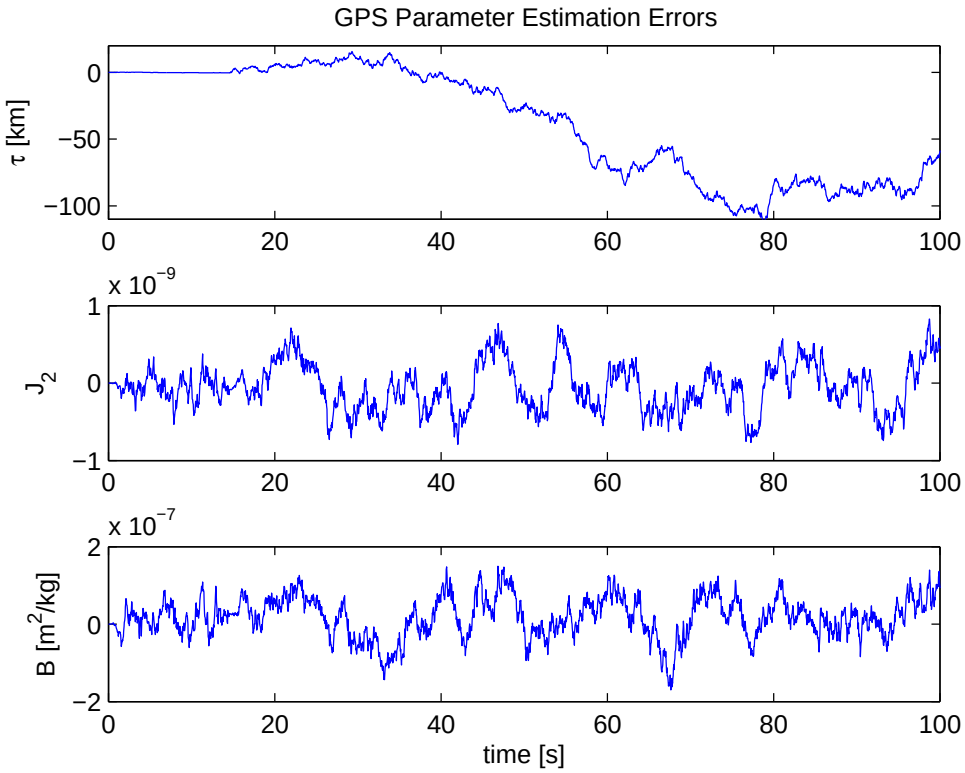

Figure 8.8 GPS Clock Bias, J_2, and Ballistic Coefficient Estimation Errors for Simulation 1.

as shown by Figure 8.9. The trajectory taken by the pursuer in this case is much smoother and follows the desired much more closely than in the first simulation. This is likely due to the improved estimates given by the Master filter shown in Figure 8.12. The resulting oscillatory motion is due to the fusion process trying to settle down once reinitialization has been implemented.

Reinitialization has a transition time that takes a significant amount of time to converge as shown by the semi-erratic decaying sinusoidal estimation errors in Figures 8.10, 8.11, 8.12. After the Master estimate has settled down the local estimates settle within the 3σ bounds and the estimation error becomes very small. Although the transition is erratic implementing reinitialization seems to improve the estimation process because of the smaller errors and improved trajectory tracking.

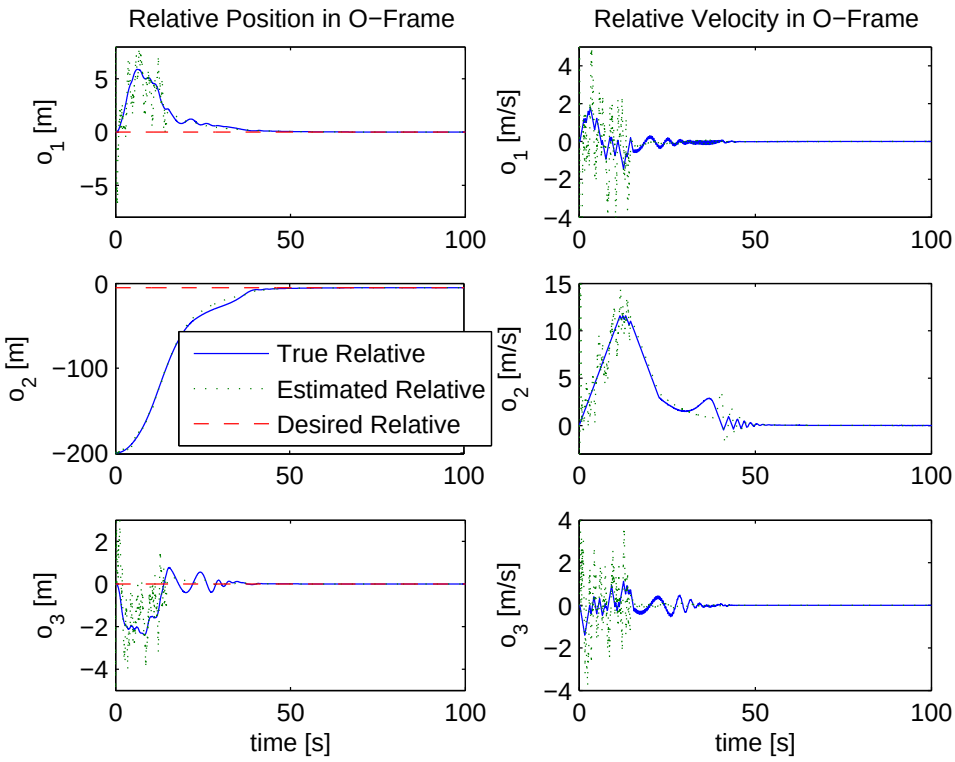

Figure 8.9 Relative Position and Velocity for Simulation 2.

Reinitialization did not affect attitude or gyro bias estimates and in turn did not affect the resulting control torques. Attitude estimation results should not differ significantly between the first and second simulations.

The second simulation uses much more control acceleration than the first simulation does. Figure 8.15 shown a significant increase in the control acceleration around the halfway point of the simulation. This is due to the increased estimation errors in the Master estimate. The Master estimate believes the Pursuer is farther away from the Target than it actually so the resulting control acceleration is larger to try and close the gap. However, the control acceleration does eventually settle down and tracks the desired position vector much better than in the first case.

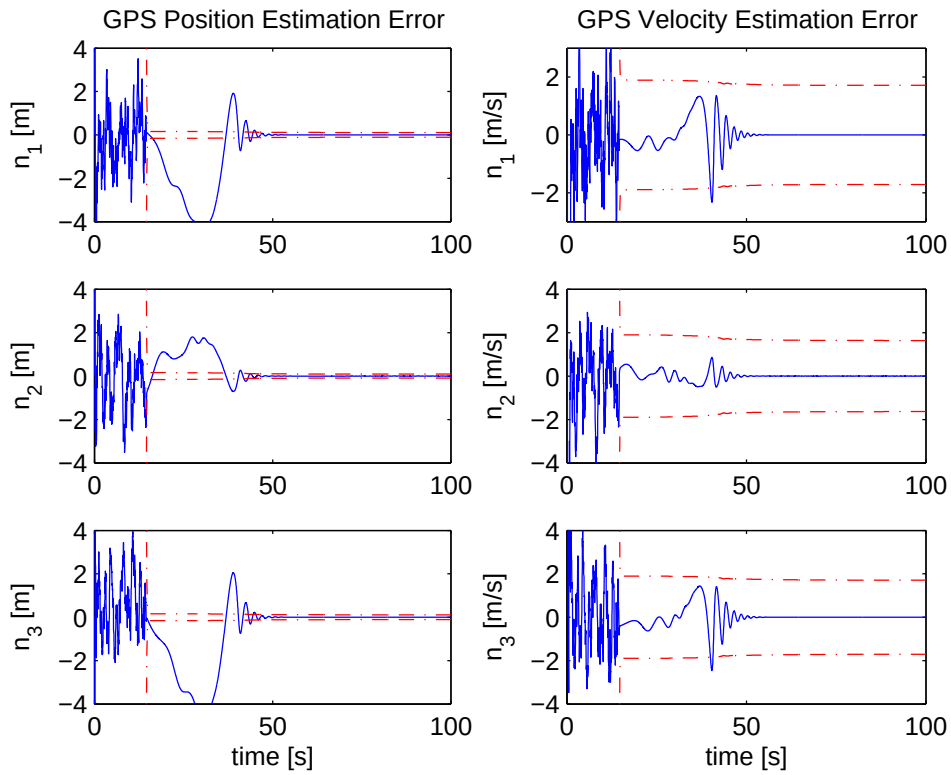

Figure 8.10 GPS Position and Velocity Estimation Error for Simulation 2.

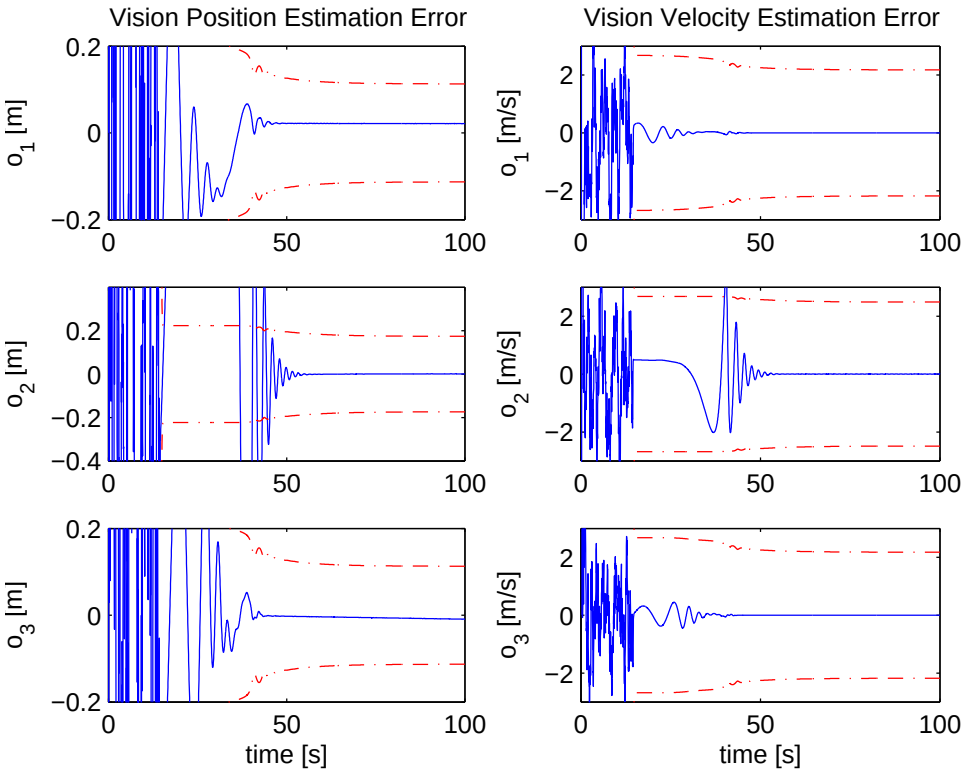

Figure 8.11 Vision Position and Velocity Estimation Error for Simulation 2.

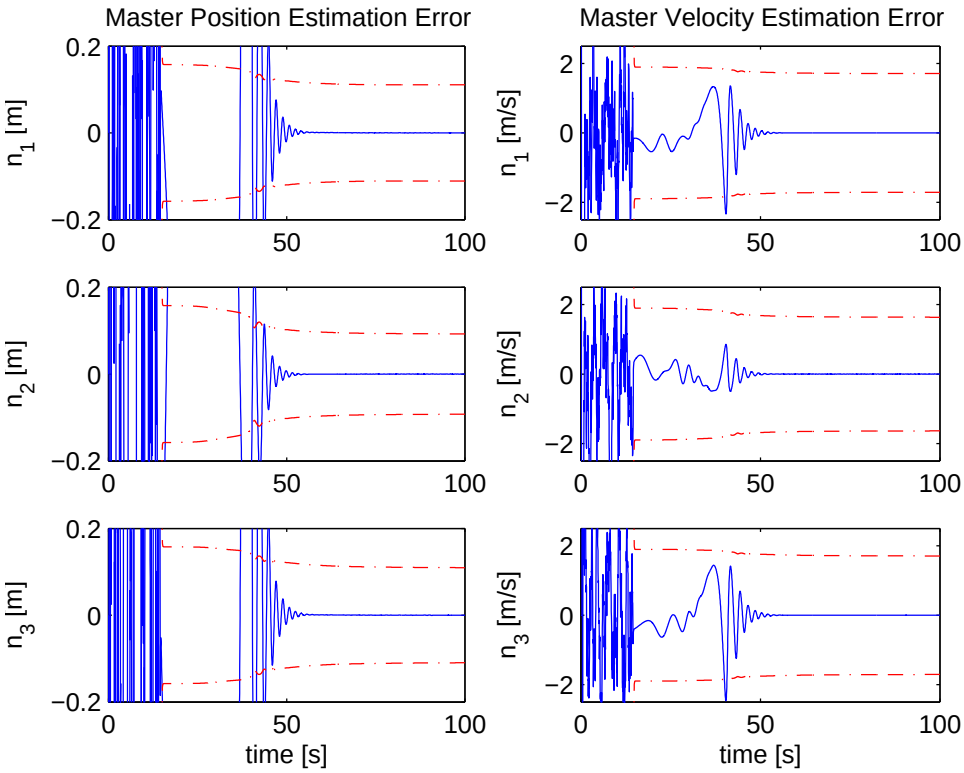

Figure 8.12 Master Filter Position and Velocity Estimation Error for Simulation 2.

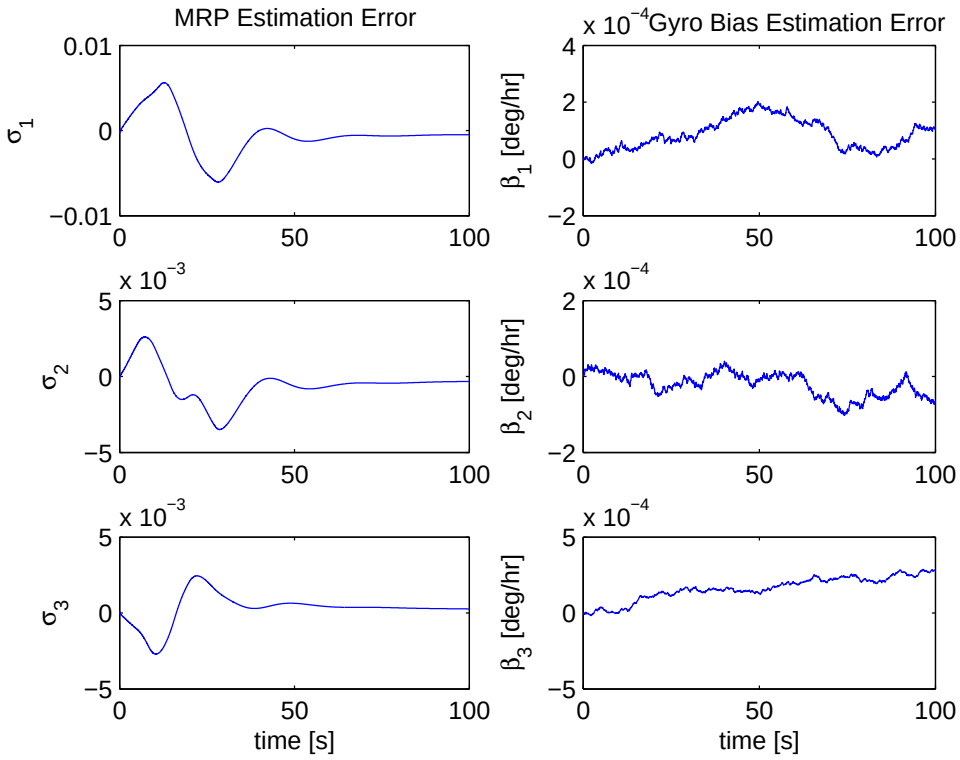

Figure 8.13 Attitude Estimation Error and Gyro Bias Estimation Error for Simulation 2.

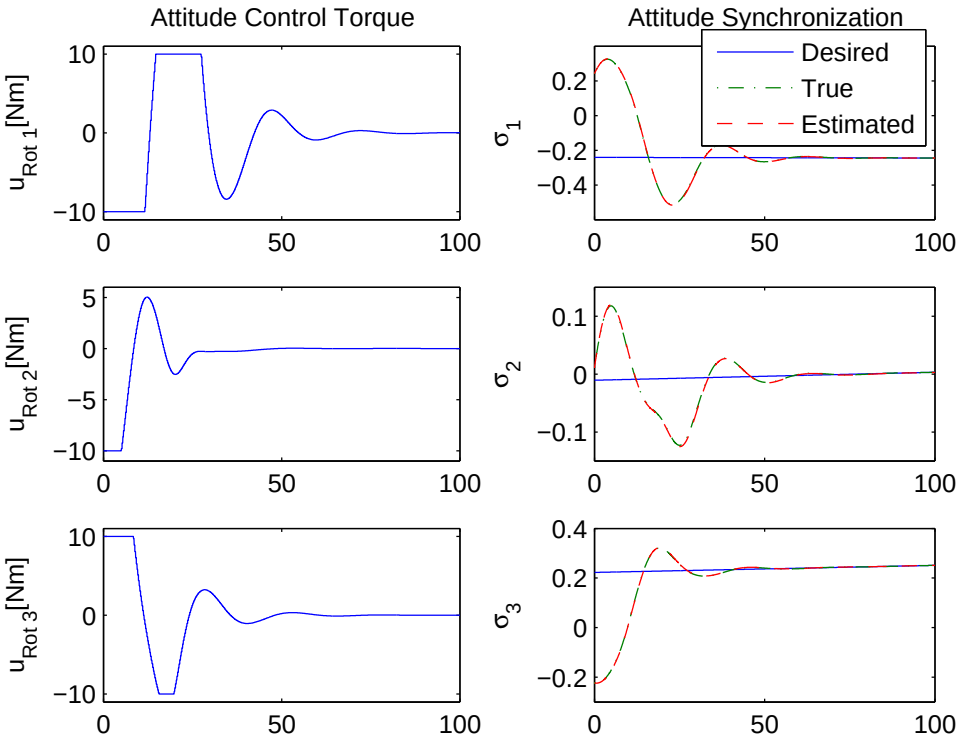

Figure 8.14 Attitude Synchronization and Control Torque Input for Simulation 2.

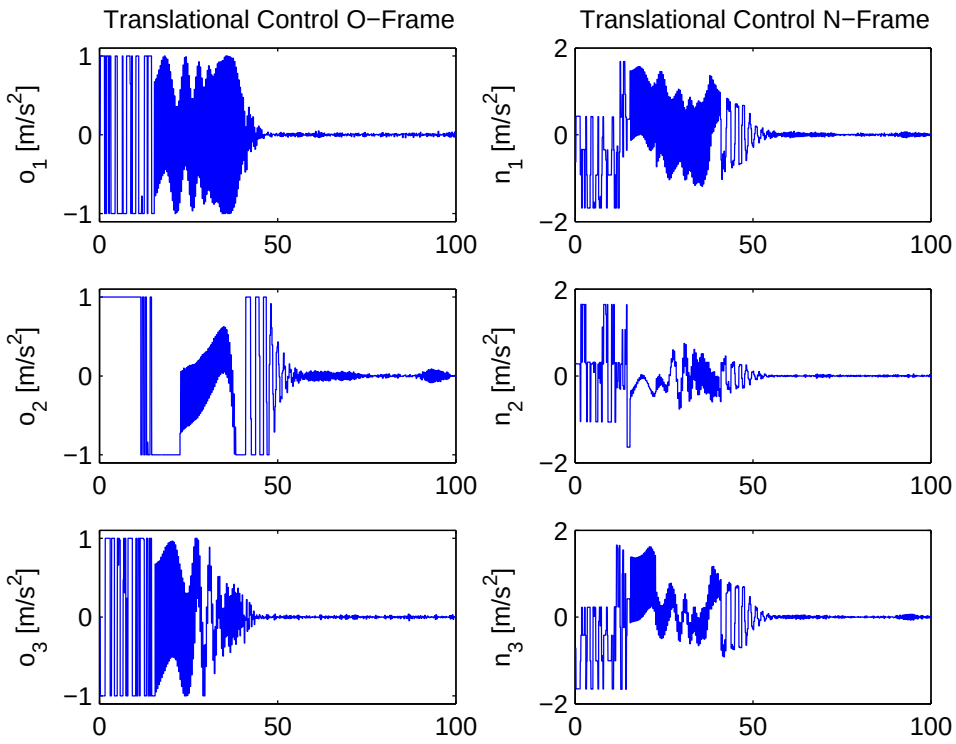

Figure 8.15 Translational Control Acceleration in the Inertial and Orbit Frames for Simulation 2.

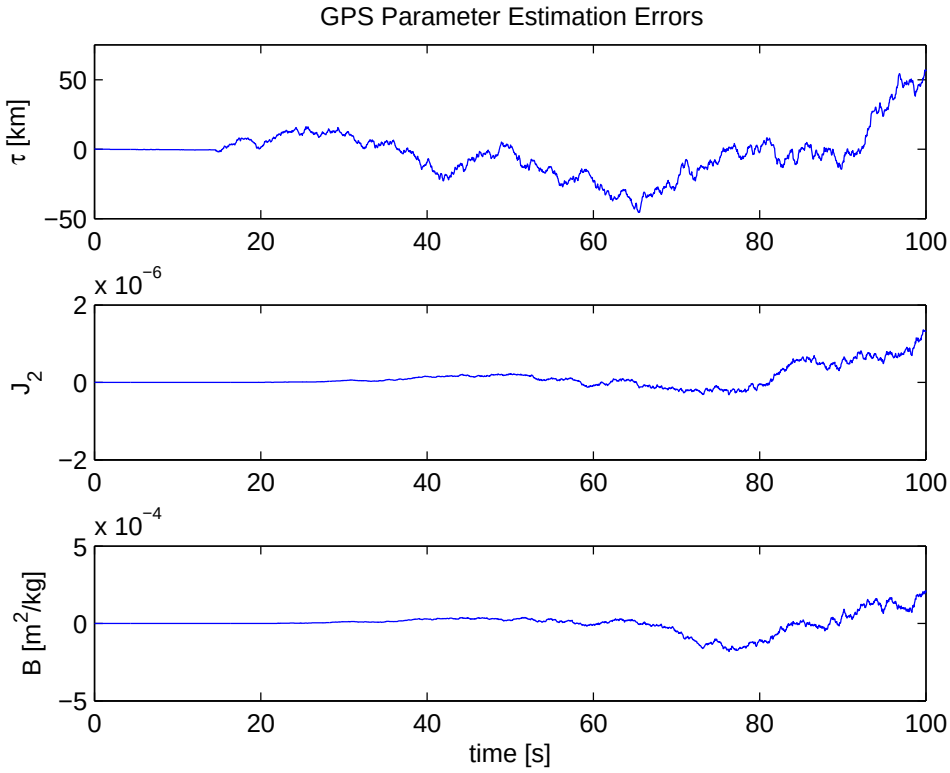

Figure 8.16 GPS Clock Bias, J_2, and Ballistic Coefficient Estimation Errors for Simulation 2.

CHAPTER 9

CONCLUSIONS

The research dealt with multi-sensor fusion for autonomous estimation and control and applied it to rendezvous and docking of spacecraft. A system consisting of a free-floating (i.e. uncontrollable) Target spacecraft and an active (controllable) Pursuer spacecraft was constructed and estimation and control algorithms were imposed on the system to achieve motion synchronization for rendezvous and docking.

GPS and vision-based sensor systems were modeled to provide inertial and relative position measurements respectively. Filters were developed for each of the sensor systems to provide estimates of the inertial and relative positions and velocities. Estimates from each filter were also fed to a Master estimate in the form of a Federated Extended Kalman Filter. The Master estimate applied a fusion algorithm to the estimates provided by GPS and vision sensor filters to get a fused estimate of the system's relative position and velocity.

Proportional Derivative control laws were applied to the system to achieve the desired relative position and attitude for autonomous rendezvous and docking. The translational controller based its calculations on the position and velocity data from the Master estimate.

Perturbations including J_2 and atmospheric drag were imposed to test the robustness of the estimation and control algorithms.

Two simulations were performed. In the first simulation, GPS and vision sensors systems each had a local filter to provide estimates based off of the individual sensor's

measurements. These local filters were tuned and operated independently of each other and independently of the Master Estimate.

In the second simulation, the local filters state and covariance matrices were reinitialized by the Master Estimate at each estimation iteration.

The vision estimation performance showed slight improvement between the first and second case. The Master Estimate showed an improvement of about an order of magnitude in the second simulation reducing the average estimation error from $10 - 20cm$ along each axis to about $1 - 2cm$. A vast improvement of several orders of magnitude in the GPS estimation was shown when reinitialization by the Master Estimate was performed.

9.1 Future Work

There are a number of future research paths that can be explored as an extension of this research project. A more realistic attitude determination sensor could be developed and applied to the system.

The relative position tracking controls could be optimized. For a rescue mission the trajectory taken by the Pursuer could be optimized to reduce flight time while in non-emergency cases the flight path could be optimized to reduce fuel consumption. Another way to potentially improve the tracking procedure is to prescribe a trajectory and at regular intervals recalculate and update the prescribed trajectory.

Observability analysis could also be performed to determine when the vision sensor should be activated and to see 'how observable' such parameters as J_2 and the satellite's ballistic coefficient are. Work could also be done to smooth the transition when a sensor is suddenly cut on/off and when local sensors are reinitialized by the fused estimate.

APPENDIX A

EXPONENTIAL ATMOSPHERE MODEL

Although a very simple approach, this method yields moderate results for general studies. This model uses the *U.S. Standard Atmosphere* (1976) for $0km$, CIRA-72 for $25 - 500km$, and CIRA-72 with exospheric temperature, exospheric temperature, $T_\infty = 1000K$ for $500 - 1000km$. The scale heights have been adjusted to maintain a piecewise-continuous formulation of the density [16].

Standard Atmosphere $(0 - 1000)\,km$: The Standard Atmosphere has been published twice (1962 and 1976) in an attempt to provide a standard reference model. It is an ideal, steady-state model of the Earth's atmosphere at a latitude of 45°N during moderate solar activity. The U.S. Committee on Extension of the Standard Atmosphere (COESA) has adopted two definitions that show its intent:

> A hypothetical vertical distribution of atmospheric temperature, pressure, and density which, by international agreement, is roughly representative of year-round, midlatitude conditions. Typical usages are as a basis for pressure altimeter calibrations, aircraft performance calculations, aircraft and rocket design, ballistic tables, and meteorological diagrams. The air is assumed to obey the perfect gas law and the hydrostatic equation which, taken together, relate temperature, pressure and density with geopotential. Only one standard atmosphere should be specified at a particular time and this standard atmosphere must not be subjected to amendment except at intervals of many years. (US Standard, 1976, xiv).

Satellites operating at much higher altitudes required the Committee to adopt another goal for the Standard Atmosphere:

> This atmosphere shall also be considered to rotate with the Earth, and be an average over the diurnal cycle, semi-annual variation, and the range of conditions from active to quiet geomagnetic, and of active to quiet sunspot

conditions. Above the tropopause (about 110 km) generalized forms of the hydrostatic equations apply. (US Standard, 1976, xiv) [16].

CIRA $(25 - 2500)\,km$: The Committee on Space Research (COSPAR) of the International Council of Scientific Unions periodically determines an atmospheric model. The current version is the COSPAR International Reference Atmosphere (CIRA-90) model. The first model was produced in 1965 (CIRA-65), which was basically a new model for altitudes from $30 - 300km$, based on Champion (1963) and the Harris-Priester (1962) model from $120 - 800km$. CIRA-72 included mean values from $25 - 500km$, and Jacchia (1971) prepared models from $110 - 2000km$. The model is a semi-theoretical technique, but it does have some free variables. Data comes mainly from measurements of satellite drag and ground-based measurements [16].

Table A.1 Exponential Atmosphere Model

Altitude h_{ellp} (km)	**Base Altitude** $h_\circ$ (km)	**Nominal Density** $\rho_\circ\,(kg/m^3)$	**Scale Height** H (km)
0-25	0	1.225	7.249
25-30	25	3.899×10^{-2}	6.349
30-40	30	1.774×10^{-2}	6.682
40-50	40	3.972×10^{-3}	7.554
50-60	50	1.057×10^{-3}	8.382
60-70	60	3.206×10^{-4}	7.714
70-80	70	8.770×10^{-5}	6.549
80-90	80	1.905×10^{-5}	5.799
90-100	90	3.396×10^{-6}	5.382
100-110	100	5.297×10^{-7}	5.877
110-120	110	9.661×10^{-8}	7.263
120-130	120	2.438×10^{-8}	9.473
130-140	130	8.484×10^{-9}	12.636
140-150	140	3.845×10^{-9}	16.149
150-180	150	2.070×10^{-9}	22.523
180-200	180	5.464×10^{-10}	29.740
200-250	200	2.789×10^{-10}	37.105
250-300	250	7.248×10^{-11}	45.546
300-350	300	2.418×10^{-11}	53.628
350-400	350	9.518×10^{-12}	53.298
400-450	400	3.725×10^{-12}	58.515
450-500	450	1.585×10^{-12}	60.828
500-600	500	6.967×10^{-13}	63.822
600-700	600	1.454×10^{-13}	71.835
700-800	700	3.614×10^{-14}	88.667
800-900	800	1.170×10^{-14}	124.64
900-1000	900	5.245×10^{-15}	181.05
1000-	1000	3.019×10^{-15}	268.00

APPENDIX B

ESTIMATION MODELS JACOBIAN MATRICES

In this appendix the F matrices used in the Extended Kalman Filter covariance propagation models are used. F is calculated by taking the Jacobian of the state's dynamics with respect to the state.

$$F\left(\hat{\mathbf{x}}\left(t\right),t\right) \equiv \left.\frac{\partial \dot{\mathbf{x}}}{\partial \mathbf{x}}\right|_{\hat{\mathbf{x}}(t)}$$

B.1 GPS Model

The estimated state vector for the GPS estimation model is

$$\mathbf{x}_{GPS} = \begin{bmatrix} X_P & X_P & Z_P & \dot{X}_P & \dot{Y}_P & \dot{Z}_P & \tau & J_2 & B \end{bmatrix}^T$$

and the equations of motion that govern the state vector are where

$$\dot{\mathbf{x}}_{GPS} = \begin{bmatrix} \dot{X} & \dot{Y} & \dot{Z} & \ddot{X} & \ddot{Y} & \ddot{Z} & \dot{\tau} & \dot{J}_2 & \dot{B} \end{bmatrix}^T =$$

$$\begin{bmatrix} \dot{X} \\ \dot{Y} \\ \dot{Z} \\ -\frac{\mu X}{R_P^3} - \frac{3\mu J_2 R_E^2 X}{2R_P^5}\left(1-\frac{5Z^2}{R_P^2}\right) - \frac{1}{2}\rho B\left(\dot{X}+\omega_E Y\right)\sqrt{\left(\dot{X}+\omega_E Y\right)^2+\left(\dot{Y}-\omega_E X\right)^2+\dot{Z}^2} \\ -\frac{\mu Y}{R_P^3} - \frac{3\mu J_2 R_E^2 Y}{2R_P^5}\left(1-\frac{5Z^2}{R_P^2}\right) - \frac{1}{2}\rho B\left(\dot{Y}-\omega_E X\right)\sqrt{\left(\dot{X}+\omega_E Y\right)^2+\left(\dot{Y}-\omega_E X\right)^2+\dot{Z}^2} \\ -\frac{\mu Z}{R_P^3} - \frac{3\mu J_2 R_E^2 Z}{2R_P^5}\left(3-\frac{5Z^2}{R_P^2}\right) - \frac{1}{2}\rho B\left(\dot{Z}\right)\sqrt{\left(\dot{X}+\omega_E Y\right)^2+\left(\dot{Y}-\omega_E X\right)^2+\dot{Z}^2} \\ 0 \\ 0 \\ 0 \end{bmatrix}$$

$$\mathbf{R}_P = \sqrt{X^2+Y^2+Z^2}$$

For this model F is given by

$$F_{GPS} = \begin{bmatrix} \frac{\partial \dot{X}}{\partial X} & \frac{\partial \dot{X}}{\partial Y} & \cdots & \frac{\partial \dot{X}}{\partial B} \\ \frac{\partial \dot{Y}}{\partial X} & \frac{\partial \dot{Y}}{\partial Y} & \cdots & \frac{\partial \dot{Y}}{\partial B} \\ \vdots & \vdots & \ddots & \vdots \\ \frac{\partial \dot{B}}{\partial X} & \frac{\partial \dot{B}}{\partial Y} & \cdots & \frac{\partial \dot{B}}{\partial B} \end{bmatrix}_{9\times 9}$$

Taking the partials of the equations above to populate F_{GPS} gives

$$\frac{\partial \dot{X}}{\partial X} = \frac{\partial \dot{X}}{\partial Y} = \frac{\partial \dot{X}}{\partial Z} = \frac{\partial \dot{X}}{\partial \dot{Y}} = \frac{\partial \dot{X}}{\partial \dot{Z}} = \frac{\partial \dot{X}}{\partial \tau} = \frac{\partial \dot{X}}{\partial J_2} = \frac{\partial \dot{X}}{\partial B} = 0, \frac{\partial \dot{X}}{\partial \dot{X}} = 1$$
$$\frac{\partial \dot{Y}}{\partial X} = \frac{\partial \dot{Y}}{\partial Y} = \frac{\partial \dot{Y}}{\partial Z} = \frac{\partial \dot{Y}}{\partial \dot{X}} = \frac{\partial \dot{Y}}{\partial \dot{Z}} = \frac{\partial \dot{Y}}{\partial \tau} = \frac{\partial \dot{Y}}{\partial J_2} = \frac{\partial \dot{Y}}{\partial B} = 0, \frac{\partial \dot{Y}}{\partial \dot{Y}} = 1$$
$$\frac{\partial \dot{Z}}{\partial X} = \frac{\partial \dot{Z}}{\partial Y} = \frac{\partial \dot{Z}}{\partial Z} = \frac{\partial \dot{Z}}{\partial \dot{X}} = \frac{\partial \dot{Z}}{\partial \dot{Y}} = \frac{\partial \dot{Z}}{\partial \tau} = \frac{\partial \dot{Z}}{\partial J_2} = \frac{\partial \dot{Z}}{\partial B} = 0, \frac{\partial \dot{Z}}{\partial \dot{Z}} = 1$$

$$\frac{\partial \dot{\tau}}{\partial X} = \frac{\partial \dot{\tau}}{\partial Y} = \frac{\partial \dot{\tau}}{\partial Z} = \frac{\partial \dot{\tau}}{\partial \dot{X}} = \frac{\partial \dot{\tau}}{\partial \dot{Y}} = \frac{\partial \dot{\tau}}{\partial \dot{Z}} = \frac{\partial \dot{\tau}}{\partial \tau} = \frac{\partial \dot{\tau}}{\partial J_2} = \frac{\partial \dot{\tau}}{\partial B} = 0$$
$$\frac{\partial \dot{J}_2}{\partial X} = \frac{\partial \dot{J}_2}{\partial Y} = \frac{\partial \dot{J}_2}{\partial Z} = \frac{\partial \dot{J}_2}{\partial \dot{X}} = \frac{\partial \dot{J}_2}{\partial \dot{Y}} = \frac{\partial \dot{J}_2}{\partial \dot{Z}} = \frac{\partial \dot{J}_2}{\partial \tau} = \frac{\partial \dot{J}_2}{\partial J_2} = \frac{\partial \dot{J}_2}{\partial B} = 0$$
$$\frac{\partial \dot{B}}{\partial X} = \frac{\partial \dot{B}}{\partial Y} = \frac{\partial \dot{B}}{\partial Z} = \frac{\partial \dot{B}}{\partial \dot{X}} = \frac{\partial \dot{B}}{\partial \dot{Y}} = \frac{\partial \dot{B}}{\partial \dot{Z}} = \frac{\partial \dot{B}}{\partial \tau} = \frac{\partial \dot{B}}{\partial J_2} = \frac{\partial \dot{B}}{\partial B} = 0$$

$$
\begin{aligned}
\frac{\partial \ddot{X}}{\partial X} &= -\frac{\mu}{R_P^3} + \frac{3\mu X^2}{R_P^5} - \frac{3\mu J_2 R_E^2}{2R_P^5}\left(1 - \frac{5Z^2}{R_P^2}\right) + \frac{15\mu J_2 R_E^2 X^2}{2R_P^7}\left(1 - \frac{5Z^2}{R_P^2}\right) - \frac{15\mu J_2 R_E^2 X^2 Z^2}{R_P^9} \\
&\quad - \frac{B\rho\omega_E\left(\dot{X} + \omega_E Y\right)\left(-\dot{Y} + \omega_E X\right)}{2\Omega} \\
\frac{\partial \ddot{X}}{\partial Y} &= -\frac{3\mu XY}{R_P^5} + \frac{15\mu J_2 R_E^2 XY}{2R_P^7}\left(1 - \frac{5Z^2}{R_P^2}\right) - \frac{15\mu J_2 R_E^2 XYZ^2}{2R_P^9} \\
&\quad - \frac{B\rho\omega_E\left(\dot{X} + \omega_E Y\right)^2}{2\Omega} - \frac{B\rho\omega_E\Omega}{2} \\
\frac{\partial \ddot{X}}{\partial Z} &= \frac{3\mu XZ}{R_P^5} + \frac{15\mu J_2 R_E^2 XZ}{2R_P^7}\left(1 - \frac{5Z^2}{R_P^2}\right) - \frac{3\mu J_2 R_E^2 X}{2R_P^5}\left(\frac{-10Z}{R_P^2} + \frac{10Z^3}{R_P^4}\right) \\
\frac{\partial \ddot{X}}{\partial \dot{X}} &= -\frac{B\rho\left(\dot{X} + \omega_E Y\right)^2}{2\Omega} - \frac{B\rho\Omega}{2} \\
\frac{\partial \ddot{X}}{\partial \dot{Y}} &= -\frac{B\rho\left(\dot{X} + \omega_E Y\right)\left(\dot{Y} - \omega_E X\right)}{2\Omega} \\
\frac{\partial \ddot{X}}{\partial \dot{Z}} &= -\frac{B\rho\left(\dot{X} + \omega_E Y\right)\dot{Z}}{2\Omega} \\
\frac{\partial \ddot{X}}{\partial \tau} &= 0 \\
\frac{\partial \ddot{X}}{\partial J_2} &= -\frac{3\mu R_E^2 X}{2R_P^5}\left(1 - \frac{5Z^2}{R_P^2}\right) \\
\frac{\partial \ddot{X}}{\partial B} &= -\frac{\rho\Omega\left(\dot{X} + \omega_E Y\right)}{2}
\end{aligned}
$$

$$
\begin{aligned}
\frac{\partial \ddot{Y}}{\partial X} &= \frac{3\mu XY}{R_P^5} + \frac{15\mu J_2 R_E^2 XY}{2R_P^7}\left(1 - \frac{5Z^2}{R_P^2}\right) - \frac{15\mu J_2 R_E^2 XYZ^2}{R_P^9} \\
&\quad - \frac{B\rho\omega_E\left(\dot{Y} - \omega_E X\right)\left(-\dot{Y} + \omega_E X\right)}{2\Omega} + \frac{B\rho\omega_E\Omega}{2} \\
\frac{\partial \ddot{Y}}{\partial Y} &= -\frac{\mu}{R_P^3} + \frac{3\mu Y^2}{R_P^5} - \frac{3\mu J_2 R_E^2}{2R_P^5}\left(1 - \frac{5Z^2}{R_P^2}\right) + \frac{15\mu J_2 R_E^2 Y^2}{2R_P^7}\left(1 - \frac{5Z^2}{R_P^2}\right) - \frac{15\mu J_2 R_E^2 Y^2 Z^2}{R_P^9} \\
&\quad - \frac{B\rho\omega_E\left(\dot{Y} - \omega_E X\right)\left(\dot{X} + \omega_E Y\right)}{2\Omega} \\
\frac{\partial \ddot{Y}}{\partial Z} &= \frac{3\mu YZ}{R_P^5} + \frac{15\mu J_2 R_E^2 YZ}{2R_P^7}\left(1 - \frac{5Z^2}{R_P^2}\right) - \frac{3\mu J_2 R_E^2 Y}{2R_P^5}\left(\frac{-10Z}{R_P^2} + \frac{10Z^3}{R_P^4}\right) \\
\frac{\partial \ddot{Y}}{\partial \dot{X}} &= -\frac{B\rho\left(\dot{Y} - \omega_E X\right)\left(\dot{X} + \omega_E Y\right)}{2\Omega} \\
\frac{\partial \ddot{Y}}{\partial \dot{Y}} &= -\frac{B\rho\left(\dot{Y} - \omega_E X\right)^2}{2\Omega} - \frac{B\rho\Omega}{2} \\
\frac{\partial \ddot{Y}}{\partial \dot{Z}} &= -\frac{B\rho\left(\dot{Y} - \omega_E X\right)\dot{Z}}{2\Omega} \\
\frac{\partial \ddot{Y}}{\partial \tau} &= 0 \\
\frac{\partial \ddot{Y}}{\partial J_2} &= -\frac{3\mu R_E^2 Y}{2R_P^5}\left(1 - \frac{5Z^2}{R_P^2}\right) \\
\frac{\partial \ddot{Y}}{\partial B} &= -\frac{\rho\Omega\left(\dot{Y} - \omega_E X\right)}{2}
\end{aligned}
$$

$$
\begin{aligned}
\frac{\partial \ddot{Z}}{\partial X} &= \frac{3\mu XZ}{R_P^5} + \frac{15\mu J_2 R_E^2 XZ}{2R_P^7}\left(3 - \frac{5Z^2}{R_P^2}\right) - \frac{15\mu J_2 R_E^2 XZ^3}{R_P^9} - \frac{B\rho\omega_E\left(-\dot{Y} + \omega_E X\right)\dot{Z}}{2\Omega} \\
\frac{\partial \ddot{Z}}{\partial Y} &= \frac{3\mu YZ}{R_P^5} + \frac{15\mu J_2 R_E^2 YZ}{2R_P^7}\left(3 - \frac{5Z^2}{R_P^2}\right) - \frac{15\mu J_2 R_E^2 YZ^3}{R_P^9} - \frac{B\rho\omega_E\left(\dot{X} + \omega_E Y\right)\dot{Z}}{2\Omega} \\
\frac{\partial \ddot{Z}}{\partial Z} &= -\frac{\mu}{R_P^3} + \frac{3\mu Z^2}{R_P^5} - \frac{3\mu J_2 R_E^2}{2R_P^5}\left(3 - \frac{5Z^2}{R_P^2}\right) + \frac{15\mu J_2 R_E^2 Z^2}{2R_P^7}\left(3 - \frac{5Z^2}{R_P^2}\right) \\
&\quad -\frac{3\mu J_2 R_E^2 Z}{R_P^5}\left(\frac{-10Z}{R_P^2} + \frac{10Z^3}{R_P^4}\right) \\
\frac{\partial \ddot{Z}}{\partial \dot{X}} &= -\frac{B\rho\left(\dot{X} + \omega_E Y\right)\dot{Z}}{2\Omega} \\
\frac{\partial \ddot{Z}}{\partial \dot{Y}} &= -\frac{B\rho\left(\dot{Y} - \omega_E X\right)\dot{Z}}{2\Omega} \\
\frac{\partial \ddot{Z}}{\partial \dot{Z}} &= -\frac{B\rho\dot{Z}^2}{2\Omega} - \frac{B\rho\Omega}{2} \\
\frac{\partial \ddot{Y}}{\partial \tau} &= 0 \\
\frac{\partial \ddot{Z}}{\partial J_2} &= -\frac{3\mu R_E^2 Z}{2R_P^5}\left(3 - \frac{5Z^2}{R_P^2}\right) \\
\frac{\partial \ddot{Z}}{\partial B} &= -\frac{\rho\Omega\dot{Z}}{2}
\end{aligned}
$$

where $\Omega = \sqrt{\left(\dot{X} + \omega_E Y\right)^2 + \left(\dot{Y} - \omega_E X\right)^2 + \dot{Z}^2}$

B.2 Vision Based Model

The estimated state vector for the vision model is

$$
\mathbf{x}_{vision} = \begin{bmatrix} x & y & z & \dot{x} & \dot{y} & \dot{z} \end{bmatrix}^T
$$

and the dynamics governing the relative motion is

$$\dot{\mathbf{x}}_{vision} = \begin{bmatrix} \dot{x} \\ \dot{y} \\ \dot{z} \\ \ddot{x} \\ \ddot{y} \\ \ddot{z} \end{bmatrix} = \begin{bmatrix} \dot{x} \\ \dot{y} \\ \dot{z} \\ 2\dot{\theta}\dot{y} + \ddot{\theta}y + \dot{\theta}^2 x - \frac{\mu(R_T+x)}{\left((R_T+x)^2+y^2+z^2\right)^{3/2}} + \frac{\mu}{R_T^2} \\ -2\dot{\theta}\dot{x} - \ddot{\theta}x + \dot{\theta}^2 y - \frac{\mu y}{\left((R_T+x)^2+y^2+z^2\right)^{3/2}} \\ -\frac{\mu z}{\left((R_T+x)^2+y^2+z^2\right)^{3/2}} \end{bmatrix}$$

F is again computed by taking the Jacobian of the dynamics with respect to the state vector

$$F_{vision} = \begin{bmatrix} \frac{\partial \dot{x}}{\partial x} & \frac{\partial \dot{x}}{\partial y} & \cdots & \frac{\partial \dot{x}}{\partial \dot{z}} \\ \frac{\partial \dot{y}}{\partial x} & \frac{\partial \dot{y}}{\partial y} & \cdots & \frac{\partial \dot{y}}{\partial \dot{z}} \\ \vdots & \vdots & \ddots & \vdots \\ \frac{\partial \dot{z}}{\partial x} & \frac{\partial \dot{z}}{\partial y} & \cdots & \frac{\partial \dot{z}}{\partial \dot{z}} \end{bmatrix}_{6\times 6}$$

Taking the partials yields

$$\frac{\partial \dot{x}}{\partial x} = \frac{\partial \dot{x}}{\partial y} = \frac{\partial \dot{x}}{\partial z} = \frac{\partial \dot{x}}{\partial \dot{y}} = \frac{\partial \dot{x}}{\partial \dot{z}} = 0, \frac{\partial \dot{x}}{\partial \dot{x}} = 1$$
$$\frac{\partial \dot{y}}{\partial x} = \frac{\partial \dot{y}}{\partial y} = \frac{\partial \dot{y}}{\partial z} = \frac{\partial \dot{y}}{\partial \dot{x}} = \frac{\partial \dot{y}}{\partial \dot{z}} = 0, \frac{\partial \dot{y}}{\partial \dot{y}} = 1$$
$$\frac{\partial \dot{z}}{\partial x} = \frac{\partial \dot{z}}{\partial y} = \frac{\partial \dot{z}}{\partial z} = \frac{\partial \dot{z}}{\partial \dot{x}} = \frac{\partial \dot{z}}{\partial \dot{y}} = 0, \frac{\partial \dot{z}}{\partial \dot{z}} = 1$$

$$
\begin{aligned}
\frac{\partial \ddot{x}}{\partial x} &= \dot{\theta}^2 - \frac{\mu}{\left(\left(R_T + x\right)^2 + y^2 + z^2\right)^{3/2}} + \frac{3\mu\left(R_T + x\right)^2}{\left(\left(R_T + x\right)^2 + y^2 + z^2\right)^{5/2}} \\
\frac{\partial \ddot{x}}{\partial y} &= \ddot{\theta} + \frac{3\mu y\left(R_T + x\right)}{\left(\left(R_T + x\right)^2 + y^2 + z^2\right)^{5/2}} \\
\frac{\partial \ddot{x}}{\partial z} &= \frac{3\mu z\left(R_T + x\right)}{\left(\left(R_T + x\right)^2 + y^2 + z^2\right)^{5/2}} \\
\frac{\partial \ddot{x}}{\partial \dot{x}} &= 0 \\
\frac{\partial \ddot{x}}{\partial \dot{y}} &= 2\dot{\theta} \\
\frac{\partial \ddot{x}}{\partial \dot{z}} &= 0
\end{aligned}
$$

$$
\begin{aligned}
\frac{\partial \ddot{y}}{\partial x} &= -\ddot{\theta} + \frac{3\mu y\left(R_T + x\right)}{\left(\left(R_T + x\right)^2 + y^2 + z^2\right)^{5/2}} \\
\frac{\partial \ddot{y}}{\partial y} &= \dot{\theta}^2 - \frac{\mu}{\left(\left(R_T + x\right)^2 + y^2 + z^2\right)^{3/2}} + \frac{3\mu y^2}{\left(\left(R_T + x\right)^2 + y^2 + z^2\right)^{5/2}} \\
\frac{\partial \ddot{y}}{\partial z} &= \frac{3\mu yz}{\left(\left(R_T + x\right)^2 + y^2 + z^2\right)^{5/2}} \\
\frac{\partial \ddot{y}}{\partial \dot{x}} &= -2\dot{\theta} \\
\frac{\partial \ddot{y}}{\partial \dot{y}} &= 0 \\
\frac{\partial \ddot{y}}{\partial \dot{z}} &= 0
\end{aligned}
$$

$$
\begin{aligned}
\frac{\partial \ddot{z}}{\partial x} &= \frac{3\mu z\left(R_T+x\right)}{\left(\left(R_T+x\right)^2+y^2+z^2\right)^{5/2}} \\
\frac{\partial \ddot{z}}{\partial y} &= \frac{3\mu yz}{\left(\left(R_T+x\right)^2+y^2+z^2\right)^{5/2}} \\
\frac{\partial \ddot{z}}{\partial z} &= \frac{\mu}{\left(\left(R_T+x\right)^2+y^2+z^2\right)^{3/2}}+\frac{3\mu z^2}{\left(\left(R_T+x\right)^2+y^2+z^2\right)^{5/2}} \\
\frac{\partial \ddot{z}}{\partial \dot{x}} &= 0 \\
\frac{\partial \ddot{z}}{\partial \dot{y}} &= 0 \\
\frac{\partial \ddot{z}}{\partial \dot{z}} &= 0
\end{aligned}
$$

APPENDIX C

DERIVATION OF FUSION COVARIANCE TRANSFORMATIONS

The covariance for the local vision sensor system can be expressed as

$$ {}^{O}\mathbf{P}_{vision} = \begin{bmatrix} {}^{O}\mathbf{P}_{11} & {}^{O}\mathbf{P}_{21} \\ {}^{O}\mathbf{P}_{12} & {}^{O}\mathbf{P}_{22} \end{bmatrix} = \begin{bmatrix} E\left\{ {}^{O}\tilde{\mathbf{r}}{}^{O}\tilde{\mathbf{r}}^{T} \right\} & E\left\{ {}^{O}\tilde{\mathbf{r}}{}^{O}\dot{\tilde{\mathbf{r}}}^{T} \right\} \\ E\left\{ {}^{O}\dot{\tilde{\mathbf{r}}}{}^{O}\tilde{\mathbf{r}}^{T} \right\} & E\left\{ {}^{O}\dot{\tilde{\mathbf{r}}}{}^{O}\dot{\tilde{\mathbf{r}}}^{T} \right\} \end{bmatrix} \tag{C.1} $$

where each term is an expectation value. However, the vision's covariance needs to be in inertial components for integration into the fusion algorithm. The vision covariance needs to take the form

$$ {}^{N}\mathbf{P}_{vision} = \begin{bmatrix} {}^{N}\mathbf{P}_{11} & {}^{N}\mathbf{P}_{21} \\ {}^{N}\mathbf{P}_{12} & {}^{N}\mathbf{P}_{22} \end{bmatrix} = \begin{bmatrix} E\left\{ {}^{N}\tilde{\mathbf{r}}{}^{N}\tilde{\mathbf{r}}^{T} \right\} & E\left\{ {}^{N}\tilde{\mathbf{r}}{}^{N}\dot{\tilde{\mathbf{r}}}^{T} \right\} \\ E\left\{ {}^{N}\dot{\tilde{\mathbf{r}}}{}^{N}\tilde{\mathbf{r}}^{T} \right\} & E\left\{ {}^{N}\dot{\tilde{\mathbf{r}}}{}^{N}\dot{\tilde{\mathbf{r}}}^{T} \right\} \end{bmatrix} \tag{C.2} $$

Recall that in general

$$ \mathbf{R}_{P} = \mathbf{R}_{T} + \mathbf{r} \tag{C.3} $$

Setting $\mathbf{R}_P$ in the inertial reference frame gives

$$ {}^{N}\mathbf{R}_{P} = {}^{N}\mathbf{R}_{T} + {}^{N}\mathbf{r} = {}^{N}\mathbf{R}_{T} + [NO]\,{}^{O}\mathbf{r} \tag{C.4} $$

and the derivative of (C.4) can be found through the use of the transport theorem which gives

$$ {}^{N}\dot{\mathbf{R}}_{P} = {}^{N}\dot{\mathbf{R}}_{T} + [NO]\,{}^{O}\dot{\mathbf{r}} + [NO]\left[{}^{O}\boldsymbol{\omega}_{O/N}\times\right]{}^{O}\mathbf{r} \tag{C.5} $$

Looking at vision covariance's first term ${}^{O}\mathbf{P}_{11} = E\left\{{}^{O}\tilde{\mathbf{r}}{}^{O}\tilde{\mathbf{r}}^{T}\right\}$ and plugging in for ${}^{O}\tilde{\mathbf{r}}$ where ${}^{O}\tilde{\mathbf{r}} = [ON]\left({}^{N}\tilde{\mathbf{R}}_{P} - {}^{N}\mathbf{R}_{T}\right)$ gives

$$\begin{aligned}
{}^{O}\mathbf{P}_{11} &= E\left\{{}^{O}\tilde{\mathbf{r}}{}^{O}\tilde{\mathbf{r}}^{T}\right\} \\
&= E\left\{[ON]\left({}^{N}\tilde{\mathbf{R}}_{P} - {}^{N}\mathbf{R}_{T}\right)\left({}^{N}\tilde{\mathbf{R}}_{P}^{T} - {}^{N}\mathbf{R}_{T}^{T}\right)[NO]\right\} \\
&= [ON]\,E\left\{\left({}^{N}\tilde{\mathbf{R}}_{P} - {}^{N}\mathbf{R}_{T}\right)\left({}^{N}\tilde{\mathbf{R}}_{P}^{T} - {}^{N}\mathbf{R}_{T}^{T}\right)\right\}[NO] \\
&= [ON]\,E\left\{{}^{N}\tilde{\mathbf{r}}{}^{N}\tilde{\mathbf{r}}^{T}\right\}[NO] \\
&= [ON]\,{}^{N}\mathbf{P}_{11}\,[NO]
\end{aligned} \tag{C.6}$$

Premultiply equation (C.6) by $[NO]$ and postmultiply it by $[ON]$ to find the first term in the vision's inertial covariance

$${}^{N}\mathbf{P}_{11} = [NO]\,{}^{O}\mathbf{P}_{11}\,[ON] \tag{C.7}$$

$$\begin{aligned}
{}^{O}\mathbf{P}_{12} &= E\left\{{}^{O}\tilde{\mathbf{r}}{}^{O}\dot{\tilde{\mathbf{r}}}^{T}\right\} \\
&= E\left\{[ON]\left({}^{N}\tilde{\mathbf{R}}_{P} - {}^{N}\mathbf{R}_{T}\right)\left(\left[{}^{N}\dot{\tilde{\mathbf{R}}}_{P}^{T} - {}^{N}\dot{\mathbf{R}}_{T}^{T}\right][NO] - {}^{O}\tilde{\mathbf{r}}^{T}\left[{}^{O}\boldsymbol{\omega}_{O/N}\times\right]^{T}\right)\right\} \\
&= E\left\{[ON]\left({}^{N}\tilde{\mathbf{R}}_{P} - {}^{N}\mathbf{R}_{T}\right)\left({}^{N}\dot{\tilde{\mathbf{R}}}_{P}^{T} - {}^{N}\dot{\mathbf{R}}_{T}^{T}\right)[NO]\right. \\
&\qquad \left. - [ON]\left({}^{N}\tilde{\mathbf{R}}_{P} - {}^{N}\mathbf{R}_{T}\right)\left({}^{O}\tilde{\mathbf{r}}^{T}\left[{}^{O}\boldsymbol{\omega}_{O/N}\times\right]^{T}\right)\right\} \\
&= E\left\{[ON]\,{}^{N}\tilde{\mathbf{r}}_{P}{}^{N}\dot{\tilde{\mathbf{r}}}_{P}^{T}\,[NO] + {}^{O}\tilde{\mathbf{r}}_{P}{}^{O}\tilde{\mathbf{r}}_{P}^{T}\left[{}^{O}\boldsymbol{\omega}_{O/N}\times\right]\right\} \\
&= [ON]\,{}^{N}\mathbf{P}_{12}\,[NO] + {}^{O}\mathbf{P}_{11}\left[{}^{O}\boldsymbol{\omega}_{O/N}\times\right]
\end{aligned}$$

solve for ${}^{N}\mathbf{P}_{12}$

$${}^{N}\mathbf{P}_{12} = [NO]\left({}^{O}\mathbf{P}_{12} - {}^{O}\mathbf{P}_{11}\left[{}^{O}\boldsymbol{\omega}_{11}\times\right]\right)[ON] \tag{C.8}$$

$$
\begin{aligned}
{}^{O}\mathbf{P}_{21} &= E\left\{{}^{O}\dot{\tilde{\mathbf{r}}}{}^{O}\tilde{\mathbf{r}}^{T}\right\} \\
&= E\left\{\left([ON]\left[{}^{N}\dot{\tilde{\mathbf{R}}}_{P} - {}^{N}\dot{\mathbf{R}}_{T}\right] - \left[{}^{O}\boldsymbol{\omega}_{O/N}\times\right]{}^{O}\tilde{\mathbf{r}}\right)\left({}^{N}\tilde{\mathbf{R}}_{P}^{T} - {}^{N}\mathbf{R}_{T}^{T}\right)[NO]\right\} \\
&= E\left\{[ON]\left({}^{N}\dot{\tilde{\mathbf{R}}}_{P} - {}^{N}\dot{\mathbf{R}}_{T}\right)\left({}^{N}\tilde{\mathbf{R}}_{P}^{T} - {}^{N}\mathbf{R}_{T}^{T}\right)[NO]\right. \\
&\qquad \left. - \left[{}^{O}\boldsymbol{\omega}_{O/N}\times\right]{}^{O}\tilde{\mathbf{r}}\left({}^{N}\tilde{\mathbf{R}}_{P}^{T} - {}^{N}\mathbf{R}_{T}^{T}\right)[NO]\right\} \\
&= E\left\{[ON]\,{}^{N}\dot{\tilde{\mathbf{r}}}{}^{N}\tilde{\mathbf{r}}^{T}\,[NO] - \left[{}^{O}\boldsymbol{\omega}_{O/N}\times\right]{}^{O}\,\tilde{\mathbf{r}}{}^{O}\tilde{\mathbf{r}}^{T}\right\} \\
&= [ON]\,{}^{N}\mathbf{P}_{21}\,[NO] - \left[{}^{O}\boldsymbol{\omega}_{O/N}\times\right]{}^{O}\mathbf{P}_{11}
\end{aligned}
$$

solve for ${}^{N}\mathbf{P}_{21}$

$$
{}^{N}\mathbf{P}_{21} = [NO]\left({}^{O}\mathbf{P}_{21} + \left[{}^{O}\boldsymbol{\omega}\times\right]{}^{O}\mathbf{P}_{11}\right)[ON] \tag{C.9}
$$

${}^{N}\mathbf{P}_{22}$ can be found in a similar manner.

$$
\begin{aligned}
{}^{O}\mathbf{P}_{22} &= E\left\{{}^{O}\dot{\tilde{\mathbf{r}}}{}^{O}\dot{\tilde{\mathbf{r}}}^{T}\right\} \\
&= E\left\{\left([ON]\left[{}^{N}\dot{\tilde{\mathbf{R}}}_{P} - {}^{N}\dot{\mathbf{R}}_{T}\right] - \left[{}^{O}\boldsymbol{\omega}_{O/N}\times\right]{}^{O}\tilde{\mathbf{r}}\right)\right. \\
&\qquad \left.\left(\left[{}^{N}\dot{\tilde{\mathbf{R}}}_{P}^{T} - {}^{N}\dot{\mathbf{R}}_{T}^{T}\right][NO] - {}^{O}\tilde{\mathbf{r}}^{T}\left[{}^{O}\boldsymbol{\omega}_{O/N}\times\right]^{T}\right)\right\} \\
&= E\left\{[ON]\left[{}^{N}\dot{\tilde{\mathbf{R}}}_{P} - {}^{N}\dot{\mathbf{R}}_{T}\right]\left[{}^{N}\dot{\tilde{\mathbf{R}}}_{P}^{T} - {}^{N}\dot{\mathbf{R}}_{T}^{T}\right][NO]\right. \\
&\qquad - [ON]\left[{}^{N}\dot{\tilde{\mathbf{R}}}_{P} - {}^{N}\dot{\mathbf{R}}_{T}\right]{}^{O}\tilde{\mathbf{r}}^{T}\left[{}^{O}\boldsymbol{\omega}_{O/N}\times\right]^{T} \\
&\qquad - \left[{}^{O}\boldsymbol{\omega}_{O/N}\times\right]{}^{O}\tilde{\mathbf{r}}\left[{}^{N}\dot{\tilde{\mathbf{R}}}_{P}^{T} - {}^{N}\dot{\mathbf{R}}_{T}^{T}\right][NO] \\
&\qquad \left. + \left[{}^{O}\boldsymbol{\omega}_{O/N}\times\right]{}^{O}\tilde{\mathbf{r}}{}^{O}\tilde{\mathbf{r}}^{T}\left[{}^{O}\boldsymbol{\omega}_{O/N}\times\right]^{T}\right\} \\
&= E\left\{[ON]\,{}^{N}\dot{\tilde{\mathbf{r}}}{}^{N}\dot{\tilde{\mathbf{r}}}^{T}[NO] + {}^{O}\dot{\tilde{\mathbf{r}}}{}^{O}\tilde{\mathbf{r}}^{T}\left[{}^{O}\boldsymbol{\omega}_{O/N}\times\right] - \left[{}^{O}\boldsymbol{\omega}\times\right]{}^{O}\tilde{\mathbf{r}}{}^{O}\dot{\tilde{\mathbf{r}}}\right. \\
&\quad \left. - \left[{}^{O}\boldsymbol{\omega}_{O/N}\times\right]{}^{O}\tilde{\mathbf{r}}{}^{O}\tilde{\mathbf{r}}^{T}\left[{}^{O}\boldsymbol{\omega}_{O/N}\times\right]\right\} \\
&= [ON]\,{}^{N}\mathbf{P}_{22}\,[NO] + {}^{O}\mathbf{P}_{21}\left[{}^{O}\boldsymbol{\omega}_{O/N}\times\right] - \left[{}^{O}\boldsymbol{\omega}_{O/N}\times\right]{}^{O}\mathbf{P}_{12} \\
&\quad - \left[{}^{O}\boldsymbol{\omega}_{O/N}\times\right]{}^{O}\mathbf{P}_{11}\left[{}^{O}\boldsymbol{\omega}_{O/N}\times\right]
\end{aligned}
\tag{C.10}
$$

Solving for ${}^{N}\mathbf{P}_{22}$ gives

$$
\begin{aligned}
{}^{N}\mathbf{P}_{22} = [NO]\,\big({}^{O}\mathbf{P}_{22} - {}^{O}\mathbf{P}_{21}\left[{}^{O}\boldsymbol{\omega}_{O/N}\times\right] + \left[{}^{O}\boldsymbol{\omega}_{O/N}\times\right]{}^{O}\mathbf{P}_{12} + \\
\left[{}^{O}\boldsymbol{\omega}_{O/N}\times\right]{}^{O}\mathbf{P}_{11}\left[{}^{O}\boldsymbol{\omega}_{O/N}\times\right]\big)\,[ON]
\end{aligned}
\tag{C.11}
$$

REFERENCES

[1] http://www pao.ksc.nasa.gov/kscpao/history/gemini/gemini.htm, "Gemini: Stepping Stone to the Moon," .

[2] Jacobsen, S., Zhu, C., Lee, C., and Dubowsky, S., "Planning of Safe Kinematic Trajectories for Free Flying Robots Approaching an Uncontrolled Spinning Satellite," Proceedings of DETC'02 ASME 2002 Design Engineering Technical Conferences and Computer and Information in Engineering Conference, ASME, Montreal, Canada, September 2002, pp. 1–7.

[3] Center, N. M. S., "The Space Launch Initiative: Technology to Pioneer the Space Frontier," NASA Fact Sheets (FS-2003-02-28-MSFC, Feb. 2003.

[4] Lightsey, E. G. and Um, J., "Autonomous Relative Navigation Methods in the Proximity of the International Space Station," Proceedings of the International Symposium on Kinematic Systems in Geodesy, Geomagnetics, and Navigation, Calgary, Canada, 2001, pp. 169–179.

[5] http://www.nasa.gov/mission_pages/station/structure/elements/progress.html, "Russian Progress Spacecraft," .

[6] Isao, K., Mokuno, M., Toru, K., and Suziki, T., "Result of Autonomous Rendezvous Docking Experiment of Engineering Test Satellite-VII," *AIAA Journal of Spacecraft and Rockets*, Vol. 38, No. 1, Jan-Feb 2001, pp. 105–111.

[7] http://www.nasa.gov/mission_pages/dart/main/index.html, "Summary of DART Accident Report," .

[8] Matsumoto, S., Ohkami, Y., Wakabayashi, Y., Oda, M., and Ueno, H., "Satellite Capturing Strategy using Agile Orbital Servicing Vehicle, Hyper-OSV," Pro-

ceedings of the 2002 IEEE International Conference on Robotics & Automation, IEEE, Washington, DC, May 2002, pp. 2309–2314.

[9] Gaylor, D. E., Lightsey, E. G., and Key, K. W., "Effects of Multipath and Signal Blockage on GPS Navigation in the Vicinity of the International Space Station," ION GPS/GNSS, Portland, OR, Sept 12 2003.

[10] Gaylor, D. E., *Integrated GPS/INS Navigation System Design for Autonomous Spacecraft Rendezvous*, Ph.D. thesis, The University of Texas at Austin, Austin, TX., December 2003.

[11] Gaylor, D. E. and Lightsey, E. G., "GPS/INS Kalman Filter Design for Spacecraft Operating in the Proximity of the International Space Station," AIAA Guidance, Navigation, and Control Conference and Exhibit, AIAA, Austin, TX., Aug. 2003, p. 11.

[12] Grewal, M. S., Weill, L. R., and Andrews, A. P., *Global Positioning Systems, Inertial Navigation, and Integration*, John Wiley & Sons Inc., New York, NY., 2001.

[13] K. K. Gunnam, D. C. Hughes, J. L. J. and Kehtarnavaz, N. K., "A Vision-Based DSP Embedded Navigation Sensor," *IEEE Sensors Journal*, Vol. 2, No. 5, Oct. 2002, pp. 15.

[14] Sun, D. and Crassidis, J. L., "Observability Analysis of Six Degree of Freedom Configuration Determination Using Vector Observations," *Journal of Guidance, Control, and Dynamics*, Vol. 25, No. 6, Nov-Dec 2002, pp. 1149–1157.

[15] Lichter, M. D. and Dubowsky, S., "State, Shape, and Parameter Estimation of Space Objects from Range Images," Proceedings of the 2004 IEEE International Conference on Robotics & Automation, IEEE, New Orleans, LA., April 2004, pp. 2974–2979.

[16] Vallado, D. A., *Fundamentals of Astrodynamics and Applications*, Microcosm Press, El Segundo, CA., 2nd ed., 2001.

[17] Junkins, J. L. and Schaub, H., *Analytical Mechanics of Space Systems*, AIAA, 2003.

[18] Wiesel, W. E., *Spaceflight Dynamics*, Irwin/McGraw-Hill, New York, NY., 2nd ed., 1997.

[19] Crassidis, J. L. and Junkins, J. L., *Optimal Estimation of Dynamic Systems*, Chapman & Hall/CRC, Boca Raton, FL., 2004.

[20] http://gps.faa.gov/FAQ/faq gps.htm.

[21] http://celestrak.com/NORAD/elements.

[22] Crassidis, J. L. and Markley, F. L., "Attitude Estimation Using Modified Rodrigues Parameters," Proceedings of the Flight Mechanics/Estimation Theory Symposium, NASA-Goddard Space Flight Center, Greenbelt, MD, May 1996, pp. 71–83.

[23] Minkler, G. and Minkler, J., *Theory and Applications of Kalman Filtering*, Magellan Book Company, Palm Bay, FL., 1993.

[24] Carlson, N. A., "Federated Square Root Filter for Decentralized Parallel Processes," *IEEE Transactions On Aerospace*, Vol. AES-26, No. 3, May 1990 1990.

[25] Bierman, G. J. and Belzer, M., "A Decentralized Square Root Information Filter/Smoother," In Proceedings of the 24^{th} IEEE Conference on Decision and Control, Ft. Lauderdale, FL., Dec. 1985.

[26] Kerr, T. H., "Decentralized Filtering and Redundancy Management for Multisensor Navigation," *IEEE Transactions On Aerospace and Electronic Systems*, Vol. AES-23, 1987, pp. 83–119.

BIOGRAPHICAL STATEMENT

Jonathan McDonald was born in Dallas, TX in 1981 and later attended Richardson High School where he graduated with honors. From 1999-2004 he attended The University of Texas at Austin where he was a five year member and section leader of the Longhorn Band and graduated with a bachelors in Aerospace Engineering. In 2005 Jonathan began working towards a Master of Science in Aerospace Engineering. His research interests include guidance and control for satellite operations.